

Elucidating the Role of CD8+ T cells and Macrophages in Triple Negative Breast Cancer Recurrence

By

Benjamin Hacker

Dissertation

Submitted to the Faculty of the  
Graduate School of Vanderbilt University  
in partial fulfillment of the requirements

for the degree of

DOCTOR OF PHILOSOPHY

in

Chemical and Biomolecular Engineering

May 12, 2023

Nashville, Tennessee

Approved:

Marjan Rafat, Ph.D.

Barbara Fingleton, Ph.D.

John Wilson, Ph.D.

Scott Guelcher, Ph.D.

Copyright 2023 by Benjamin Christian Hacker  
All Rights Reserved

*To my friends and family*

## ACKNOWLEDGEMENTS

I have many people to thank, for there is no way I would have reached this point on my own. First, I would like to thank two high school teachers - Ms. Bruce and Swen, who are both outstanding educators who initially spurred my interest in science, chemistry, and engineering. I also owe a huge thanks to Professor Azarin at the University of Minnesota. Her research introduced me to biological and bio-engineering research – something that I knew I loved the moment I started it.

I would like to thank my immediate family for always pushing me to work hard and to constantly be a learner. I also owe gratitude to my Grandpa – he had a PhD in organic chemistry, and when I was a kid he loved sharing knowledge and talking about recent scientific advances. Back then I did not understand much of it, but I always aspired to do something scientific like him.

I owe a huge debt of gratitude to Marjan. I think about where I was when I started in lab, and I am very grateful for the amount of patience that she had. I have appreciated the fact that she always has my back, and she pushes me to be the best version of myself as a researcher.

I also want to thank my committee members, Drs. Fingleton, Wilson, and Guelcher, for their time, attention, and intellectual advice and feedback. Additionally, I would like to thank other co-mentors and collaborators, including Drs. Rathmell, Freeman, and Kirschner. They have all helped me to become a more confident and capable scientist.

I have been incredibly lucky to have the colleagues that I do have. We have a very healthy lab culture: there is a good mix of scientific curiosity, support, and humor, all of which have been invaluable to me making it through graduate school in one piece. I will miss it.

Finally, I want to thank my partner, Sage. She has supported me through the process, steadfastly, for many years. I am very grateful for her unwavering support and love.

## TABLE OF CONTENTS

|   |    |
|---|----|
| ACKNOWLEDGEMENTS .....  | 4  |
| LIST OF TABLES .....  | 8  |
| LIST OF FIGURES .....   | 9  |
| INTRODUCTION .....  | 12 |
| 1.1 Triple Negative Breast Cancer and Radiation Therapy .....   | 12 |
| 1.2 Radiation Therapy, Cancer Progression, and Recurrence.....  | 13 |
| 1.3 Radiation-Induced Damage in the mammary gland.....  | 17 |
| 1.4 Mammary and Tumor Organoids.....  | 21 |
| 1.4.1 Regenerative Capacity.....  | 25 |
| 1.4.2 Extracellular Matrix (ECM) and Cell-Matrix Interactions.....  | 26 |
| 1.4.3 Modeling Metastasis.....  | 28 |
| 1.4.4 Drug Screening.....   | 29 |
| 1.4.5 Co-Culture Models with Immune Cells.....  | 30 |
| 1.4.6 Other Technical Outputs.....  | 32 |
| 1.5 Investigating Normal Tissue Radiation Damage and cell infiltration.....   | 33 |
| 1.6 Future directions.....  | 38 |
| 1.7 Organization of Dissertation .....  | 40 |
| GROWTH AND CHARACTERIZATION OF IRRADIATED EPITHELIAL ORGANOIDS<br>FROM MAMMARY FAT PAD TISSUE .....                   | 41 |
| 2.1 Summary .....   | 41 |
| 2.2 Introduction .....  | 42 |
| 2.3 Materials and Methods.....  | 44 |
| 2.3.1. Mammary Gland Acquisition and Irradiation .....  | 44 |
| 2.3.2. Mechanical Disruption and Digestion of Mammary Glands.....   | 44 |
| 2.3.3 Determining Organoid Density.....   | 46 |
| 2.3.4. Plating Organoids .....  | 47 |
| 2.3.5 Co-culturing with Macrophages and 4T1s .....  | 47 |
| 2.3.6 Immunofluorescence Staining of Organoids .....  | 48 |
| 2.4 Results .....   | 50 |
| 2.5 Conclusions and Future Work.....  | 60 |
| IRRADIATED MAMMARY FIBROBLAST ORGANOIDS ELUCIDATE MECHANISMS OF<br>MACROPHAGE-MEDIATED BREAST CANCER RECURRENCE ..... | 63 |
| 3.1 Summary .....   | 63 |
| 3.2 Introduction .....  | 64 |
| 3.3 Materials and Methods.....  | 66 |

|  |           |
|--|-----------|
| 3.3.1 Cell Lines.....  | 66        |
| 3.3.2 Orthotopic Tumor Studies .....   | 66        |
| 3.3.3 Luminex Multiplex Cytokine Assay.....  | 67        |
| 3.3.4 Primary Organoid Generation .....  | 67        |
| 3.3.5 Radiation.....   | 67        |
| 3.3.6 Flow Cytometry.....  | 68        |
| 3.3.7 Organoid Embedding, Sectioning, and Immunofluorescence .....   | 69        |
| 3.3.8 Scanning Electron Microscopy (SEM).....  | 70        |
| 3.3.9 Primary Macrophage Isolation and Culture.....  | 70        |
| 3.3.10 Invasion Assay.....   | 71        |
| 3.3.11 Organoid 4T1 Migration Assay.....   | 71        |
| 3.3.12 IL-6 Quantification .....   | 72        |
| 3.3.13 Statistical Analysis .....  | 72        |
| 3.4 Results and Discussion.....  | 73        |
| 3.4.1 In vivo characterization of infiltrating macrophages and cytokine secretion resulting from radiation damage.....         | 73        |
| 3.4.2 Primary fibroblast organoid model.....   | 76        |
| 3.4.3. Direct co-culture experiments with M0 macrophages.....  | 78        |
| 3.4.3 The irradiated microenvironment facilitates TNBC cell recruitment through direct organoid -macrophage interactions ..... | 80        |
| 3.4.4 IL-6 secretion drives 4T1 cell invasiveness <i>in vitro</i> .....  | 84        |
| 3.4.5 IL-6 secretion drives 4T1 cell invasiveness <i>in vivo</i> .....   | 85        |
| 3.5 Conclusions and Future Work.....   | 87        |
| <b>CYTOTOXIC T CELLS INFLUENCE PHENOTYPES OF RADIATION DAMAGED STROMA</b><br>.....   | <b>88</b> |
| 4.1 Summary .....  | 88        |
| 4.2 Introduction .....   | 89        |
| 4.3 Materials and Methods.....   | 91        |
| 4.3.1 Primary CD8+ T cell isolation and culture.....   | 91        |
| 4.3.2 Cell Culture.....  | 92        |
| 4.3.3 Organoid co-culture and irradiation .....  | 93        |
| 4.3.4 Organoid Fixation, Staining, and Imaging .....   | 93        |
| 4.3.5 Invasion Assay.....  | 94        |
| 4.3.6 Reverse Phase Protein Array (RPPA) .....   | 94        |
| 4.3.7. Luminex Multiplex Cytokine Assay.....   | 95        |
| 4.4 Results and Discussion.....  | 95        |
| 4.4.1 Phenotypes associated with cell damage are upregulated and persistent in immunocompromised mice .....                    | 95        |
| 4.4.2 CD8+ T cell depletion alters the microenvironmental damage response post <i>in vivo</i> RT .....                         | 96        |
| 4.4.3 Development of a Fibroblast - CD8+ T cell co-culture model RT.....   | 99        |

|  |     |
|--|-----|
| 4.4.4 – CD8+ T cells are activated and proliferate in response to direct contact with irradiated fibroblasts ..... | 101 |
| 4.4.5 CD8+ T cells may contribute to macrophage phenotypic changes. ....   | 103 |
| 4.4.6 Co-culture with CD8+ T cells alters the secretome <i>in vitro</i> .....                                      | 104 |
| 4.4.7 CD8+ T cell mediated tissue damage resolution downregulates macrophage recruitment to irradiated sites.....  | 106 |
| 4.5 Conclusions and Future Work.....   | 108 |
| CONCLUSIONS AND FUTURE WORK .....  | 110 |
| 5.1 Conclusions .....  | 110 |
| 5.1.1 Irradiated Mammary Epithelial Organoids.....   | 110 |
| 5.1.2 Irradiated mammary fibroblast organoids .....  | 111 |
| 5.1.3 Immunocompetent irradiated mammary fibroblast organoids .....  | 112 |
| 5.2 Future Directions.....   | 112 |
| 5.2.1 IL-6 inhibitors.....   | 112 |
| 5.2.2 Macrophage reprogramming therapeutics .....  | 115 |
| 5.2.3 Controlling Normal Tissue Radiation Damage with Radioprotectants and Modified Dosing Regimes.....            | 118 |
| REFERENCES .....   | 121 |
| APPENDICES .....   | 154 |
| APPENDIX A – Appendix Data.....  | 154 |
| APPENDIX B – Code.....   | 176 |
| APPENDIX C – Protocols .....   | 182 |

## LIST OF TABLES

| Table   | Page |
|---|------|
| Table 1.1 Mammary organoid tunability and applicable <i>in vitro</i> assays. ....   | 23   |
| Table 1.2 Summary of recent methods of mammary organoids and their applications. ....   | 24   |
| Table 1.3. The contribution that organoid techniques could make to elucidating mechanisms of radiation damage and their applications to radiation therapy. .... | 37   |
| Table 4.1. Proteins with significant fold change and their associated pathways. ....  | 98   |
| Table 5.1. IL-6 targeting agents in clinical trials as anti-cancer therapeutics. Adapted from <sup>48</sup> . ..  | 114  |
| Table 5.2. Select clinical studies of macrophage reprogramming compounds. Adapted from <sup>22</sup> .<br>.....   | 117  |
| Table 5.3. List of Radioprotective Agents and Their Mechanism of Action. Adapted from <sup>117</sup> . ..   | 120  |
| Table A.1. Table of all proteins analyzed in RPPA. ....   | 162  |
| Table A.2. Table of cytokine abbreviations. ....  | 175  |

## LIST OF FIGURES

| Figure  | Page |
|---|------|
| Figure 1.1 Cancer recurrence following therapy. ....  | 16   |
| Figure 1.2 Characteristics of radiation damage in the mammary gland. ....   | 18   |
| Figure 1.3 Organoid culture conditions and applications. ....   | 22   |
| Figure 2.1. Organoid Isolation Method Workflow. ....  | 50   |
| Figure 2.2. Organoid Plating in 3D Protein Matrices and on Tissue Culture Treated Plastic. ....                                   | 52   |
| Figure 2.3. Organoid Yields from Different Isolation Methods. ....  | 53   |
| Figure 2.4. Non-Adherent Organoid Growth.....   | 55   |
| Figure 2.5. F-actin expression in organoids.....  | 57   |
| Figure 2.6. Evaluating cell-cell interactions through macrophage-organoid co-culture. ....  | 58   |
| Figure 2.7. Evaluating tumor-normal tissue interactions through co-culture. ....  | 59   |
| Figure 3.1: Schematic of <i>in vivo</i> experiments.....  | 73   |
| Figure 3.2. M2 Macrophage infiltration is increased after <i>in vivo</i> irradiation. ....  | 74   |
| Figure 3.3: IL-6 secretion is associated with <i>in vivo</i> RT of normal mammary tissue.....                                     | 76   |
| Figure 3.4. Design of primary mammary organoids.....  | 78   |
| Figure 3.5. Direct co-culture with M0 macrophages influences the irradiated microenvironment.<br>.....                            | 80   |
| Figure 3.6. Organoid macrophage (macs) co-culture facilitates enhanced secretion of MMP9.....                                     | 82   |
| Figure 3.7. Cell infiltration into organoids is enhanced by co-culture of irradiated stroma and<br>infiltrating macrophages. .... | 83   |
| Figure 3.8. IL-6 secretion drives tumor cell invasion post-RT <i>in vitro</i> . ....  | 85   |
| Figure 3.9 IL-6 neutralization <i>in vivo</i> downregulates 4T1 cell invasion after irradiation.....                              | 86   |
| Figure 3.10. Proposed mechanism of 4T1 tumor cell infiltration following normal tissue RT.....                                    | 87   |

|  |     |
|--|-----|
| Figure 4.1. Timeline of in vivo 4T1 recruitment studies. ....  | 96  |
| Figure 4.2. Depletion of CD8+ T cells causes significant changes in protein expression in the wound healing response post in vivo RT. .... | 97  |
| Figure 4.3. T cell isolation produces a pure CD8+ T cell population. ....  | 99  |
| Figure 4.4. T cell infiltration into organoids. ....   | 100 |
| Figure 4.6. CD8+ T cell proliferation is enhanced when co-cultured in irradiated organoids. ...  | 102 |
| Figure 4.7. Co-culture with CD8+ T cells enhances macrophage MHC II expression. ....   | 103 |
| Figure 4.8. MFI values of various cytokines 48 hours after irradiation and co-culture with CD8+ T cells. ....                              | 104 |
| Figure 4.9. Macrophage invasion as a function of RT and immunocompetency. ....   | 107 |

## List of Appendix Figures and Protocols

| <b>Figure</b>  | <b>Page</b> |
|--|-------------|
| Figure A.1. Organoid clumping over time.....   | 154         |
| Figure A.2. Organoid growth in Matrigel Basement Membrane.....   | 155         |
| Figure A.3. Epithelial Marker Expression on Irradiated Organoids.....  | 156         |
| Figure A.4. Macrophage infiltration in normal tissues 10 days post-RT.....   | 157         |
| Figure A.5. M2 Macrophage infiltration is increased 10 days post-RT after CD8+ T cell depletion.<br>.....                                | 158         |
| Figure A.6. SVF organoid characterization. ....  | 159         |
| Figure A.7. Polarized Macrophage and 4T1 Co-Culture Validation.....  | 160         |
| Figure A.8. In vivo validation of IL-6 depletion model. ....   | 161         |
| Figure B.1. Custom script used to analyze the intensity of a fluorophore as a function of distance<br>from the center of a organoid..... | 177         |
| Figure B.2. Custom script used to analyze the intensity of a fluorophore within an ROI.....  | 180         |
| Figure B.3. Custom script used to measure organoid area by creating an ROI using the phase<br>channel of a organoid.....                 | 181         |
| Protocol C.1. Flow Cytometry Sample Prep for Mammary Fat Pads.....   | 182         |
| Protocol C.2. Stromal Vascular Fraction Organoids .....  | 185         |
| Protocol C.3. Bone Marrow Derived Macrophage Isolation .....   | 190         |
| Protocol C.4. CD8+ T cell isolation, activation, and expansion.....  | 194         |

## INTRODUCTION

*Adapted from:* Hacker BC, Rafat M. Organoids as Complex *in vitro* Models for Studying Radiation-Induced Cell Recruitment. *Cellular and Molecular Bioengineering*. 13:341–357, 2020.

### 1.1 Triple Negative Breast Cancer and Radiation Therapy

Breast cancer is the most commonly diagnosed form of cancer and the second most lethal in American women<sup>219</sup>. Unchecked tumor cell growth occurs as a result of dysfunctional regulation of proliferation within terminal mammary ducts. Histologically, most breast cancers emerge as ductal carcinoma in situ (DCIS), where cancer cells are still contained within the basement membrane surrounding the lobular units. Once cancer cells have escaped the basement membrane, the disease progresses to invasive ductal carcinoma (IDC), where cells can metastasize to other organs through the vasculature or lymphatic system<sup>262</sup>. Breast cancer is a heterogeneous disease, but it is phenotypically classified by the presence of three receptors: estrogen receptor (ER), progesterone receptor, and human epidermal growth factor receptor 2 (HER2). For patients with cancer overexpressing one or more of these receptors, treatments have been developed to target the overexpressed markers. However, for patients with triple negative breast cancer (TNBC), hormone treatments and monoclonal antibodies are unsuccessful, reducing treatment options to chemotherapy, surgery, and radiotherapy.

Despite receiving aggressive treatment, TNBC patients encounter high (13-26%) rates of recurrence<sup>2,3,146</sup>. An emerging body of literature suggests that normal tissue damage caused by ionizing radiation may contribute to cancer recurrence through the recruitment of circulating tumor

cells (CTCs), and recurrence risks are higher for lymphopenic patients<sup>122,193,217</sup>. However, many steps in the tumor reseeded process are unknown. Current *in vitro* models available for studying the effects of normal tissue damage are limited in their efficacy. Therefore, there is an overwhelming need to engineer robust *in vitro* models to study radiation-induced normal tissue damage and its relation to tumor cell recruitment and recurrence in TNBC.

One such model that is gaining traction is an organoid model of the mammary gland. Organoids are 3D multicellular constructs that retain relevant architecture and have heterogeneous cell populations, making them an attractive alternative to monolayer cultures that do not recapitulate complex *in vivo* characteristics. In this review, we will outline recent advances in mammary organoid development, and we will examine the advantages of using mammary organoids as models to study normal tissue damage and radiation-induced cell recruitment.

## **1.2 Radiation Therapy, Cancer Progression, and Recurrence**

The relationship between ionizing radiation and cancer progression is complex. Approximately 2/3 of all TNBC patients receive ionizing radiation treatment<sup>2</sup>. Overall, outcomes have been positive as patients receiving radiation therapy have a significantly lower likelihood of locoregional recurrence<sup>2</sup>, with over 80% living recurrence free after treatment for at least 3 years<sup>64,146</sup>.

In addition to decreasing recurrence at the primary site, radiation has been observed to hinder tumor growth at distant sites, termed the abscopal effect. In mouse models of Lewis lung carcinoma and fibrosarcoma, it was shown that p53 upregulated the abscopal effect by decreasing tumor growth after irradiation of normal tissue at a distant site<sup>36</sup>. The presence of T cells appears to be an important mediator of the abscopal effect. Demari *et al.* showed that in mouse models

with contralateral 67NR TNBC mammary carcinoma tumors, irradiation of one tumor significantly decreased growth of the other in wild type but not in immunocompromised nude mice<sup>60</sup>. Furthermore, tumor oxygenation enhances the abscopal effect, and there have been efforts to take advantage of this therapeutically. More recently, Meng and colleagues developed a nanoplatform for inhibiting HIF-1 $\alpha$  in 4T1 mouse breast tumors, which synergistically inhibited tumor growth at primary and distant sites when combined with radiation<sup>161</sup>.

At the same time, an emerging body of literature suggests that ionizing radiation may contribute to recurrence. In 1991, C.F. von Essen described agents like hypoxic cell radiosensitizers, chemotherapy, and surgery that, when combined with radiotherapy, increased metastasis following local tumor irradiation and increased metastatic foci in previously irradiated normal tissues<sup>251</sup>. Particular hallmarks associated with tumorigenesis that are upregulated after radiation have not been fully elucidated and are still areas of active research<sup>96</sup>. For example, angiogenesis may be influenced by radiation. In zebrafish and mouse models, low dose irradiation of 0.8 Gy was shown to promote angiogenesis and 4T1 tumor progression via upregulation of vascular endothelial growth factor receptor 2 (VEGFR2)<sup>227</sup>. Additionally, interactions between irradiated stroma and tumor cells have increased pancreatic tumor invasiveness after doses as low as 5 Gy were applied<sup>179</sup>.

Lymphocyte count has also been implicated in outcomes for patients, both at the primary site and peripherally. High levels of tumor infiltrating lymphocytes are associated with a more positive prognosis<sup>144</sup>. Similarly, peripheral absolute lymphocyte count has been found to predict overall survival in TNBC patients<sup>4</sup>. Additional studies revealed that TNBC patients with lymphopenia or low absolute lymphocyte count were also more likely to experience recurrence after radiotherapy<sup>193,217</sup>. A lymphopenic pre-clinical model was then used to show that tumor cells

from contralateral sites were recruited ten days after normal tissue irradiation, and macrophage infiltration was necessary for tumor cell recruitment<sup>193</sup>.

Insights into recurrence can be gained from examining what is known about the metastatic cascade, which is a multistep process. Before the primary site is surgically removed, metastasis is initiated when tumor cells escape by invading into the surrounding stroma and intravasating into the blood stream or lymphatic system<sup>7</sup>. Tumor cells can survive in the circulation and travel to distant organs. They may extravasate from the bloodstream and either enter a period of dormancy, remaining undetectable, or can rapidly proliferate, eventually forming a clinically detectable metastasis<sup>7</sup>. The most common regions of metastasis of TNBC cells are the lungs, bone, liver, brain, and adrenal glands<sup>10,24,75,257</sup>. The local recurrence process is believed to either be caused by tumor cells that have evaded therapy or to follow mechanisms similar to metastasis (**Fig. 1**). However, rather than colonizing a new site, CTCs may re-colonize the primary site<sup>122</sup>, which is commonly defined as the first site of relapse occurring in either the chest wall, the intact breast, ipsilateral axilla, internal mammary nodes, or supraclavicular fossa<sup>269</sup>.

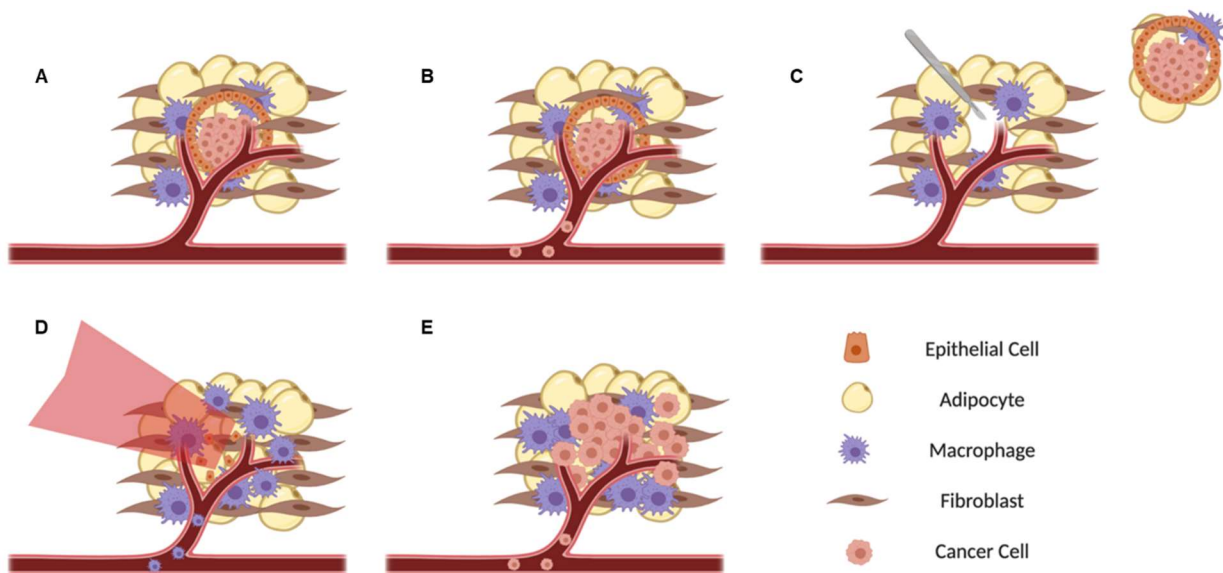


**Figure 1.1 Cancer recurrence following therapy.**

**A.** Most breast cancers begin within the ducts as ductal carcinoma *in situ* (DCIS). **B.** Cancer cells may escape the primary site and enter the circulation, becoming circulating tumor cells (CTCs) and potentially taking root in distant tissues. **C.** Following chemotherapy, the tumor and surrounding stroma is resected surgically. **D.** The area is then treated with ionizing radiation, which causes macrophage recruitment to the site of damage. The extent of this recruitment is influenced by immune status. **E.** CTCs may facilitate cancer recurrence in addition to tumor cells remaining in the treated site, and this outcome is prevalent in immunocompromised patients<sup>193</sup>. Organoids can help elucidate mechanisms of this process, including tumorigenesis<sup>78,278</sup>, escape and stromal invasion<sup>74,107</sup>, and immune and tumor cell recruitment<sup>91</sup>.

These findings convey a complicated relationship between radiotherapy, cancer ablation, and cancer progression. To aid in delving deeper into the mechanisms of recurrence, robust *in vitro* models must be further established to characterize radiation damage to normal tissue and to evaluate how radiation influences tumor and immune cell migration. While *in vivo* studies remain the standard for pre-clinical trials of radioprotectors, radiosensitizers, and cancer therapeutic screening, 3D *in vitro* studies serve as an essential complement and can overcome limitations of *in vivo* mouse models, such as differences in biology, lack of control over complex biological systems, and discrepancies between therapy regimens in mice and humans. Already, murine

mammary organoids, which are mammary gland derived primary cells grown in 3D, are being used to model macrophage and tumor cell recruitment after normal tissue irradiation<sup>91</sup>. This work can be further expanded to determine the role of normal tissue damage in recurrence.

### **1.3 Radiation-Induced Damage in the mammary gland**

Ionizing radiation damages cellular DNA. In the mammary gland, the response to radiation is multi-faceted due to the diverse tissue composition (**Fig. 2**). Proliferation rate is correlated to the extent of response to radiation damage<sup>198</sup>. Highly proliferative cells, like epithelial cells in the ducts or lobes, rapidly undergo apoptosis and delayed secondary apoptosis associated with mitotic catastrophe<sup>202</sup>. Cells that proliferate more slowly, like adipocytes, may enter a state of senescence rather than apoptosis, and their response to radiation damage occurs more slowly, sometimes taking months or years<sup>198</sup>. Cell cycle phase, oxygenation status, and interactions with other cell types all influence radiation response. There has therefore been a shift from examining response of homogeneous cell populations to analyzing damage when multiple cell types are present<sup>263</sup>. Because of the different cell populations in the mammary gland, there is great interest in understanding the interactions between epithelial, adipose, stromal, and endothelial cells in response to radiation.

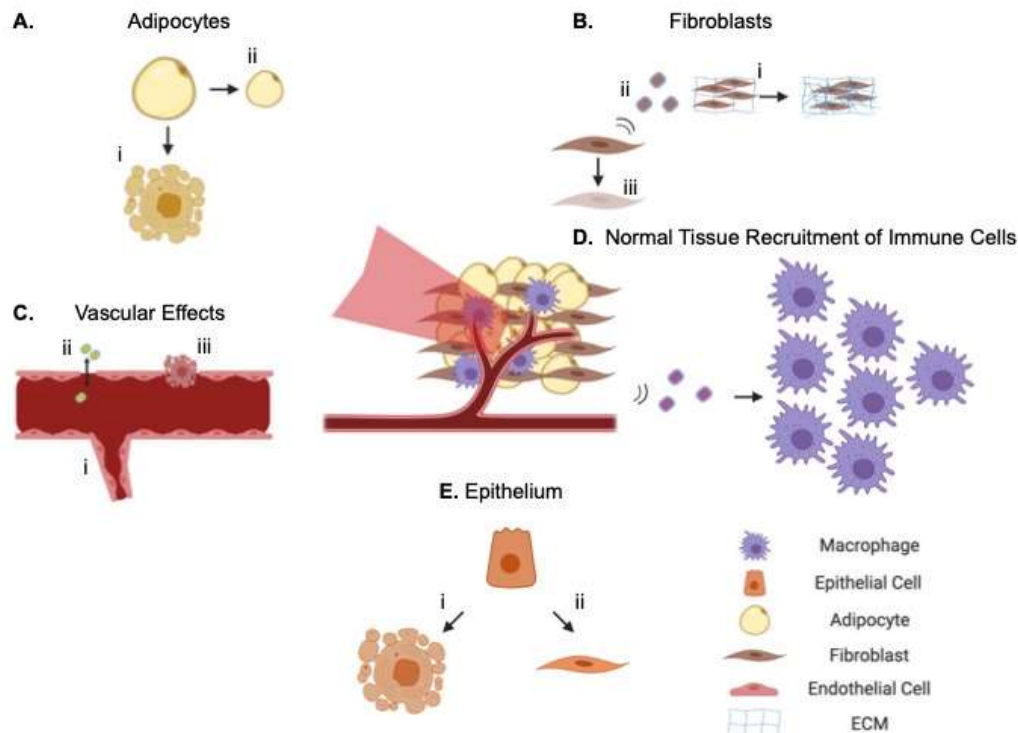


**Figure 1.2 Characteristics of radiation damage in the mammary gland.**

**A.** After radiation, adipocytes (i) undergo apoptosis, and (ii) decrease in size<sup>188</sup>. **B.** Fibroblasts (i) increase production of ECM components and cause fibrosis<sup>197</sup>, (ii) secrete a variety of cytokines in the pro- and anti-inflammatory response, and (iii) can be induced into a state of senescence<sup>239</sup>. **C.** Radiation can have a variety of effects on the endothelium and vasculature, including (i) angiogenesis<sup>227</sup>, (ii) a temporary increase in endothelial layer permeability<sup>16</sup>, (iii) apoptosis of endothelial cells<sup>197</sup>, and CD11b+ cell induced vasculogenesis<sup>6</sup>. **D.** Secreted factors from the irradiated stroma recruit macrophages<sup>193</sup> and CD11b+ monocytes<sup>6</sup>. **E.** Radiation induces apoptosis (i) in epithelial cells or (ii) induces epithelial-to-mesenchymal transition<sup>11</sup>. For each cell type, adipose and fibroblast spheroids<sup>124,125,264</sup>, microvascular networks<sup>254</sup>, and epithelial organoids<sup>71,91,173</sup> can be used as models to isolate individual contributions of the radiation response.

Most breast cancers arise from epithelial cells. Radiation therapy can be used to target tumor cells or can be applied to the area surrounding the resected tumor post-surgery. Morphologically, mammary epithelial tissue exposed to ionizing radiation most commonly undergoes moderate atrophy<sup>72</sup>. Within the stromal compartment, fibrosis, or excess deposition of

extracellular matrix (ECM), is readily apparent. Treatment over time also has an effect on tolerance of radiation damage, which decreases with each subsequent dose<sup>32</sup>. Inflammation of blood vessels is observed as a late effect of radiation within mammary tissue<sup>72</sup>. In the vasculature, small capillaries are the most sensitive to ionizing radiation as they are composed of a single layer of endothelial cells<sup>246</sup>. Ionizing radiation can disrupt the adhesion of endothelial cells, an observation marked by disruption of VCAM 1 expression in 2D and 3D endothelial cultures<sup>111</sup>.

The sheer number of proteins secreted by adipocytes (>400) indicates their important role in cell communication and cross-talk<sup>277</sup>. Therefore, changes in secreted cues after irradiation are of particular interest. Crosstalk between adipocytes and tumor cells have been shown to increase tumor cell resistance to therapy. Bochet *et al.* co-cultured murine 3T3F442A cells that were differentiated into adipocytes with SUM159PT mammary carcinoma cells. At doses of 5 Gy, tumor cells in co-culture displayed higher survival fraction and lower mitotic catastrophe than tumor cells cultured alone<sup>26</sup>. Adipocytes have been shown to be sensitive to radiation *in vivo*. In inguinal fat pads, adipocytes exposed to 7 Gy irradiation were reduced in size and number<sup>188</sup>. In addition to causing direct toxicity to cells by double strand DNA breaks, application of ionizing radiation can cause indirect effects through the generation of short-lived reactive oxygen species. In the mammary gland, where there is a large percentage of cells with fat, this can lead to excessive amounts of peroxidation of unsaturated lipids. Lipid peroxidation has been quantitated by malondialdehyde concentration<sup>240</sup> and has been correlated with tumor progression<sup>194,224,258</sup>.

Crosstalk between mammary stroma and parenchyma can play a role in response to radiation, and changes in the stromal compartment can contribute to cancer progression and recurrence. Nguyen and colleagues showed this by adapting a previously developed mammary chimera model<sup>20,174</sup>. In this model, the epithelium in the inguinal mammary gland was removed,

mice were exposed to whole body low dose irradiation, and fragments of mammary epithelium lacking the tumor suppressor gene *p53* were transplanted into the cleared mammary gland. Rather than being used to treat cancer, ionizing radiation was used to initiate tumor growth and progression, and it was found that radiation induced aggressive, ER negative tumor growth. This is evidence that radiation induced changes in the stromal compartment can affect outcomes in the epithelium. One of the major limitations of the chimeric model was that tumor detection in mice required almost a full year. *In vitro* organoid models could replicate these interactions in a much shorter time frame.

Outcomes for living cells can also be altered by dead cells. A phenomenon called accelerated repopulation has been known for decades<sup>231</sup>. In this process, the few cancer cells that may survive radiotherapy proliferate at a markedly increased pace to re-establish the tumor. Radiation-induced death of multiple cell types has been shown to contribute to repopulation, including cancer cells and fibroblasts<sup>104</sup>, and this may be mediated by Caspase-3 signaling. However, more complex co-culture models for further probing this process have not been developed.

In addition, the response to radiation therapy can be significantly impacted by the endothelium. Ahn and Brown have shown that after radiation of tumor and normal tissue, recruited CD11b<sup>+</sup> bone marrow derived cells (BMDCs) can drive tumor regrowth by upregulating vasculogenesis<sup>6</sup>. This recurrence can be prevented by blocking infiltration of BMDCs and preventing vasculogenesis, which has been shown in a glioblastoma model<sup>123</sup>. In this study, the authors found that inhibiting the HIF pathway was effective at reducing tumor recurrence after radiotherapy, but this inhibition did not have an impact on recurrence in the absence of

radiotherapy. Taken together, these studies highlight the importance of modeling radiation response with *in vitro* systems that incorporate multiple cell types.

#### 1.4 Mammary and Tumor Organoids

Mammary organoids, which are 3D multicellular constructs that retain aspects of the organ's architecture, upregulate signaling pathways that are lost in 2D culture<sup>253</sup> and have heterogeneous cell populations, making them representative models of the mammary gland. They can be generated from a variety of sources (**Fig. 3, Table 1**), including patient derived reduction mammoplasties<sup>130,142</sup>, cell lines<sup>169</sup>, mouse mammary epithelial ducts<sup>91,106,173</sup>, co-cultures of luminal and myoepithelial cells<sup>223</sup>, or single mammary stem cells<sup>112</sup>. Mammary organoids are cultured in a various vessels or configurations, most often in matrices designed to mimic the basement membrane surrounding ductal lumina<sup>142,172,173</sup>. Other culture conditions incorporate microfluidic systems to simulate shear stress and oxygen and nutrient diffusion<sup>13</sup> or low adhesion culture conditions, which force cells to self-adhere rather than adhere to tissue culture treated plastic and causes a loss of dimensionality<sup>91</sup>. There have been many exciting recent developments in the use of mammary organoids to study biological processes (**Table 2**), which are described below.

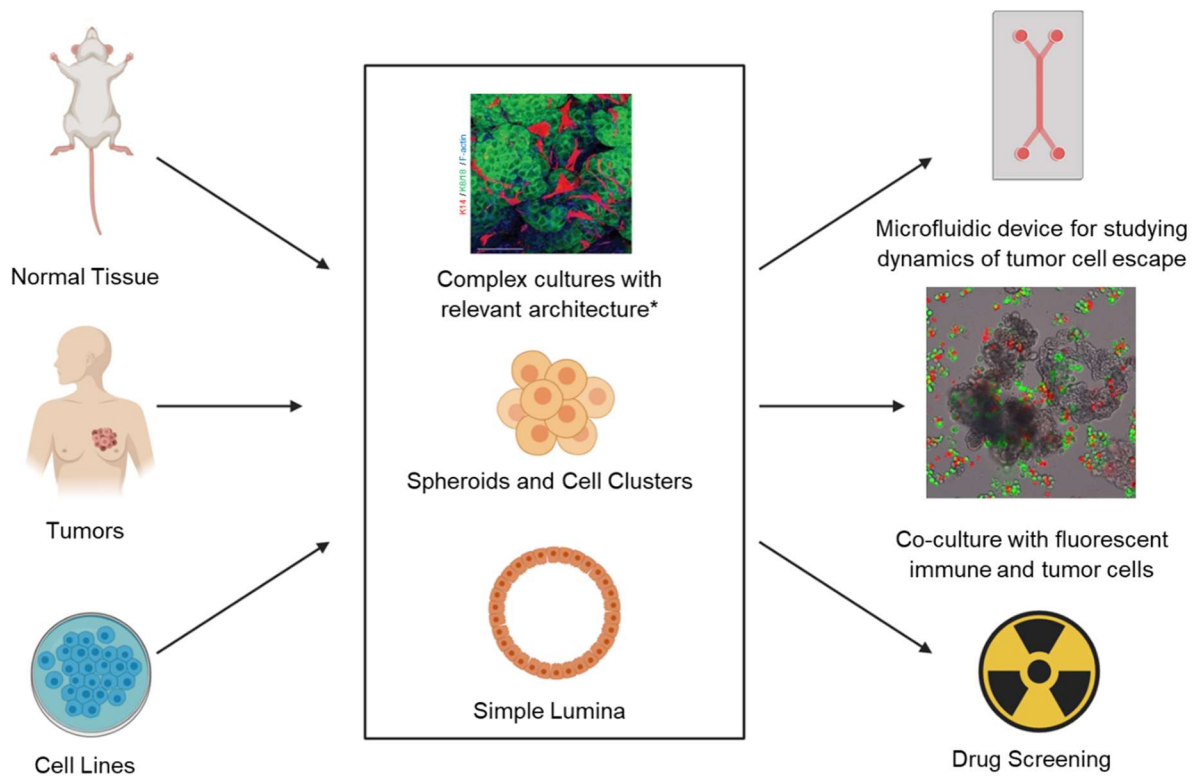


**Figure 1.3 Organoid culture conditions and applications.**

\*Adapted from Jamieson et al.<sup>112</sup> Mammary organoids are derived from normal, non-tumor tissue or tumors from various mammalian sources. They can also be derived from cell lines. Organoids are distinct from monolayer cultures in that their culture conditions facilitate the adoption of a 3D phenotype. They can be forced to adapt a spheroid form when seeded into low adhesion plates, cultured into lumen that recapitulate localized keratin and cadherin expression, or form complex cultures when mammary stem cell niche factors are included. These studies are useful in supplementing in vivo observations, including determining dynamics of tumor cell escape from the primary site, characterizing kinetics and cell-cell interactions between normal tissues and immune cells, and testing therapeutics on tumor cell growth.

**Table 1.1 Mammary organoid tunability and applicable *in vitro* assays.**

| Sources of Organoid Tissue  | Culture Vessels  | Assays   | Outputs   | References   |
|---|--|--|---|--|
| Primary Mammary Epithelium  | Low adhesion plates<br>Basement membrane                   | Immune cell co-culture<br>Invasion assays<br>Live cell imaging     | Cystic spherical organoids                                  | Hacker <sup>91</sup><br>Nguyen-Ngoc <sup>173</sup> |
| Patient derived reduction mammaplasty   | Micro-patterned microwells                                 | Flow cytometry and immunofluorescence to analyze lineage diversity | Organized bilayered alveoli and ducts                       | LaBarge <sup>130</sup>                             |
| Patient derived reduction mammaplasty enriched for regenerative CD10 <sup>+</sup> CD49 <sup>hi</sup> /EPCAM <sup>-</sup> cells                              | Floating collagen gels                                     | Branching  | Structures with terminal ductal-lobular units               | Linnemann <sup>142</sup>                           |
| Tumor organoids from MMTV-PyMT mice   | Microfluidic device with fluid flow and chemokine gradient | Organoid migration   | Tumors that migrate through the device                      | Hwang <sup>107</sup>                               |
| Single sorted basal (K14 <sup>+</sup> ) or luminal (K8/18 <sup>+</sup> ) CD24 <sup>+</sup> CD29 <sup>+</sup> mammary stem cells from confetti reporter mice | Basement membrane extract                                  | Tissue dynamics<br>Cell fate decisions<br>3D confocal microscopy   | Complex mammary glands over 300 $\mu$ m in size             | Jamieson <sup>112</sup>                            |
| Murine mammary epithelium isolated into varying ratios of myoepithelium and luminal epithelium  | Matrigel or Collagen I                                     | Live cell imaging<br>Cell invasion and dissemination               | Cystic organoids that can invade into the basement membrane | Sirka <sup>223</sup>                               |

**Table 1.2 Summary of recent methods of mammary organoids and their applications.**

| Novel Organoid Development   | Applications   | References                         |
|--|--|------------------------------------|
| Irradiated organoids recapitulate pre-clinical observations of increased macrophage recruitment  | Co-Culture;<br>Radiation Damage                                      | Hacker <sup>91</sup>               |
| Communication of ECM and intracellular proteins impacts acinar and tumor formation   | Development;<br>Tumorigenesis  | Furuta <sup>78</sup>               |
| BCL11b transcription factor inhibits differentiation of mammary stem cells   | Regenerative Medicine;<br>Development                                | Miller <sup>164</sup>              |
| Macrophages are recruited to tumors and facilitate tumor cell metastasis   | Tumorigenesis;<br>The Metastatic Cascade                             | Linde <sup>141</sup>               |
| Patient derived explants of breast tumors allow for rapid evaluation of drug efficacy in hormone-dependent cancers                               | Drug Screening   | Centenera <sup>41</sup>            |
| Human breast epithelial progenitors can be expanded more rapidly in organoid culture than 2D culture   | Regenerative Medicine;<br>Development                                | Chatterjee <sup>43</sup>           |
| Transcriptome analysis on MCF10A M1-M4 organoid culture reveals that lncRNA stabilizes mRNA of an oncogene                                       | Tumorigenesis  | Jadaliha <sup>110</sup>            |
| Formin Dia1 is necessary for invasion of epithelium into the basement membrane   | Development;<br>Tumorigenesis  | Fessenden <sup>74</sup>            |
| Small molecule inhibitor WRG-28 blocks discoidin domain receptor 2 (DDR2), inhibiting tumor cell invasion and migration in a TNBC organoid model | Drug Screening   | Grither and Longmore <sup>87</sup> |
| MAP3K1 deletion confers resistance to AKT inhibitor in organoid model of MCF10A cells  | Drug Screening;<br>Therapeutic Resistance                            | Avivar-Valderas <sup>12</sup>      |
| Glucocorticoids contribute to loss of myoepithelium, allowing DCIS to become IDC   | Tumorigenesis  | Zubeldia-Plazaola <sup>278</sup>   |
| Cancer cells become more invasive in hypoxic and limited nutrient conditions   | Tumorigenesis;<br>Microfluidic Systems                               | Ayuso <sup>13</sup>                |
| Long-term culture of patient-specific breast cancer organoids  | Drug Testing;<br>Personalized Medicine                               | Sachs <sup>203</sup>               |
| Biochemical and biomechanical cues cause K14+ leader cells to initiate migration of tumor cells in primary tumor organoids                       | Metastatic Cascade;<br>Tumorigenesis;<br>Migration;<br>Microfluidics | Hwang <sup>107</sup>               |

### 1.4.1 Regenerative Capacity

Culturing organoids long-term, similar to primary cells, is challenging. Timescales for primary-derived organoid culture are on the order of two weeks<sup>214</sup>, which limits longer term studies. To lengthen these timescales, there has been much interest in identifying stem cells or stem-like cells that are highly proliferative and have high regenerative potential as well as identifying factors that contribute to generation of organ-like structures while maintaining stem cell maintenance and homeostasis<sup>43,164</sup>. Much of the work in patient derived mammary organoids has been inspired by developing organotypic models of colorectal cancer due to their ease of accessibility from colonoscopies<sup>206</sup>. Fundamental studies identifying stem-like cells within the intestine have been done<sup>50</sup>, and factors that contribute to stem cell renewal and tissue differentiation have been characterized<sup>207</sup>. However, the process of discovery of factors that allow for long term growth and differentiation of mammary organoids is still underway, and some of the factors that facilitate culture of intestinal epithelial organoids do not necessarily translate to mammary epithelial organoids. In 2016, Jardé and colleagues showed that epidermal growth factor (EGF), a protein that had been used for GI and prostate organoid maintenance, did not contribute to long term mammary organoid growth<sup>114</sup>. Instead, they found that culturing in media supplemented with Neuregulin-1, a member of the EGF ligand family, caused faster growth, more relevant architecture, and self-organization into basal and luminal compartments. The authors cultured the organoids for over two months. They also showed regenerative capacity by injecting organoids into cleared epithelium, and these results show regeneration of the epithelial ductal tree that was confirmed by an additional study<sup>180</sup>.

Mammary organoids can also be induced from differentiated cells. Rather than taking the approach of isolating tissue stem cells, Panciera *et al.* de-differentiated terminally differentiated

luminal and basal cells<sup>180</sup>. The authors introduced dox-lentiviral vectors and induced cellular YAP/TAZ expression. They generated organoids that could be cultured at least 12 months (>25 passages) and had very similar cytokeratin fluorescent protein patterns and gene expression to organoids derived from mammary stem cells.

#### **1.4.2 Extracellular Matrix (ECM) and Cell-Matrix Interactions**

Since Lasfargues established a method using collagenase to digest and isolate adult mouse mammary epithelium in 1957<sup>136</sup>, mammary organoids have been used for studying mechanisms of organogenesis, development, metastasis and cancer cell progression. There have been many influential discoveries elucidating mechanisms of cell-matrix interactions. The ECM has been shown to influence organoid growth, conferring insights into *in vivo* mammary development. The development of mammary organoids embedded in a basement membrane has been shown to depend on material stiffness, which has ranged from 120 to 200 Pa<sup>8</sup>, and in tumor microenvironments can be as high as 3.2 kPa<sup>40</sup>. In one recent study, Linnemann *et al.* produced organoids from single human mammary epithelial cells, and these organoids had morphology similar to terminal ductal-lobular units<sup>142</sup>. Organoids were cultured in floating collagen gels, which have reduced stiffness compared to attached hydrogels<sup>8</sup>. Organoids produced more alveolar structures when grown in free-floating collagen matrix. They also displayed accurate co-localization of basal and luminal markers and exhibited a higher propensity for myoepithelial contractility<sup>142</sup>. Interestingly, atomic force microscopy measurements showed that floating collagen gels exhibited stiffnesses more similar to *in vivo* conditions than adherent collagen gels<sup>8</sup>.

Additionally, it was shown that ECM composition regulates mammary morphogenesis. Furuta and colleagues investigated the role of laminin proteins affecting morphogenesis signaling

pathways in a patient derived mammary organoid model<sup>78</sup>. They discovered that laminin-111 upregulated production of nitric oxide, which inhibited tumorigenesis. Inhibition of nitric oxide resulted in poor acinar formation and organization, and instead the cells displayed a less defined, more proliferative phenotype. Finally, cancer progression was also slowed when matrix-metalloproteinase laminin degradation was inhibited. This study shed light on mechanisms of communication between the ECM and inter-nuclear proteins in regulating acinar formation and tumor progression.

Furthermore, tumor spheroids and stromal cells have been shown to alter ECM properties, which could in turn influence cell behavior<sup>154</sup>. Much remains unknown about how these cell-generated forces affect the microenvironment. In one 3D model, dense fibrotic environments resulted in plastic ECM remodeling<sup>155</sup>. In another study, Acerbi *et al.* performed mechanical analysis of human breast tumor tissues<sup>1</sup>. They found that breast cancer progression and aggressiveness are linked with collagen linearization. These effects are further enhanced by inflammation and transforming growth factor beta (TGF- $\beta$ ) signaling, which has implications for the role of radiation in tumor progression. In a 3D breast cancer cell model, Han *et al.* discovered that contractions of MDA-MB-231 cells can alter the mechanics of the surrounding ECM in collagen, fibronectin, and Matrigel model systems<sup>95</sup>. These modifications potentially provide a mechanism of mechanical communication between cells. As *in vitro* models become more realistic and complex, organoids and other 3D models are playing a crucial role in analyzing the biomechanics and biophysical mechanisms of cell-matrix signaling, which has particular relevance in evaluating radiation-induced fibrosis<sup>230</sup>.

### 1.4.3 Modeling Metastasis

In addition to evaluating factors that contribute to development and mammary gland homeostasis, organoids have also been used to examine various facets of the metastatic cascade. Transcriptome analysis of MCF-10A organoids revealed that long non-coding RNA sequences were important in preventing breast cancer progression as they supported stability of tumor suppressor mRNA sequences<sup>110</sup>. Organoids have also been used to identify invasive promoting factors like Dia-1 dependent adhesions and glucocorticoids<sup>74,278</sup>.

Organoid studies have identified mechanisms that would be difficult to image *in vivo* and impossible to recreate with simple 2D *in vitro* cultures. For example, Hwang *et al.* developed an organoid model from transgenic mice<sup>107</sup>. In this model, cytokeratin 14 positive (K14+) basal epithelial cells expressed GFP, and primary breast tumor organoids were obtained from mice and cultured in a microfluidic system. A gradient of stromal cell derived factor 1 (SDF1), a cytokine commonly found in the mammary stroma, was induced, and organoids were imaged over time. It was found that K14+ basal cells initiated collective tumor cell migration toward this factor, implicating them as leaders of collective tumor cell escape from the primary site.

Differences in microenvironmental composition (i.e. stromal vs. basement membrane) may influence cancer cell invasiveness, providing insights into the metastatic cascade. In an organoid model, primary human breast carcinomas were grown in different ECM gels to compare their phenotype. Organoids cultured in collagen I matrix (a stromal mimicking microenvironment) were more protrusive and had a higher percentage of disseminated cells than those cultured in Matrigel (a basement membrane-mimicking microenvironment)<sup>172</sup>. These data suggest that as cancer cells escape the lumen, contact with a stromal microenvironment induces a more metastatic phenotype.

#### 1.4.4 Drug Screening

Due to their faithful recapitulation of tissue architecture and ease of accessibility, organoids are commonly used for drug screening. While some studies have focused on drug testing for organoids derived from cell lines<sup>12,87</sup>, there have been recent developments to improve drug screening of patient derived breast cancer organoids, which have contributed greatly to improvements in personalized medicine<sup>41,203</sup>. In 2018, a biobank of breast cancer organoids was established<sup>203</sup>. These authors were motivated by the fact that systemic therapies are not specific enough for individual cases of breast cancer; that is, heterogeneous cancer phenotypes can display a variety of responses to therapies. This approach can be used for drug development and analysis of *in vitro* drug response in a heterogeneous population of breast cancers.

Methods of delivering drugs to organoids have also been refined. Organoids grown in 3D matrix (e.g. Matrigel) are dense and compact, limiting delivery of genetic material. Work by Laperroussaz *et al.* examined a method for transgene expression in organoids<sup>135</sup>. Previous strategies for introducing viral vectors included dissociating organoids into single cells before transfection and then re-embedding in Matrigel. However, this method is essentially a 2D transfection as the spatial architecture and polarity is lost after dissociation. Instead, the authors used a microfluidic device to embed organoids into Matrigel microbeads, introduced lentiviral vectors via electroporation, and demonstrated high efficacy of siRNA induction while retaining high organoid viability.

### 1.4.5 Co-Culture Models with Immune Cells

The vast majority of 3D co-culture models with immune cells have used tumor spheroids as opposed to normal tissue organoids. The most common co-culture model has utilized tumor cells and macrophages<sup>90,141,236,261</sup>. Macrophages can be seeded within the tumor spheroid to evaluate infiltrated tumor associated macrophages (TAMs) or around the spheroid within the surrounding matrix as a model of macrophages within the stroma. The use of human-derived monocytes provides the most biologically relevant model; however, many studies use the murine RAW 264.7 cell line or bone marrow-derived macrophages as a macrophage model.

To examine the effect of tumor cells on the TAM phenotype, Tevis *et al.* developed a co-culture model of RAW 264.7 macrophages and MDA-MB-231 TNBC spheroids<sup>236</sup>. They determined that cancer cells upregulated macrophage secretion of IL-10 when macrophages were in close proximity or contact with the cancer spheroids, suggesting an increased immunosuppressive macrophage phenotype. Other co-culture studies have studied the effect that macrophages have on tumor cells. Winslow *et al.* generated spheroids from human MCF7 cancer cells and co-cultured these spheroids with human-derived CD14+ monocytes to investigate the impact that monocytes have on tumor cell gene expression<sup>261</sup>. To evaluate changes in transcription in tumor cells, they dissociated the spheroids, sorted the tumor cells, and collected RNAseq data. They determined that co-culture with monocytes downregulated CYP1A1, which can act as an activator of carcinogens. This model presents a straightforward technique for determining how co-cultures may change oncogene expression.

Tumor spheroid and macrophage co-cultures have also contributed to knowledge of the metastatic process. In a recent study, Linde *et al.* examined how myeloid cells in the mammary gland contributed to cancer cell dissemination<sup>141</sup>. Using HER2+ tumor spheroid organoids cultured

from transgenic mice, they found that mammary-derived macrophages co-localized with organoids and that this co-localization was associated with CCL2 signaling. CCL2 signaling was further associated with attracting TAMs and inducing an increased invasive phenotype in HER2+ cancer cells.

Other co-culture studies have included a stromal component within tumor spheroids. Kuen and colleagues developed a 3D spheroid model consisting of both pancreatic cancer cells and fibroblasts<sup>128</sup>. They co-cultured human monocytes with the spheroids and found that the co-culture polarized monocytes toward an immunosuppressive, M2-like phenotype. Polarized macrophages also displayed immunosuppressive properties when co-cultured with T cells, reducing proliferation of CD3+ T cells and inhibiting activation of CD8+ and CD4+ T cells. Kuen's spheroid co-culture model reflected the aggressive, immunosuppressive nature of the pancreatic cancer microenvironment and could serve as a tool to elucidate further mechanisms of tumor progression.

Tumor organoids have additionally been co-cultured with T cells, a model that is becoming increasingly relevant given the importance of immunotherapy. Dijkstra *et al.* developed a patient-derived colorectal cancer organoid model<sup>62</sup>. By co-culturing autologous T cells with cancer organoids, they applied principals of adoptive transfer in a 3D environment, activating and expanding tumor reactive T cells. In this model, T cells killed tumor organoids that had proficient expression of major histocompatibility complex (MHC) class I but did not prevent proliferation of MHC I-deficient tumor organoids. This is an exciting application of spheroid-immune co-culture that may lead to the advancement of personalized medicine.

Although most 3D co-cultures with immune cells have occurred in the context of tumor spheroids, some studies have paired normal tissue organoids and immune cells. Normal tissue

organoid models co-cultured with immune cells can provide insights into the kinetics of cell infiltration into normal tissue. For example, a novel co-culture system of intestinal epithelial organoids and intraepithelial lymphocytes (IELs) was developed<sup>177</sup>. Using time-lapse imaging, the dynamics of IEL interactions with the intestinal tissue and how IL-2, IL-7, and IL-15 affected lymphocyte infiltration were analyzed. The authors tracked  $\alpha\beta$ T and  $\gamma\delta$ T cells over the course of two hours and quantified parameters like mean speed, track length, and alignment of individual lymphocytes. Significant differences were not found between their variables; however, this technique is a powerful way to characterize cell motility in an *in vitro* system.

Analysis of cell migration and motility has mainly been used to model organogenesis, development, and mammary morphogenesis. Huebner *et al.* used 3D culture to study ductal elongation in the mammary gland and tracked individual fluorescent cells in mammary organoids using time-lapse imaging. The authors discovered a model of elongation, distinguishing how receptor tyrosine kinases influence both proliferation and cell migration within the mammary duct<sup>106</sup>. While live cell time-lapse imaging has elucidated aspects of mammary development, similar techniques would prove valuable to evaluating individual interactions between immune cells and tissue, providing insight into cell morphology and co-localization kinetics. These studies illustrate the potential for culturing immune cells with organoid models of normal tissue damage.

#### **1.4.6 Other Technical Outputs**

The increased dimension offered by organoids also brings with it increased potential in complex quantitative outputs. Techniques commonly used for 2D cell culture (e.g. fluorescence microscopy, transcriptomics) can also be applied to organoids. Size and shape diversity in these models have often been ignored, yet differences in morphology may significantly impact results.

In a recent study, Zanonoi *et al.* used software to assess how morphological parameters affect the response of lung cancer spheroids to various treatments<sup>268</sup>. Using 3D reconstructions of brightfield organoid images, they evaluated spheroidization time, or the time for cellular aggregation into spherical constructs. They also determined that homogeneously sized spheroids had different viability profiles than non-homogeneously sized spheroids, which have potential implications for studying drug and radiation response.

Spheroid morphology has also been assessed in patient-derived tumor organoids. Borten *et al.* developed Matlab-based software to examine morphologic parameters like area, solidity, and eccentricity of tissues<sup>28</sup>, providing a more accessible way to increase the throughput of organoid data. Interestingly, the investigators also evaluated morphological parameters, like solidity, convex area, and kurtosis, with transcriptomic data obtained from RNA sequencing. Integrating these data may reveal insights into the mechanisms regulating organoid development.

Fluorescent image analysis can provide additional complex information in organoid models. For example, in a biomechanical study of tumor cell invasion into the ECM, Kopanska and colleagues used fluorescent staining of collagen fibers to enable quantitation of fiber orientation and alignment<sup>126</sup>. Additionally, fluorescent tracking beads validated displacement velocity maps, allowing for visualization of contractile flow speed and magnitude as a function of time. The results obtained from this tension-based model determined how biomechanical forces in the ECM influence invasion.

## **1.5 Investigating Normal Tissue Radiation Damage and cell infiltration**

Current 2D *in vitro* models do not recapitulate tissue complexity and cell heterogeneity to properly assess the effects of radiation damage to normal tissue. Organ specific stem cells are

necessary for homeostasis and wound healing in multiple organs<sup>162,244</sup>. They are progenitors of differentiated, functional cells, and radiation induced stem cell damage can severely disrupt homeostasis, especially in regions of high proliferation and turnover. While many 2D assays of radiotherapy damage do not incorporate stem cells into their culture<sup>89,225</sup>, the impact of low dose radiation on salivary gland stem cells has recently been studied<sup>171</sup>. The survival of stem cell derived organoids exposed to 4x0.25 Gy fractionated radiation was shown to be much lower than cells exposed to 1 Gy in a single dose, suggesting that salivary stem cells may have a low dose hypersensitivity. This deviates from preconceptions about a linear response to increasing radiation doses.

Many cytokines are secreted in response to radiation damage<sup>209</sup> and have complex and sometimes contradictory roles. For example, normal tissue damage caused by ionizing radiation is known to result in the steady production of both anti-inflammatory cytokine TGF- $\beta$ <sup>18</sup> and pro-inflammatory factor IL-6<sup>250</sup>. Depending on stage of progression, each of these cytokines can paradoxically behave as tumor suppressors or oncogenic factors in the tumor microenvironment<sup>25,242</sup>. Despite extensive studies of normal tissue damage after radiation, there are no approved therapies for radiation-induced fibrosis. While *in vivo* studies of radiation damage to normal tissue and tumor cell recruitment have limited control over biological variables, most *in vitro* models in this area are limited in their efficacy<sup>111</sup>. There is therefore much interest in developing biologically realistic models to isolate cell-cell interactions and cell-matrix interactions<sup>91</sup>. Normal tissue organoids can be used as essential complements to studies of radiation damage mechanisms and their applications to radiation therapy (Table 1.3). Current areas of interest include modifying radiation dosing regimens<sup>30,33,145,167,168,208,221</sup>, applying normal tissue radioprotectants or tumor

radiosensitizers<sup>21,51,88,115,147,175,212,234,274</sup>, and modulating immune cell infiltration with other locally targeted therapies<sup>46,67,105,143,245</sup>.

3D organoid models for studying radiation damage to normal tissue have been examined. A mammary organoid model from epithelial ducts isolated from murine mammary glands was developed to evaluate the influence of radiation on immune cell recruitment<sup>91</sup>. Organoids were irradiated *ex vivo* and co-cultured with RAW 264.7 macrophages. In this model, macrophages preferentially migrated toward irradiated organoids as was shown in previous pre-clinical studies<sup>193</sup>.

Furthermore, lack of cell heterogeneity can limit conclusions that can be drawn about normal tissue damage. The gut is a commonly studied organ as indirect exposure to radiation can have devastating effects on nutrient uptake. In a study of radiation-induced damage from immune cells to intestinal tissue, co-cultured Caco-2 cells with peripheral blood mononuclear cells (PBMCs) showed increased permeability of the intestinal barrier induced by activity from PBMCs<sup>170</sup>. However, recent studies have suggested that endothelial cells drive intestinal radiation response<sup>76,80,181</sup>. For example, an organotypic gut-on-a-chip model was used to show that the vascular endothelium mediates radiation damage<sup>111</sup>. This suggests that studies without the endothelial compartment may not accurately replicate radiation response.

The ability to obtain clear images on a single cellular scale allows for identification of temporal cell behaviors, such as kinetics of radiation-induced tumor and immune cell infiltration, which can be quantified via cell migration and motility analysis<sup>14,62,106,177</sup>. Mammary epithelial organoids are being developed to visualize the kinetics of TNBC cell and macrophage recruitment following radiation damage. The accessibility of conditioned media allows for identification of cues secreted by organoids. Variables related to tumor cell recurrence can be evaluated as a

function of radiation damage, including tumor cell invasiveness in invasion and migration assays and macrophage chemotaxis. Proteins and cytokines that play a role in macrophage facilitated tumor cell infiltration and identified from organoid models can be further validated *in vivo*. Additional characteristics of the mammary gland should be incorporated in future studies, including adipokines, fibroblasts, and immune cells such as neutrophils, which have been associated with tumor progression and recurrence<sup>189,217</sup>. The tunability of this model is therefore a great strength and allows for increased biological relevance in understanding mechanisms of recurrence.

**Table 1.3. The contribution that organoid techniques could make to elucidating mechanisms of radiation damage and their applications to radiation therapy.**

| Area of interest                    | Specific treatment  | Models used   | References                    |
|-------------------------------------|---|---|-------------------------------|
| Radiation Dosage Scheme             | Design of complex dosage schemes  | Computational Model   | López Alfonso <sup>145</sup>  |
| Radiation Dosage Scheme             | FLASH Radiation   | <i>In vivo</i> : non-tumor bearing C57BL/6 J mice<br>No <i>in vitro</i> studies   | Simmons <sup>221</sup>        |
| Radioprotector Studies              | Superoxide dismutase mimic  | <i>In vivo</i> : Rhesus macaque<br>No <i>in vitro</i> studies   | Cline <sup>51</sup>           |
| Radioprotector Studies              | Treatment of 3,3'-Diindolylmethane, an anti-oxidant agent, to minimize gut injury | <i>In vivo</i> : non-tumor bearing C57BL/6 J mice<br><i>In vitro</i> : HIEC-6 cell lines (2D)   | Lu <sup>147</sup>             |
| Radiosensitizer Studies             | Inhibition of histone deacetylases  | <i>In vivo</i> : Bladder cancer cell xenografts<br><i>In vitro</i> : Bladder cancer cell lines (2D)   | Groselj <sup>88</sup>         |
| Radiosensitizer Studies             | Genistein and inhibition of Bcl-xL  | <i>In vitro</i> : NSCLC cell lines (2D)<br><i>In vivo</i> : Subcutaneous (Sub-q) A549 tumor injections                                      | Zhang <sup>274</sup>          |
| Radiosensitizer Studies             | PARP inhibitors and fractionated doses  | <i>In vivo</i> : Sub-q xenografts<br><i>In vitro</i> : Lung carcinoma cell lines (2D)   | Jiang <sup>115</sup>          |
| Immune cell infiltration modulation | cGAS-STING pathway  | <i>In vivo</i> : STING <sup>-/-</sup> C57BL/6 J mice<br><i>In vitro</i> : Primary fibroblasts (2D)  | Dou <sup>63</sup>             |
| Immune cell infiltration modulation | Trex1 exonuclease release   | <i>In vivo</i> : Sub-q murine and human TNBC tumor injections<br>Sub-q patient derived xenografts<br><i>In vitro</i> : TNBC cell lines (2D) | Vanpouille-Box <sup>245</sup> |
| Immune cell infiltration modulation | High intensity ultrasound to replace neo-adjuvant radiation therapy               | <i>In vivo</i> : Sub-q injection of RM-9 prostate cancer cells<br><i>In vitro</i> : Prostate cancer cell line (2D)                          | Huang <sup>105</sup>          |
| Immune cell infiltration modulation | High intensity ultrasound to replace neo-adjuvant radiation therapy               | <i>In vivo</i> : Ascitic carcinoma cells injected intraperitoneally (I.P.) and sub-q<br>No <i>in vitro</i> studies performed                | Chida <sup>46</sup>           |

## 1.6 Future directions

Despite undergoing intensive chemotherapy, surgery, and radiation therapy, up to 1 in 4 TNBC patients may experience local recurrence. Since ionizing radiation is known to upregulate hallmarks of cancer, such as angiogenesis and metastatic growth, radiotherapy may be associated with microenvironmental changes that promote recurrence in a small but significant subset of patients. However, many of the mechanisms governing this process are still unknown. Organoid models offer an avenue to elucidate these mechanisms. As mammary organoid cultures become more complex and translatable, researchers need to adopt standardized parameters to ensure that studies can be compared. It is important that reproducibility, scale, and biological relevance are considered.

Even with well-controlled media, scaffold, and seeding conditions, organoids can be heterogeneous in size, shape, and morphology. These parameters must be analyzed robustly and systematically in studies employing organoids as differences in morphology can have significant effects on viability profile, development, and other phenotypes<sup>15,44,268</sup>. Despite undertaking similar studies, different labs observe unique results<sup>28</sup>. To successfully navigate discrepancies in techniques, researchers will benefit from a baseline set of parameters and analytical techniques to adequately and reproducibly characterize organoid cultures.

Organoid cultures can generate 3D constructs much thicker than a cell monolayer, but organoid size is restricted by basic transport phenomena: too large, and the center will develop a hypoxic or necrotic core as oxygen is consumed faster than it can diffuse to the center. To address this, multiple groups are developing vascular networks within engineered tissues to provide a biologically relevant way to deliver oxygen and nutrients throughout the construct<sup>165,255</sup> or creating bioreactors to increase nutrient availability<sup>158,275</sup>. An additional hindrance to size is obtaining clear

images within large organoids. Indeed, one benefit of organoid models over *in vivo* studies is the relative ease of imaging. To overcome this challenge, optical clearing protocols have been developed to reduce light scattering and increase the imaging depth in organoids<sup>57,93,121</sup>. One recent study reported the development of a high throughput technique for improved fluorescent image resolution at depths of over 100  $\mu\text{m}$ , allowing for increased clarity deep into the organoid<sup>31</sup>.

Biological relevance, organoid maturation, and architecture are also important design considerations. Although the introduction of a third dimension is more accurate than monolayer cultures, researchers may declare physiological relevance without direct comparison to *in vivo* architectures. In the case of stem cell-derived organoids, for example, this can be inaccurate, as these tissues often resemble fetal rather than adult tissues<sup>199</sup>. This could result in a severe limitation in modeling various cancers as they disproportionately affect older populations. Recent studies have begun to make direct comparisons between organoid characteristics and *in vivo* tissue structure and function<sup>62,180,203</sup>.

Moving forward, tissue-derived organoids may be used to study additional effects of radiation therapy, including epigenetic changes caused by oxidative stress<sup>233</sup>. Organoid models will also benefit from looking beyond a single organ to model diseases with multi-organ pathologies<sup>199</sup>, potentially allowing for the characterization of systemic radiation effects. In the near future, organoids will serve an essential role in determining the mechanisms of tumor cell recruitment following therapy. Advances in this field will have significant positive implications for breast cancer patients vulnerable to recurrence.

## 1.7 Organization of Dissertation

This dissertation consists of 5 chapters.

**Chapter 2** details the development and characterization of a primary murine epithelial organoid model. This model was developed primarily to allow for co-culture of various compartments: normal tissue, immune cell, and tumor cell.

**Chapter 3** describes a organoid co-culture model that elucidates mechanisms of recurrence in an immunocompromised setting. It describes the development and lays the groundwork for reasoning why different proportions of various cells are utilized. Ultimately, it pairs *in vivo* and *in vitro* data to show that IL-6 secreted from myeloid-stromal interactions may serve as a chemoattractant toward circulating tumor cells.

**Chapter 4** details a static model of T cell infiltration. The role of CD8<sup>+</sup> T cells in the RT-wound healing process is explored *in vivo* and *in vitro*. Ultimately, it reveals that CD8<sup>+</sup> T cells may downregulate the secretion of cytokines associated with cellular stress and senescence; and in the absence of these lymphocytes, the wound healing response is aberrant, facilitating the enhanced recruitment of macrophages.

**Chapter 5** provides conclusions for the work discussed in this dissertation and discusses future areas of exploration that may be of interest.

## Chapter 2

### GROWTH AND CHARACTERIZATION OF IRRADIATED EPITHELIAL ORGANOIDs FROM MAMMARY FAT PAD TISSUE

*Adapted from:* Hacker BC, Gomez JD, Silvera-Batista CA, Rafat M. Growth and Characterization of Irradiated Organoids from Mammary Fat Pad Tissue. Journal of Visualized Experiments. 147:e59293, 2019.

#### 2.1 Summary

Organoids derived from the digested tissue are multicellular three-dimensional (3D) constructs that better recapitulate *in vivo* conditions than cell monolayers. Although they cannot completely model *in vivo* complexity, they retain some functionality of the original organ. In cancer models, organoids are commonly used to study tumor cell invasion. This protocol aims to develop and characterize organoids from the normal and irradiated mouse mammary gland tissue to evaluate radiation response in normal tissues. These organoids can be applied to future *in vitro* cancer studies to evaluate tumor cell interactions with irradiated organoids. Mammary glands were resected, irradiated to 20 Gy and digested in a collagenase VIII solution. Epithelial organoids were separated via centrifugal differentiation, and 3D organoids were developed in 96-well low-adhesion microplates. Organoids expressed the characteristic epithelial marker cytokeratin 14. Macrophage interaction with the organoids was observed in co-culture experiments. This model may be useful for studying tumor-stromal interactions, infiltration of immune cells, and macrophage polarization within an irradiated microenvironment.

## 2.2 Introduction

Approximately 60% of triple negative breast cancer (TNBC) patients choose breast-conserving therapy (BCT) as a form of treatment<sup>137</sup>. In this treatment modality, the tumor containing part of the breast tissue is removed, and the surrounding normal tissue is exposed to ionizing radiation to kill any residual tumor cells. Treatment reduces recurrence in much of the breast cancer population; however, approximately 13.5% of treated patients with TNBC experience locoregional recurrences<sup>146</sup>. Therefore, studying how radiation may recruit circulating tumor cells (CTCs) will lead to important insights into local recurrence<sup>122,249</sup>.

Previous work has shown that radiation of the normal tissue increases recruitment of various cell types<sup>193</sup>. In pre-clinical models of TNBC, irradiation of normal tissue increased macrophage and subsequently tumor cell recruitment to normal tissues<sup>193</sup>. Immune status influenced tumor cell recruitment to irradiated sites, with tumor cell migration observed in immunocompromised subjects. Recapitulating these interactions using organoids derived from mammary glands will allow the observation of cell migration and cell-stromal interactions in real time with microscopy and live cell imaging to determine the role of radiation damage in altering tumor cell behavior.

Mouse mammary organoids have helped elucidate key steps in the development of the mammary gland. A mammary organoid is a multicellular, three dimensional construct of isolated mammary epithelium that is larger than 50  $\mu\text{m}$ <sup>71,172,214,215,220</sup>. Using primary epithelial organoids, Simian et al. evaluated necessary factors for branching in the mammary gland<sup>220</sup>. Shamir et al. discovered that dissemination can occur without an epithelial to mesenchymal transition, providing insight

into the metastatic cascade<sup>214</sup>. Methods for generating and characterizing organoids from mammary gland tissue are well established<sup>65,69,173,215</sup>. However, to our knowledge, methods for growing irradiated organoids from mammary glands have not been reported. A protocol for growing and characterizing irradiated organoids would be a critical step in recapitulating radiation-induced immune and tumor cell recruitment.

In this paper, we report a method for growing and characterizing irradiated mammary epithelial organoids in low adhesion microplates coated with a hydrophilic polymer that supports the formation of organoids. These organoids were co-cultured with macrophages to examine immune cell infiltration kinetics. This work can be extended to include co-culturing organoids with adipose cells to recapitulate mammary characteristics, breast cancer cells to visualize tumor cell recruitment, and CD8<sup>+</sup> T cells to study tumor-immune cell interactions. Previously established protocols may be used to evaluate irradiated organoids. Earlier models co-culturing mammary organoids and immune cells have shed light on mechanisms of metastasis and dissemination. DeNardo et al. found that CD4<sup>+</sup> T cell regulation of tumor associated macrophages enhanced a metastatic phenotype of mammary adenocarcinomas<sup>61</sup>. Co-culture models have also been used to elucidate mechanisms of biological development. Plaks et al. clarified the role of CD4<sup>+</sup> T cells as down-regulators of mammary organogenesis<sup>187</sup>. However, our group is the first to establish a procedure of visualizing how normal tissue irradiation influences immune cell behavior. Because normal tissue irradiation has been shown to enhance tumor cell recruitment<sup>193</sup>, this protocol can be further developed to analyze how tumor cell behavior is altered by irradiation of normal tissue and cells, leading to a greater understanding of cancer recurrence.

## **2.3 Materials and Methods**

Animal studies were performed in accordance with institutional guidelines and protocols approved by the Vanderbilt University Institutional Animal Care and Use Committee.

### **Preparation of mice and cell acquisition**

#### **2.3.1. Mammary Gland Acquisition and Irradiation**

Nu/Nu mice (8-10 weeks old) were sacrificed using CO<sub>2</sub> asphyxiation followed by cervical dislocation. The skin was cleaned using 70% ethanol. Abdominal and inguinal mammary glands were resected from mice using pre-sterilized scissors and forceps. Lymph nodes were removed before resection. Mammary glands were rinsed in sterile 1x phosphate buffered saline (PBS). Mammary glands were then placed in 15 mL tubes with 10 mL Dulbecco's Modified Eagle Media/Nutrient Mixture F12 (DMEM/F12) for transport, on ice. Samples were then irradiated to a dose of 20 Gy using a cesium source.

#### **2.3.2. Mechanical Disruption and Digestion of Mammary Glands**

45 min after irradiating, mammary glands were placed in a 35 mm sterile cell plate and minced with scalpels. Mammary glands were minced approximately 40 strokes until the tissue relaxed and pieces were cut to a size no larger than approximately 1 mm<sup>2</sup> in area. Chopped tissue pieces were transferred to a collagenase solution in a 50 mL centrifuge tube. The collagenase solution consisted of 2 mg/mL collagenase, 2 mg/mL trypsin, 5% v/v fetal bovine serum (FBS), 5 µg/mL insulin, and 50 µg/mL gentamicin in DMEM/F12 media. For each mouse, 10 mL collagenase solution was

used. Samples were placed in a water bath at 37 °C and vortexed every 10 min for 30-60 min. Digestion was completed once the collagenase solution turned cloudy.

Samples were spun down at 450 x g for 10 min at room temperature. A pellet of epithelial cells, individual stromal cells, and red blood cells was recovered. From this step on, all pipettes, pipette tips, and centrifuge tubes were precoated with bovine serum albumin (BSA) solution prior to contact. BSA solution consisted of 2.5 w/v % BSA in Dulbecco's Phosphate Buffered Saline (DPBS). For pre-coating, BSA solution was simply added to and removed from the inside of the pipette tip and tubes.

For additional recovery, the supernatant was transferred to a fresh BSA coated 15 mL tube. The fat layer was dispersed by pipetting up and down vigorously and centrifuged at 450 x g for 10 min at room temperature. The supernatant was aspirated, leaving a small amount of media in the tube to avoid aspirating the cell pellet. The aqueous layer from the tube with original pellet was aspirated. 10 mL DMEM/F12 was then added to the tube with the original pellet and transferred to the second tube. The two pellets were resuspended by pipetting vigorously. This suspension was then centrifuged at 450 x g for 10 min at room temperature. The supernatant was aspirated and 4 mL DMEM/F12 was added to the tube.

40 µL deoxyribonuclease (DNase) was added to the suspension, which was gently shaken by hand for 2-5 min at room temperature. The DNase solution consisted of 4U/mL DNase in DMEM/F12. 6 mL DMEM/F12 was added, and the solution was thoroughly pipetted. The tube was centrifuged at 450 x g for 10 min at room temperature. The supernatant was aspirated to the 0.5 mL mark, and the pellet was resuspended in 10 mL DMEM/F12 and pipette thoroughly. The solution was pulsed to 450 x g and stopped 4 s after reaching that speed. Pulsing and resuspension

were repeated three more times to purify organoids via centrifugal differentiation. After this step, the pellet appeared to be an off-white color consisting of only epithelial organoids.

NOTE: Organoids can also be filtered using sterile mesh 40  $\mu\text{m}$  filters. After step 1.16, pipette media containing organoids through a filter into a centrifuge tube, and then rinse with 5 to 10 mL of DMEM/F12 media. Flip the filter over a new 50 mL centrifuge tube. Pass 10 mL of DMEM/F12 media through, going the opposite way to rinse off any retentate. The retentate should consist of organoids, and the filtrate should consist mainly of stromal cells, which can be discarded or kept if desired.

### 2.3.3 Determining Organoid Density

The pellet was resuspended in 10 mL DMEM/F12 and pipetted thoroughly to create a homogenous solution. 50  $\mu\text{L}$  of this solution was transferred to a 30 mm Petri dish and viewed under a phase contrast microscope at 20x. The number of organoids was quantitated with a tally counter.

Note: Here pipette tips have been consistently used with a minimal diameter of 457  $\mu\text{m}$ , which is 5-10 times the diameter of the organoids that are seeded. For transferring volumes of 2 mL or larger, use serological pipettes with tip diameters excess of 1500  $\mu\text{m}$ .

The organoid density was calculated using the following equation:

$$\frac{\# \text{ organoids in } 50\mu\text{L}}{50\mu\text{L}} = \frac{\# \text{ organoids in tube}}{\text{volume of tube}} [=] \frac{\text{organoids}}{\mu\text{L}}.$$

1000 organoids/mL was used as a desired density to simplify further dilution. If the density is too low, the cell solution was centrifuged at 450 x g for 5 min and resuspended, pipetting thoroughly to create a homogenous solution.

#### **2.3.4. Plating Organoids**

To grow organoids in a protein matrix, organoids were seeded at a concentration of 1 organoid/ $\mu$ L in collagen type 1 diluted to 87% or in basement membrane extracted from Engelbreth-Holm-Swarm mouse sarcoma. Samples were kept on ice to prevent premature gelation of basement membranes.

To grow organoids on low adhesion plates, 50  $\mu$ L of suspension (50 organoids) was carefully pipetted into each well of the low adhesion plate. 150  $\mu$ L of organoid media (1% penicillin-streptomycin and 1% insulin-transferrin-selenium (ITS) in DMEM/F12 media) was added to bring the total working volume to 200  $\mu$ L. Media was carefully changed every 2 days.

NOTE: Low adhesion plates are not tissue culture treated; therefore, the cells can be easily detached. Aspirate media slowly by tilting the plate and inserting the pipette tip at the edge of each well. Leave a small amount of media in the bottom of the well. Add new media slowly to avoid applying unnecessary shear forces to organoids.

#### **2.3.5 Co-culturing with Macrophages and 4T1s**

dTomato-labelled RAW 264.7 macrophages were maintained in DMEM media supplemented with 10% FBS and 1% penicillin-streptomycin. Macrophages were seeded at a density of  $1 \times 10^4$ ,  $5 \times 10^4$ ,

or  $1 \times 10^5$  cells/mL into wells with organoids. GFP labelled 4T1s were maintained in RPMI supplemented with 10% FBS and 1% penicillin-streptomycin. 4T1s were seeded at a density of  $1 \times 10^4$  cells/mL into wells with organoids. Live cell phase contrast and fluorescent imaging was used to monitor macrophage infiltration over time (**Figure 6A,B**).

### **2.3.6 Immunofluorescence Staining of Organoids**

Organoids can be stained in low adhesion wells or can be transferred to chamber slides. To transfer, gently pipette up and down until organoids have detached from plates. Transfer to chamber slides and incubate for 4-8 h to allow organoids to adhere to the plate surface.

Organoid medium was removed from the wells by carefully aspirating. Samples were fixed with 10% neutral buffered formalin for 15 min at room temperature. Samples were then washed 3x 5 minutes in 1x PBS.

Note: If desired, fixed samples can be stored at 4°C for one week for further staining.

Samples were then permeabilized with 0.1% 4-(1,1,3,3-Tetramethylbutyl)phenyl-polyethylene glycol for five minutes. To stain for F-actin, samples were incubated with phalloidin diluted 1:1000 and 1.67 nM bisbenzimidazole nuclear dye in 1% PBS/BSA for one hour at RT. For all other stains, samples were incubated in blocking solution with 5% normal goat serum in 0.1% PBS/Polyethylene glycol sorbitan monolaurate (PBST) for 1 hour at room temperature. Samples were then washed 3x 5 min with PBS.

Samples were incubated with Anti-Cytokeratin 14 diluted 1:1000, E-Cadherin diluted 1:200, or Tight Junction Protein One diluted 1:100 in 1% NGS in PBST for 1 hour at room temperature. After primary incubation, samples were washed 3x 5 minutes in PBST.

For secondary staining, samples were incubated with Goat Anti-Rabbit secondary diluted 1:200 with 1% NGS/PBST for 1 hour at room temperature in the dark. After secondary incubation, samples were washed 3x 5 min in PBS. Hoechst nuclear dye was used to stain nuclei. Samples were then washed 3x 5 min in PBS. If using chamber slide, samples were mounted with a coverslip. Stained samples were wrapped in foil and stored at 4°C for up to two weeks.

## 2.4 Results

Irradiated epithelial mammary organoids were successfully obtained from mouse mammary glands, processed, and cultured on low-adhesion plates (**Figure 2.1**).

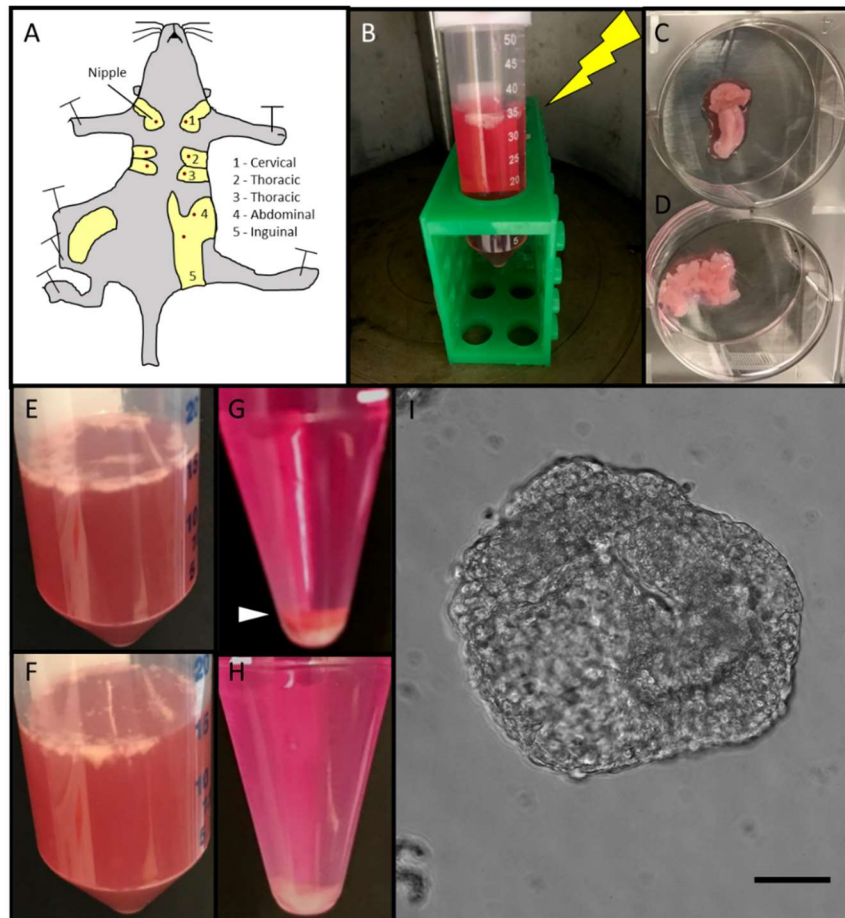


### Figure 2.1. Organoid Isolation Method Workflow.

**A.** Mammary glands were resected from mice. The abdominal and inguinal mammary glands were used. **B.** Mammary glands were irradiated in 50 mL centrifuge tubes containing DMEM/F12 media. **C.** Mammary glands were transferred to sterile six-well plates and cut with surgical scalpels until minced (**D**). **E.** Mammary glands were transferred into 50 mL centrifuge tubes containing 5 mL sterile DMEM/F12 media per gland and digested in a collagenase VIII solution (**F**). **G.** After being transferred to a 15 mL tube, centrifugal differentiation was utilized to remove stromal cells, single cells, and red blood cells, observed in a red pellet (white arrow-head) until only white epithelial organoids were obtained (**H**). **I.** 50 organoids were plated in 200  $\mu$ L of media in 96-well low adhesion plates and imaged using phase contrast microscopy. Scale bar represents 50  $\mu$ m.

Organoid yield was tested by seeding in different growth environments (**Figure 2.2A-G**). Seeding cells directly onto tissue culture treated 10 cm cell plates yielded an overgrowth of fibroblast cells. Fibroblasts were identified under phase contrast microscopy in or near the same plane of focus as organoids, and they quickly grew out from plated organoids within a few days. An outgrowth of fibroblasts was also observed when organoids were seeded in basement membrane and collagen protein matrices (**Figure 2.2E, F**).

A variety of conditions were tested in optimizing irradiated organoid growth (**Figure 2.2H**). Collagenase types I and VIII from *clostridium histolyticum* were used as the enzyme in the organoid digestion step<sup>69,156,157</sup>. Organoid yields were significantly higher after digestion with collagenase VIII. This may be due to the purification processes used in producing the enzyme: collagenase type I is partially purified and may cause unnecessary damage to membrane proteins and receptors, leading to poor organoid formation, cell lysis, or over-digestion<sup>27,156,157</sup>. No significant differences in yield between irradiated and control organoids were observed.

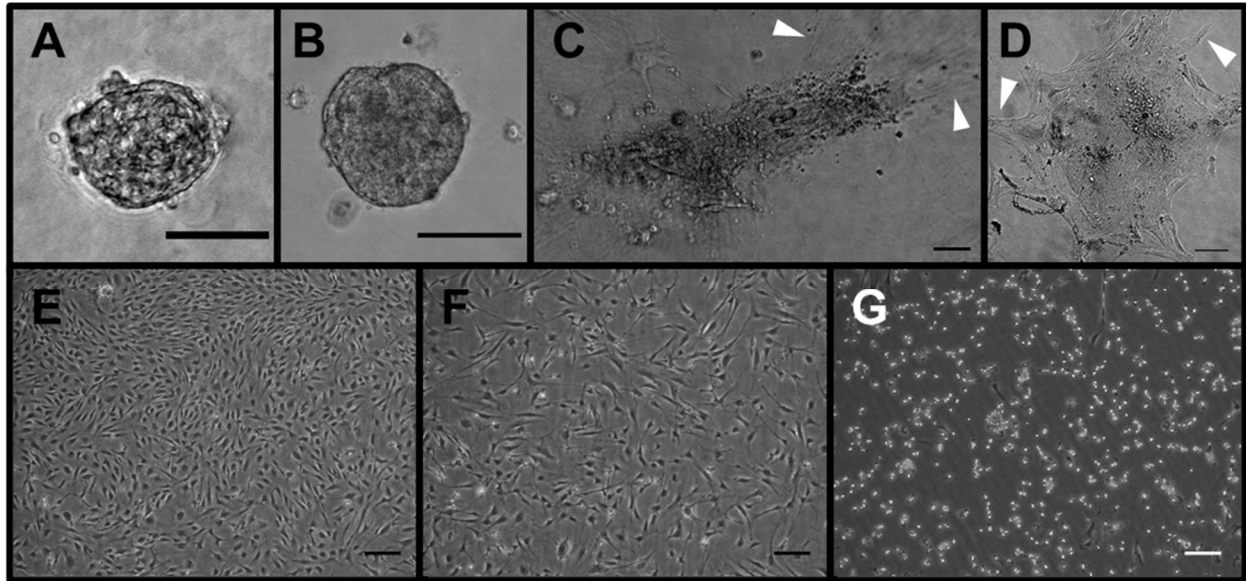


**Figure 2.2. Organoid Plating in 3D Protein Matrices and on Tissue Culture Treated Plastic.** Organoids seeded in collagen (A) and basement membrane (B), imaged after 84 hours of growth. Outgrowth of fibroblasts occurred in matrix plated organoids (C, D). Phase contrast images of organoids sorted through filtration were obtained 192 hours after seeding. No major differences between the filtrate (E) and retentate (F) were observed, with both resulting in confluent fibroblast growth. Cells in E and F were seeded on tissue culture treated plastic. After trypsinizing for five minutes at room temperature, fibroblasts were removed via aspiration; however, remaining epithelial cells formed a monolayer culture instead of three-dimensional organoids (G). Scale bars represent 100  $\mu\text{m}$ .

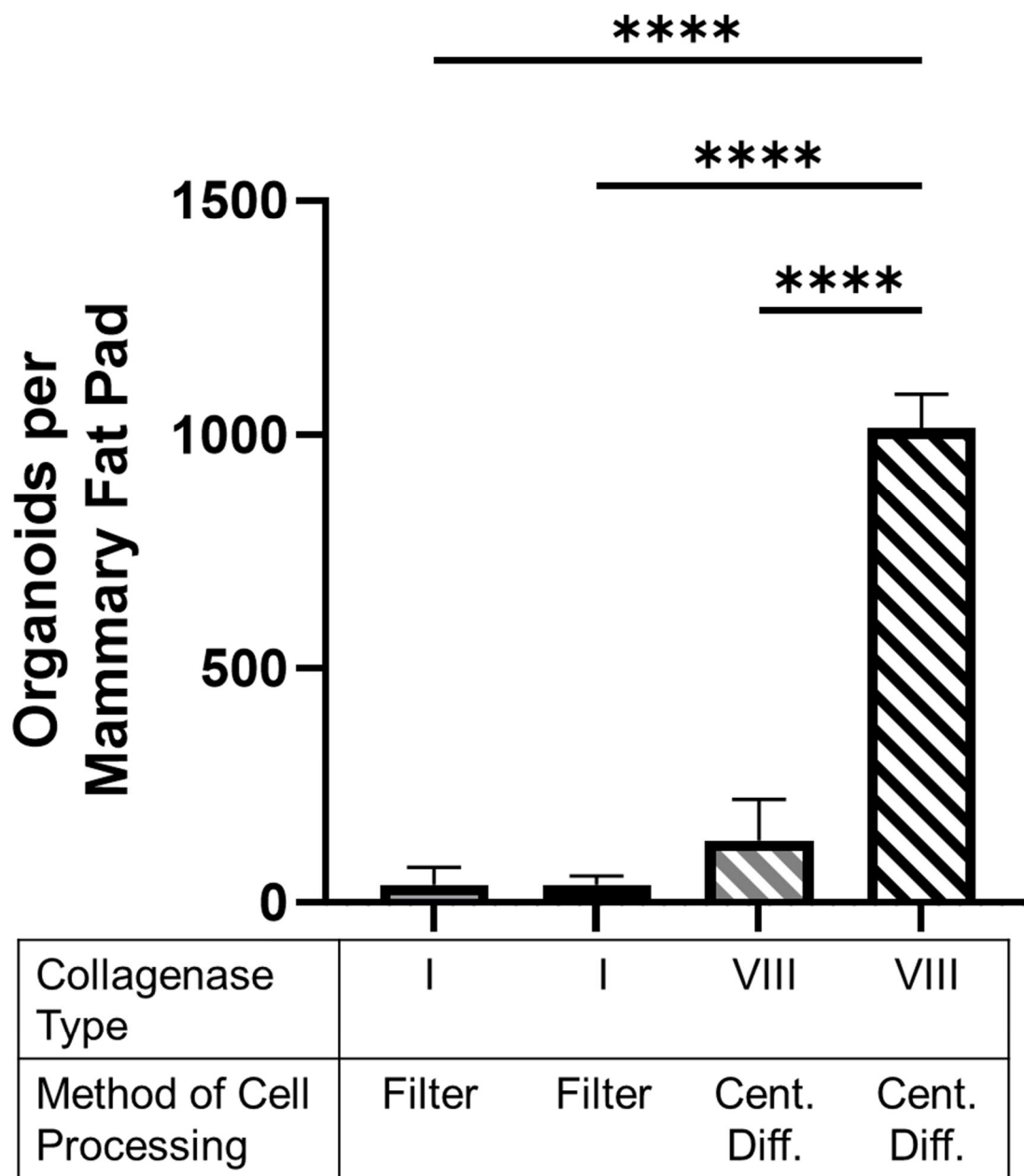


**Figure 2.3. Organoid Yields from Different Isolation Methods.**

Different collagenase types (I and VIII) and cell processing methods (filtration and centrifugal differentiation (Cent Diff)) were tested, and organoid yield per mammary gland was quantified (n = 3 glands for each method). Statistical significance was determined using one-way ANOVA, \*\*\*\*p<0.0001. Error bars represent standard error.

Irradiated organoids could be cultured in low adhesion plates (**Figure 2.3A-C**) or within basement membrane (**Figure 2.3D-G**), but the most rapid growth occurred in low adhesion plates (**Figure 2.3H**). Organoids recapitulated mammary gland characteristics. White arrowheads indicate constructs morphologically similar to ducts and lobes<sup>196,228,270</sup> (**Figure 2.3C**), which are critical for the production and transport of milk in the mammary gland<sup>196</sup>. However, further characterization is required to confirm this observation. Growth trends indicated that non-irradiated organoids grew faster than irradiated organoids (**Figure 2.3H**), most likely due to cell growth arrest resulting from mechanisms of DNA damage repair; however, the trend was not statistically significant<sup>153</sup>. Occasional clumping of low adhesion organoids was observed, and organoids could be cultured up to two weeks before dissociating.

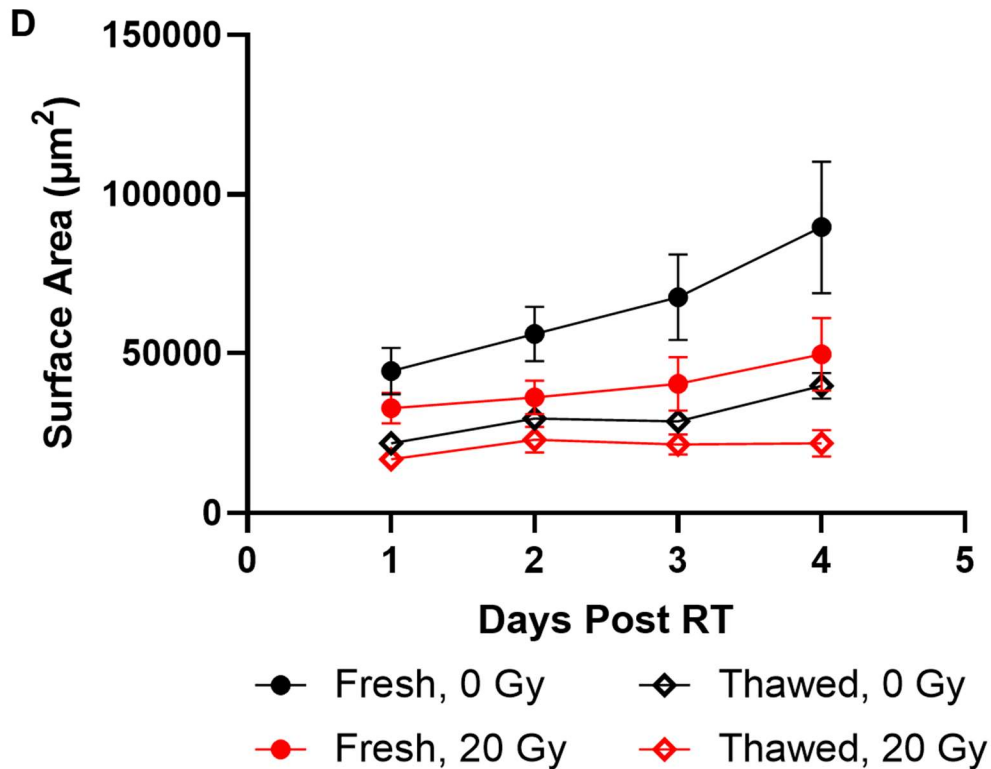
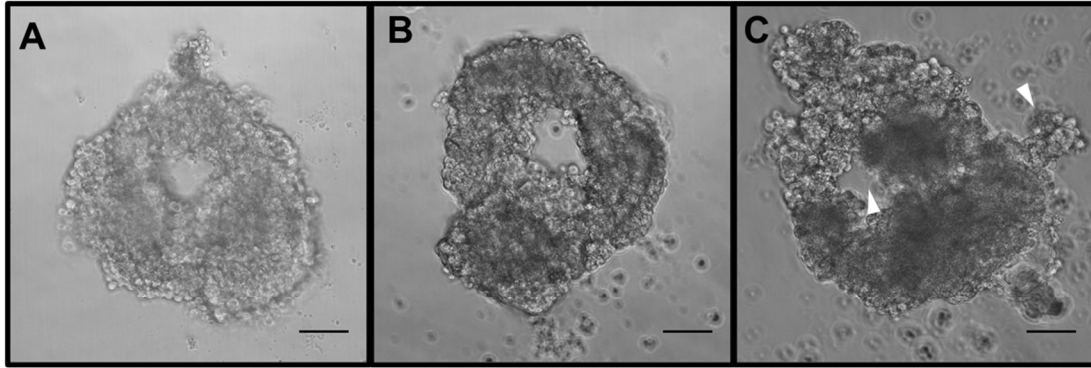


**Figure 2.4. Non-Adherent Organoid Growth.**

Representative phase contrast images of irradiated organoid growth in low adhesion plates obtained 24 (A), 48 (B), and 72 (C) hours after seeding. White arrowheads indicate structures that have similar morphology to ducts and lobes.. Scale bars represent 50 µm. **D.** Area measurements were obtained in different growth conditions: organoids immediately seeded after digestion and sorting (0 Gy, solid black circle; 20 Gy, solid red circle); and frozen organoids thawed and plated (0 Gy, open black diamond; 20 Gy, open red diamond). N=4 biological replicates, data is mean ± SEM. Area calculations were made using ImageJ software. No statistically significant differences were observed between the 0 and 20 Gy fresh organoids.

Organoids expressed epithelial characteristics, which were evaluated through immunofluorescence staining of Cytokeratin 14 (K14), E-Cadherin (E-cad), and Tight Junction Protein 1 (ZO-1)<sup>35,42,130</sup>(**Figure 2.4**). Irradiated organoids expressed epithelial markers. K14, a marker of myoepithelium<sup>130</sup>, was expressed strongly on the surface of irradiated organoids (**Figure 2.4A**). Additionally, E-cad and ZO-1 were expressed within cellular junctions of organoids (**Figure 2.4B, C**). These proteins are essential for proper cell adhesion<sup>35</sup>. After irradiation, organoids continued to retain their epithelial characteristics.

Fluorescent staining of organoids could be visualized within low adhesion plates using fluorescence microscopy (**Figure 2.5A-D**); however, the clearest visualization was obtained via confocal microscopy (**Figure 2.5E-F**). Corrected total fluorescence intensity was calculated by subtracting the background and normalizing by organoid area (**Figure 2.5G**).

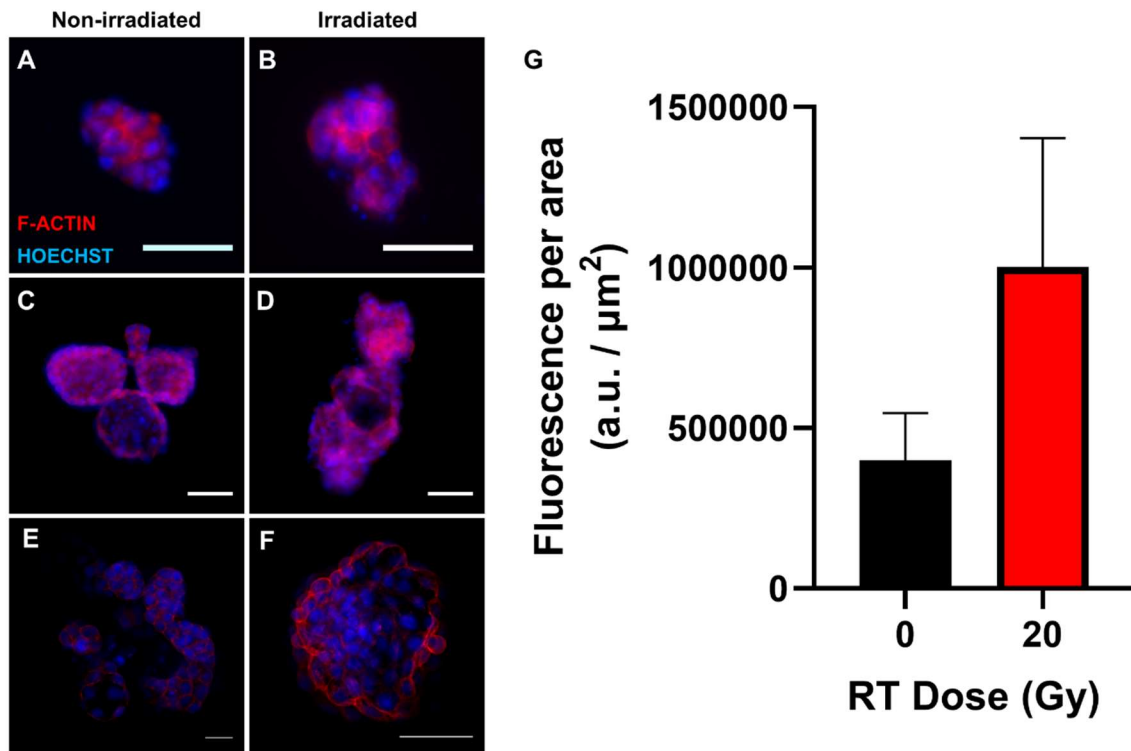


**Figure 2.5. F-actin expression in organoids.**

F-actin (red), a microfilament in epithelial cells, was expressed with lower intensity in non-irradiated organoids (A, C, E) than in irradiated (B, D, F) organoids. A nucleic acid stain was used to visualize nuclei (blue). Images were taken on low adhesion 96-well plates (A, B) and 16-well chamber slides (C, D). Images were also taken using confocal microscopy (E, F). All organoids were fixed and imaged after one week of growth. Scale bars are 50 μm. G. Phalloidin fluorescence data from low adhesion plate images were quantified in ImageJ (n = 3 glands). Error bars indicate standard error.

Growing organoids in the 96-well low adhesion plates also simplified co-culture experiments. When seeded at concentrations typical in the mammary gland, macrophages co-localization increased with irradiated organoids (Figure 2.6A, B)<sup>35,49</sup>. To mimic tumor infiltration into the irradiated microenvironment, organoids were included in a tri-culture with macrophages and GFP labelled 4T1 cells (Figure 2.6C). For all sizes of organoids, no differences in 4T1 co-localization



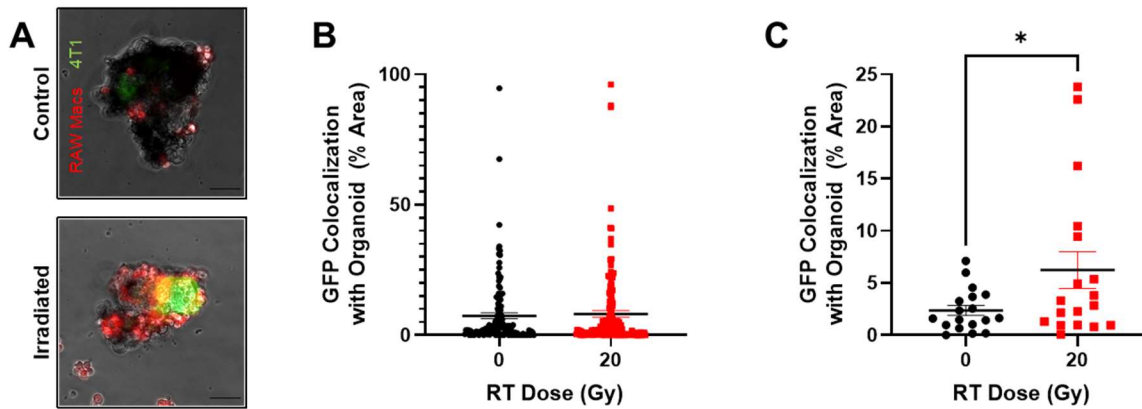


**Figure 2.7. Evaluating tumor-normal tissue interactions through co-culture.**

**A.** GFP labelled 4T1 cells co-localized with organoids alongside macrophage infiltration. **B.** 24 hours post seeding of 4T1 co-localization into organoids treated with 0 (black) and 20 (red) Gy irradiation. **C.** 4T1 co-localization into larger organoids ( $80,000 \mu\text{m}^2$  or above in size). Macrophages were seeded at concentrations of 50,000 cells/mL, and 4T1s were seeded at a density of 10,000 cells/mL, and their infiltration was captured every 30 minutes via live cell fluorescence imaging. All co-culture experiments commenced 7 days after initial organoid seeding. Data is mean  $\pm$  SEM. Statistical significance was determined using a two-tailed, unpaired t-test, \* $p < 0.05$ , \*\* $p < 0.01$ .

## 2.5 Conclusions and Future Work

In this protocol, we have developed a method for reproducible growth and characterization of irradiated mammary organoids (**Figure 2.1**). An irradiation dose of 20 Gy was applied to mirror previous *in vivo* models of tumor cell recruitment<sup>193</sup>. Irradiation of mammary glands *ex vivo* prior to organoid formation allowed for isolation of radiation damage effects without a corresponding infiltration of immune cells. The development of an *in vitro* irradiated normal tissue model enables real time viewing of cellular interactions that may contribute to radiation induced CTC recruitment<sup>69,173</sup>.

Closely following steps 1.5-1.18 was critical for maximizing organoid yield. We added thawed aliquots of concentrated collagenase to the digestive solution. Due to the highly viscous nature of the concentrated collagenase aliquot, there can be some variations in amount and therefore in enzymatic activity, so organoid digestion must be closely monitored to avoid over-digestion. It is also important to digest organoids in a 50 mL tube as this allows for an even surface area for digestion. Other studies have used filtration for purifying organoids<sup>130,270</sup>; however, we obtained a much higher yield purifying with centrifugal differentiation (**Figure 2.2H**). Pre-coating pipettes, pipette tips, and centrifuge tubes with the BSA solution is essential for maximizing yield. Organoids noticeably adhere to uncoated plastic when solution application is neglected.

Great care must be taken to avoid aspirating organoids. This is a risk that occurs when purifying, changing media, and staining for fluorescent markers. Using low adhesion plates for growth allows for easy transfer of organoids and removes the need for organoids to be sectioned in OCT for further staining, a procedure required for basement membrane embedded organoids<sup>173</sup>. In addition to benefits from superior growth, seeding irradiated organoids in low adhesion plates required fewer steps and was less technically challenging than culturing organoids in basement

membrane or collagen. However, when staining for markers, it may be helpful to view organoids under a microscope to ensure that accidental aspiration does not occur.

Moreover, there are many considerations that must be accounted for when imaging organoids. Within basement membrane embedded organoids, occasional fibroblast growth may be observed (**Figure 2.2C, D**). Fibroblast outgrowth in 3D cultured organoids may be caused by organoids making contact with the tissue culture treated surface as adhesion leads to upregulated fibroblast growth factor production in adherent cells<sup>109</sup>. Interestingly, the morphology of these fibroblasts is strikingly similar to pre-adipocytes as both cell types exhibit spindly, elongated shapes<sup>86</sup>. In further investigation, exposure to insulin, dexamethasone, and 3-isobutyl-1-methylxanthine (IBMX) may yield cells with an adipogenic lineage, spurring a shift toward a more spherical cellular shape associated with adipocytes<sup>86,210</sup>. We obtained clear images using phase contrast microscopy of free-growing low adhesion (**Figure 2.3A-C**) and basement membrane embedded (**Figure 2.3D-G**) organoids. Tracking individual organoid growth in low adhesion plates, however, was difficult due to minimal focal adhesions between the cells and well surface, resulting in organoid movement and occasional aspiration.

Once stained for surface markers, confocal microscopy rendered clearer marker localization (**Figure 2.5E, F**) than widefield microscopy (**Figure 2.5A-D**). From fluorescence quantification, trends in phalloidin expression suggest that irradiated organoids expressed increased F-actin relative to the control (**Figure 2.5G**). Actin cytoskeleton reorganization has been observed in dermal microvascular endothelial cells irradiated at similar dosages<sup>79</sup>.

For extended imaging sequences, like time lapse co-culture with immune cells (**Figure 2.6**), a live cell imaging chamber with humidity and CO<sub>2</sub> control is required<sup>70</sup>. Live cell images taken every 30 minutes revealed that macrophages co-localized with organoids after 24 hours

(**Figure 2.6A, B**), preferentially migrating toward irradiated organoids (**Figure 2.6C**). Macrophage infiltration into irradiated normal tissue has been observed *in vivo*, is attributed to chemokine and cytokine gradients, and typically precedes CTC recruitment<sup>193</sup>. Future studies will evaluate classically and alternatively activated macrophage interactions with organoids as polarized macrophage dynamics may play an important role in determining response to radiation<sup>149,271</sup>. Additional analyses will evaluate the consequence of serum starvation and the growth effects of culturing organoids in complete media since these variables may have significant effects on organoid-immune cell interactions. This system can further be adapted for co-culture with other cell types, including CD8<sup>+</sup> T cells, stromal cells, adipocytes, and breast cancer cells. Real time observation with techniques like live cell imaging will facilitate the elucidation of potential mechanisms that contribute to CTC recruitment to irradiated normal tissue, which may have significant implications for patients suffering from recurrent TNBC.

## Chapter 3

### IRRADIATED MAMMARY FIBROBLAST ORGANIDS ELUCIDATE MECHANISMS OF MACROPHAGE-MEDIATED BREAST CANCER RECURRENCE

*Adapted from:* Hacker BC, Lin EJ, Herman DC, Questell AM, Martello SE, Hedges RJ, Walker AJ, Rafat M. Irradiated Mammary Spheroids Elucidate Mechanisms of Macrophage-Mediated Breast Cancer Recurrence. *Cellular and Molecular Bioengineering*, In Revision.

#### 3.1 Summary

While most patients with triple negative breast cancer receive radiation therapy to improve outcomes, a significant subset of patients continue to experience recurrence. Macrophage infiltration into radiation-damaged sites has been shown to promote breast cancer recurrence in pre-clinical models. However, the mechanisms that drive recurrence are unknown. Here, we developed a novel organoid model to evaluate macrophage-mediated tumor cell recruitment.

We characterized infiltrating macrophage phenotypes into irradiated mouse mammary tissue via flow cytometry. We then engineered a organoid model of radiation damage with primary fibroblasts, macrophages, and 4T1 mouse mammary carcinoma cells using *in vivo* macrophage infiltration results to inform our model. We analyzed 4T1 infiltration into organoids when co-cultured with biologically relevant ratios of pro-healing M2:pro-inflammatory M1 macrophages. Finally, we quantified interleukin 6 (IL-6) secretion associated with conditions favorable to tumor

cell infiltration, and we directly evaluated the impact of IL-6 on tumor cell invasiveness *in vitro* and *in vivo*.

In our *in vivo* model, we observed a significant increase in M2 macrophages in mouse mammary glands 10 days post-irradiation. We determined that tumor cell motility toward irradiated organoids was enhanced in the presence of a 2:1 ratio of M2:M1 macrophages. We also measured a significant increase in IL-6 secretion after irradiation both *in vivo* and in our model. This secretion increased tumor cell invasiveness, and tumor cell invasion and recruitment were mitigated by neutralizing IL-6.

Our work suggests that interactions between infiltrating macrophages and damaged stromal cells facilitate breast cancer recurrence through IL-6 signaling.

### **3.2 Introduction**

Almost 300,000 American women will be diagnosed with breast cancer in 2022<sup>218</sup>, and approximately 15% of those patients will have triple negative breast cancer (TNBC), a particularly aggressive subtype. To treat this disease, patients elect to undergo chemotherapy, surgery, and radiation therapy (RT)<sup>2</sup>. RT typically produces positive outcomes for a majority of patients<sup>64,146</sup>. However, an emerging body of literature implicates RT in contributing to cancer recurrence. Up to 20% of patients will experience locoregional recurrence after RT, and this may be correlated to patient immune status<sup>2,3,193,217</sup>. Lymphopenia, or low lymphocyte count, has been identified as a risk factor for worse clinical outcomes in breast cancer patients<sup>53</sup>. Chemotherapy and RT can cause lymphopenia and immune dysfunction<sup>129</sup>, and lymphopenia is correlated with lower overall survival after therapy<sup>4</sup>. This suggests that a significant number of TNBC patients may benefit from additions to their therapeutic regime.

The impact of normal tissue radiation damage on cancer recurrence is currently understudied. Previous pre-clinical studies have linked radiation to tumor spread. For example, irradiation of mammary stroma induced breast cancer in injected epithelial cells<sup>20</sup>. However, radiation damage alone does not dictate recurrence. Radiation-induced metastasis of TNBC cells to the lung was shown to be facilitated by macrophages<sup>276</sup>. Pre-irradiation of tumor beds led to myeloid cell infiltration and then tumor cell growth due to matrix degradation<sup>6</sup>. More recently, macrophages were shown to promote tumor cell recruitment following normal tissue radiation damage under lymphopenic conditions<sup>193</sup>. However, the contribution of stromal-macrophage interactions to breast cancer recurrence following normal tissue radiation remains unknown.

Organoid models provide an avenue to determine mechanisms of recurrence,<sup>92</sup> and their increased biological relevance compared to monolayer studies allows for insights into cell movement, direct cell-cell interactions, and cell-extracellular matrix (ECM) interactions<sup>14,91,253</sup>. Organoid models complement *in vivo* models, and they serve as a crucial tool to design well-controlled and robust studies. Here, we developed a novel primary fibroblast organoid model to evaluate the effect of radiation damage on stromal-macrophage interactions that drive recurrence. We first characterized *in vivo* macrophage infiltration to inform our model parameters. We then used our organoid model to determine the contributions of irradiated normal tissue and macrophage infiltration to TNBC recurrence.

### **3.3 Materials and Methods**

#### **3.3.1 Cell Lines**

Luciferase-labeled and GFP expressing 4T1 mouse mammary carcinoma cells were obtained from Dr. Laura L. Bronsart (Stanford University). All cells were cultured at 37°C and 5% CO<sub>2</sub>. 4T1 cells were cultured in RPMI-1640 (Gibco) supplemented with 10% heat-inactivated fetal bovine serum and antibiotics (100 U/mL penicillin and 100 mg/mL streptomycin). Cells were used within three passages before injection into mice.

#### **3.3.2 Orthotopic Tumor Studies**

Animal studies were performed in accordance with institutional guidelines and animal protocols approved by the Vanderbilt University Institutional Animal Care and Use Committee. Tumor inoculation was performed by injecting  $5 \times 10^4$  4T1 cells in a volume of 50  $\mu$ L of sterile PBS into the number four inguinal right MFPs of 8- to 10-week old female Nu/Nu or Balb/C mice (Charles River Laboratories). In CD8<sup>+</sup> T cell reduction experiments, 0.5 mg anti-CD8a (2.43; BioXCell) was injected intraperitoneally every 5 days starting from the day of inoculation<sup>193</sup>. Control mice were injected with 0.5 mg rat IgG2b isotype control (LTF-2; BioXCell) using the same dosing schedule. In IL-6 depletion experiments, 0.5 mg anti-IL6 (BioXCell) was injected intraperitoneally starting 6 hours before irradiation, then every 3 days afterward. Control mice were injected with 0.5 mg IgG1 isotype control antibody (BioXCell). Tumor length and width were measured using digital calipers (Fisher Scientific) beginning one week after tumor inoculation. Tumor volume was calculated as follows:  $\text{Volume} = (L_1^2 \times L_2)/2$ , where  $L_1$  is the smaller diameter of the tumor, and  $L_2$  is the larger diameter<sup>193</sup>.

### 3.3.3 Luminex Multiplex Cytokine Assay

To assess cytokine profiles at the local site of infiltration, MFPs were harvested and homogenized in 20 mM Tris HCl (pH 7.5) buffer with 0.5% Tween 20, 150 mM NaCl, and protease inhibitor, centrifuged for 10 min at 4°C, and supernatant was stored at -80°C<sup>23</sup>. Protein content was measured using bicinchoninic acid protein assay (ThermoFisher). For evaluation of systemic cytokine signaling, blood samples were collected via retro-orbital bleed, allowed to clot at room temperature for 30 minutes, then centrifuged for 10 minutes. Serum was then recovered and stored at -80°C. Samples were processed at the Stanford Human Immune Monitoring Center using a mouse 39-plex Affymetrix kit. A list of cytokine definitions can be found in **table A.2**.

### 3.3.4 Primary Organoid Generation

Organoid were generated from primary cells obtained from the SVF in mouse MFPs using previously published techniques<sup>235</sup>. Briefly, MFPs were harvested and minced with a blade and digested for 40 minutes in a solution of PBS with 20 ug/mL liberase, and antibiotics (100 U/mL penicillin and 100 mg/mL streptomycin). Tissue was flushed through a 100 µm filter and plated in 10 cm dishes in DMEM/20% BCS. Upon confluence, cells were plated in low adhesion U-bottom plates at a density of 10,000 cells/organoid. Organoids were formed within 24 hours of passaging.

### 3.3.5 Radiation

Radiation was delivered by two methods. For *in vivo* RT, mice were anesthetized by administering isoflurane and irradiated to 20 Gy using a 300 kVp cabinet x-ray system filtered with 0.5 mm Cu. The mice were shielded using a Cerrobend jig with apertures 1 cm wide and 1.5 cm long to expose normal MFPs. Transmission through the 2 cm thick shield was less than 1%. For *in vitro*

experiments, organoids were irradiated in U-bottom low adhesion plates to 20 Gy using a Cesium source.

### **3.3.6 Flow Cytometry**

MFPs were harvested and minced in a solution of 1% FBS in PBS. They were then placed in a 2 mg/mL solution of Collagenase II (Sigma) and incubated for 30 minutes in a water bath at 37°C. The digestion was inactivated by adding 1% FBS in PBS. The digested tissue was then passed through a 100 µm filter to generate a single cell suspension. Cells were stained with the Aqua fixable viability stain (ThermoFisher) and FC receptors were blocked with CD16/32 (Biolegend) simultaneously with other cell surface markers for 20 minutes at 4°C. After staining, cells were rinsed with PBS and fixed with 1% neutral buffered formalin in saline for at least 20 minutes at 4°C. Intracellular stains were performed using an intracellular permeabilization buffer (ThermoFisher). Fixed cells were rinsed with PBS for 5 mins, rinsed with permeabilization buffer for five minutes, then incubated with antibodies diluted in permeabilization buffer for thirty minutes at room temperature in the dark. Cells were then rinsed with permeabilization buffer and resuspended in PBS. Flow cytometry was performed on a four-laser Amnis CellStream machine (Luminex), and FlowJo software was used for analysis. Compensations were obtained by using compensation beads (ThermoFisher). The following antibody clones were used for analysis: CD45 (30-F11), CD11b (M1/70), F4/80 (BM8), MHCII (M5/114.15.2), iNOS (CXNFT), CD64 (X54-5/7.1), CD86 (GL1), CD206 (C068C2), IL-4R $\alpha$  (I015F8), IL-10 (JES5-16E3), and Arg-1 (A1exF5).

For staining of primary SVF cells, cells were passaged and stained using the same staining protocol. The following antibody clones were used for analysis: PDGFR $\alpha$  (APA5), PDGFR $\beta$  (APB5), Podoplanin (8.1.1), CD26 (H194-112), and CD90.2/Thy1.2 (53-2.1).

### **3.3.7 Organoid Embedding, Sectioning, and Immunofluorescence**

Organoids were stained using previously published methods<sup>9,102</sup>. Tissues were carefully transferred to microcentrifuge tubes using wide bore pipet tips. Organoids were rinsed in PBS and fixed in 10% Neutral Buffered Formalin overnight at 4°C. They were then rinsed in PBS and incubated in 30% sucrose overnight at 4°C. They were subsequently incubated 2-4 hours in 1:1 mixture of 30% sucrose-PBS and OCT, transferred to a mold with OCT, and stored at -80°C before cryosectioning. For immunofluorescence, slides were incubated in PBS to remove OCT and permeabilized with 0.1% Triton-X 100 in PBS for 10 minutes. Sections (15  $\mu$ m) were then rinsed with PBS and blocked with 1% bovine serum albumin (BSA) in PBS with 10% normal goat serum (NGS) for 1 hour at room temperature in humid chambers. Sections were incubated with primary antibody diluted in 1% BSA in PBS overnight in humid chambers at 4°C. After rinsing with PBS, sections were incubated with secondary antibody diluted in 1% BSA in PBS for 2 hours in humid chambers. Then, after additional PBS rinses, sections were incubated with phalloidin (ThermoFisher) for 1 hour. Coverslips were mounted onto slides using NucBlue mounting media (ThermoFisher) and allowed to cure overnight before imaging on a fluorescence microscope (Leica DMI8). Antibodies and stains used for immunofluorescence studies include iNOS (Abcam), CD206 (Abcam), collagen IV (Abcam), MMP 9 (Abcam), F4/80 (Invitrogen) and phalloidin (ThermoFisher).

For whole mount staining, organoids were transferred to PBS after fixation. They were blocked and permeabilized in buffer containing 1% BSA, 1% DMSO, 1% Triton-X 100, and 1% NGS for 1 hour at room temperature on an orbital shaker. After blocking, they were incubated with primary antibodies for 72 hours at 4°C. After primary antibody incubation, organoids were rinsed 5 times, then incubated with secondary antibodies (1:200), Hoechst (2 µM), and phalloidin (Thermofisher) for 24 hours at 4°C. After secondary incubation, organoids were rinsed 5 times and imaged. Fiji was used to for image analysis.

### **3.3.8 Scanning Electron Microscopy (SEM)**

Organoids were fixed using methods previously published<sup>204</sup>. Briefly, organoids were carefully transferred from culture plates into a microcentrifuge tube using a wide bore pipet. Organoids were washed in 1x PBS and then fixed in 2% glutaraldehyde, 4% paraformaldehyde, and 0.1 M sodium cacodylate buffer (pH 7.3) for 1 hour at 4°C followed by incubation in 1% glutaraldehyde in PBS for 15 min at room temperature. After fixation, organoids were washed 3x in PBS then dehydrated in a series of 10 minute incubations of 10%, 25%, 50%, 75%, 90%, and 2x 100% ethanol at room temperature. The organoids were then further dehydrated in 50% ethanol:hexamethyldisilazane (HMDS) and 100% HMDS, and air dried overnight. They were mounted on carbon backed aluminum stubs, sputter coated with gold for 45 seconds (Cressington), and imaged using a Quanta 250 Environmental Scanning Electron Microscopy at 5 kV.

### **3.3.9 Primary Macrophage Isolation and Culture**

Bone marrow derived macrophages (BMDMs) were cultured using previously published methods<sup>77,266,273</sup>. Briefly, macrophages were isolated from the femurs of Nu/Nu mice. Femurs were

crushed using a mortar and pestle, and the cell suspension was passed through a 40  $\mu\text{m}$  filter. Red blood cells were lysed with an ACK lysis buffer, and macrophage precursors were plated at densities of  $1 \times 10^6$  cells/plate in IMDM supplemented with 10% FBS, antibiotics (100 U/mL penicillin and 100 mg/mL streptomycin), and 10 ng/mL macrophage colony stimulating factor (MCSF) on 10 cm low adhesion plates for 7 days for maturation into macrophages. For polarization, media was spiked with LPS and IFN- $\gamma$  for 24 hours (M1 macrophages) or IL-4 for 48 hours (M2 macrophages).

### **3.3.10 Invasion Assay**

Conditioned media (CM) collected from organoid and macrophage co-cultures was used as chemoattractants in a transwell migration assay (Corning reduced growth factor Matrigel invasion chamber, 8  $\mu\text{m}$  pore size). Organoids were irradiated to 20 Gy and then co-cultured with 2:1 M2:M1 macrophages. Supernatant was collected after 24 hours of co-culture. 100,000 4T1 cells were seeded into the upper chambers and incubated with CM for 24 hours. Cells that invaded through Matrigel inserts or migrated through uncoated inserts were stained with NucBlue mounting media and nuclei were counted. Invasion was calculated by dividing invasion counts by migration counts.

### **3.3.11 Organoid 4T1 Migration Assay**

24 hours after irradiation of organoids, 100 GFP-labeled 4T1 cells were plated per organoid. Infiltration was monitored via live cell fluorescence and phase contrast imaging every 24 hours for a total of 72 hours after plating of 4T1 cells. GFP signal was evaluated as a function of radial position via a custom MATLAB (MathWorks) script. Along the radial axis, 1,000 readings of

fluorescent intensity were evaluated over every angle of each organoid. Readings were normalized to the overall length of each radius to generate relative intensity values. For each biological replicate, more than 10 technical replicates were analyzed.

### **3.3.12 IL-6 Quantification**

IL-6 secretion in CM was measured using an ELISA assay (R&D systems) per manufacturer instructions.

### **3.3.13 Statistical Analysis**

To determine statistical significance, differences in radiation dose on flow cytometry data and cytokine concentration were analyzed using two-tailed unpaired t-tests. One-Way ANOVA was evaluated when comparing co-culture conditions for GFP intensity, IL-6 secretion, and 4T1 invasiveness. All statistical analysis was performed in GraphPad Prism 9.

### 3.4 Results and Discussion

#### 3.4.1 In vivo characterization of infiltrating macrophages and cytokine secretion resulting from radiation damage

We characterized the phenotypes of macrophages that infiltrated irradiated mouse mammary fat pads (MFPs) in a model of radiation-induced recurrence (**Figure 3.1**)<sup>193</sup>.

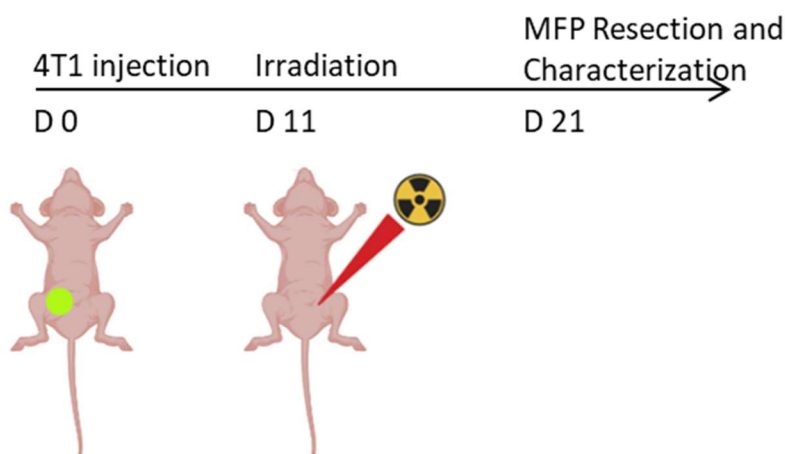


**Figure 3.1: Schematic of *in vivo* experiments.**

We defined macrophage ( $CD45^+CD11b^+F4/80^+$ ) phenotypes as follows: as cells expressing high expression of iNOS, CD86, CD64, or MHCII for pro-inflammatory M1 macrophages and IL4R $\alpha$ , Arg-1, CD206, or IL-10 for pro-healing M2 macrophages<sup>150,229,267</sup>. We observed no increase in M1 macrophage infiltration 10 days post-RT (**Figure 3.2 A, A.3.1 C**). However, a significant increase in M2 macrophage infiltration was observed with tumor cell recruitment (**Figures 3.2 B, A.3.1 D**). In TNBC patients, higher numbers of tumor associated macrophages typically with an M2 phenotype are correlated with poorer prognosis<sup>232</sup>. Expression of CD163, an M2 marker, in breast tumors was linked to increased likelihood of early distant recurrence and decreased overall survival<sup>213</sup>. Additionally, it has been shown that M2 macrophages play a role in

radiation-induced recurrence in other cancers. For example, expression of CD163 in primary head and neck cancer tumors is associated with a higher likelihood of recurrence after RT<sup>17</sup>.

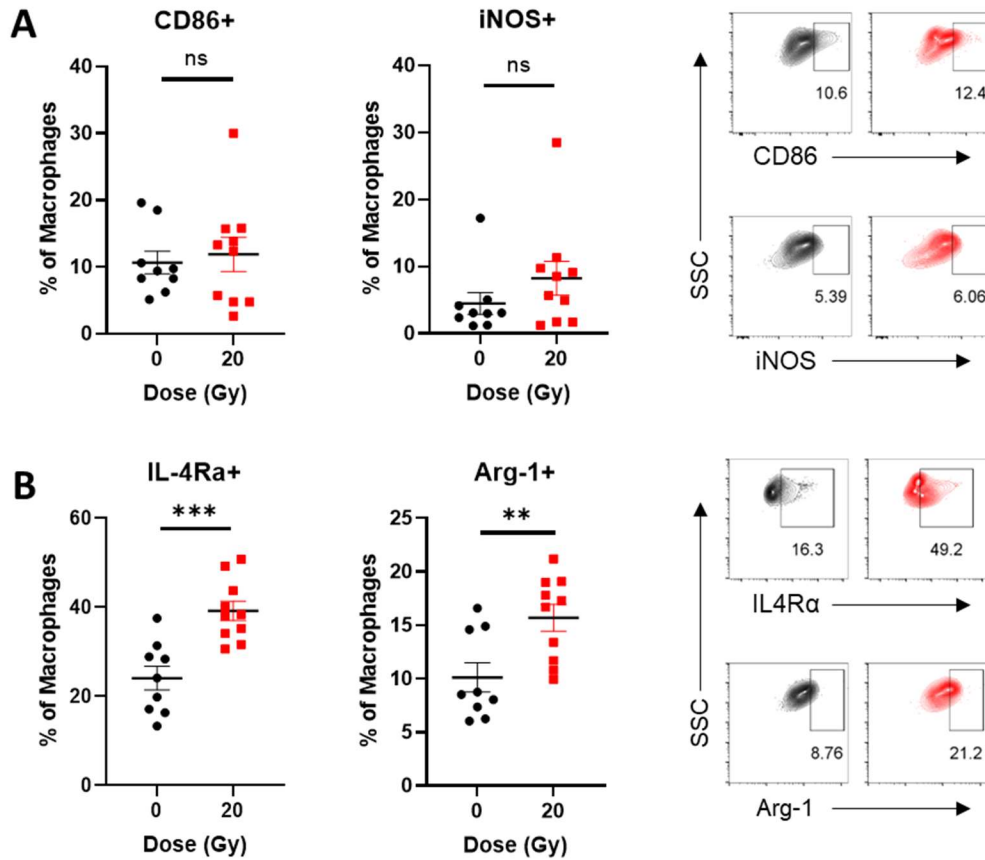


**Figure 3.2. M2 Macrophage infiltration is increased after in vivo irradiation.**

Flow cytometry characterization of M1 (A) and M2 (B) macrophage infiltration into MFPs 10 days post-RT (n=9-10 biological replicates). Error bars show standard error of the mean with \*\*p<0.01 and \*\*\*p<0.001 as determined by a two-tailed unpaired t-test.

Because communication between damaged tissue and immune cells is essential to the wound healing response, we evaluated how local and systemic cytokine expression influenced tumor cell recruitment in Balb/C mice with antibody-reduced CD8+ T cells to model lymphopenic patients. Cytokine secretion 10 days post-RT from MFP homogenates and mouse serum was evaluated using a Luminex multiplex immunoassay. Median fluorescence intensity (MFI) values

were normalized to those obtained from mice without tumor cell infiltration or RT. MFPs with tumor cell infiltration post-RT exhibited greater than a 2-fold increase in interleukin 6 (IL-6) and IL-23, and more than a 3-fold increase in transforming growth factor beta (TGF- $\beta$ ) relative to a mouse without tumor cell infiltration (**Figure 3.3 A**). Additionally, increases in IL-6 expression were observed systemically (**Figure 3.3 B**). Increased levels of IL-6 in serum are associated with higher risk of early recurrence and bone metastasis<sup>176</sup>. Although IL-6 is typically known as a pro-inflammatory cytokine<sup>119</sup>, it has also been shown to promote TNBC epithelial-mesenchymal transition, progression, cancer stemness, and M2 macrophage polarization<sup>259</sup>. The role of M2 secreted IL-6 as a response to neuroinflammation may be similar to the response of M2 macrophages of a radiation-damaged normal tissue microenvironment<sup>39</sup>. Together, these data indicate that IL-6 influences the recruitment of circulating tumor cells *in vivo*.

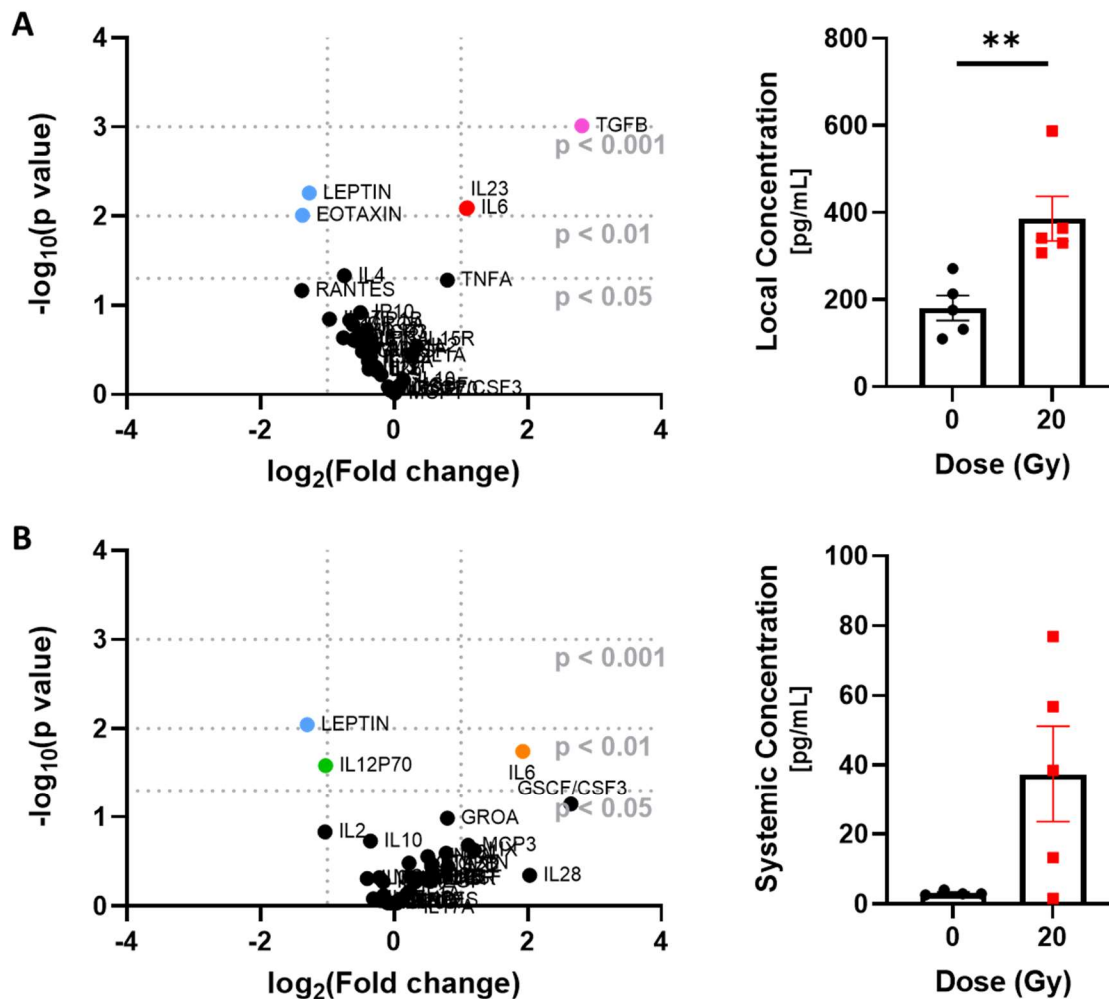


**Figure 3.3: IL-6 secretion is associated with in vivo RT of normal mammary tissue.**

**A.** Volcano plot of relative change in cytokines in irradiated MFPs. Differences were calculated by normalizing cytokine median fluorescence intensity values 10 days post-RT to values from non-irradiated CD8+ T cell-reduced mice with no tumor. **B.** Volcano plot of relative change in cytokines in serum samples. Error bars show standard error of the mean with \*\* $p < 0.01$  as determined by a two-tailed unpaired t-test.

### 3.4.2 Primary fibroblast organoid model

The stroma in the mammary gland is made up of a heterogeneous collection of fibroblasts. We evaluated the contributions of cells derived from the mammary stromal vascular fraction (SVF) to

tumor cell recruitment. Within 16 hours of plating in U-bottom low-adhesion plates, cells formed organoids of approximately 300  $\mu\text{m}$  in diameter (**Figure 3.4 A**), a size that is below the threshold where hypoxia and necrosis may occur<sup>56,92</sup>. Surface markers of primary SVF cells were evaluated. The isolated cells expressed high and consistent levels of platelet-derived growth factor receptor beta (PDGFR $\beta$ ), Podoplanin, and CD90.2/Thy1.2 (**Figures 3.4 B, A.3.3 A**). Expression of these markers have been shown in both healthy mammary glands and in mammary glands containing cancer associated fibroblasts<sup>211,247</sup>. There was negligible expression of immune, epithelial, and endothelial markers (**Figures 3.4.C, A.3.4 B**), implying that this model is composed primarily of fibroblasts. Fibroblasts produce ECM components, and radiation induces fibrosis, which results in excess ECM production<sup>58,151</sup>. Previous studies have incorporated primary fibroblasts into organoids<sup>235</sup>; however, we are the first to study the effects of irradiation on organoid behavior.

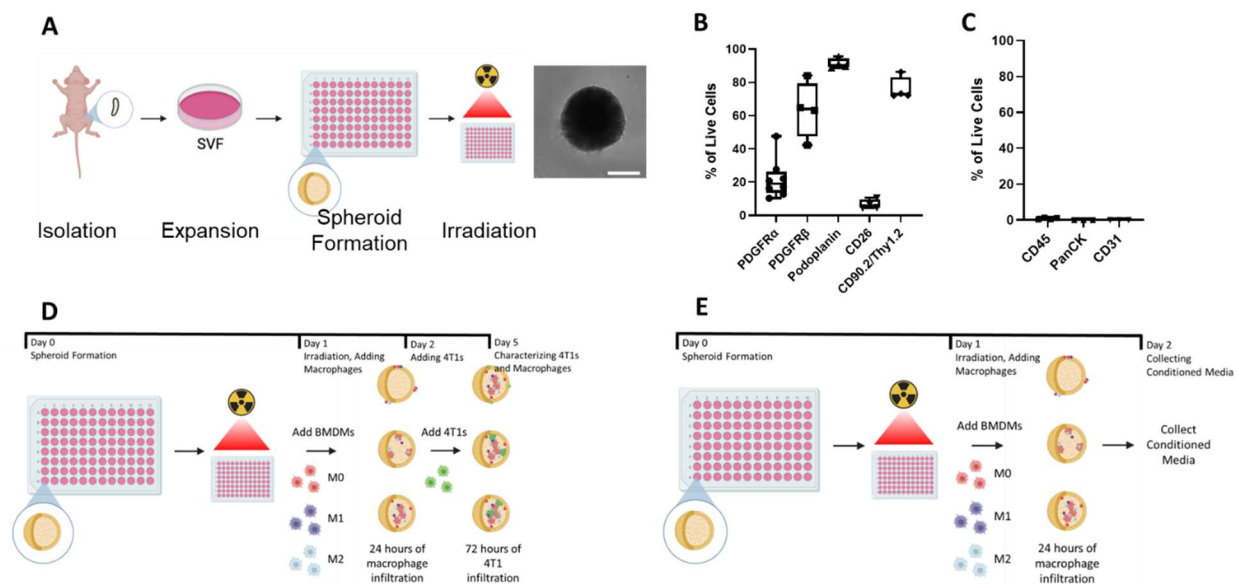


**Figure 3.4. Design of primary mammary organoids.**

**A.** Experimental schematic of stromal vascular fraction (SVF) isolation from mouse MFPs, expansion, and irradiation. Brightfield image of representative organoid. Scale bar is 100  $\mu\text{m}$ . **B.** SVF cells are composed of cells of fibroblast lineage based on flow cytometry characterization. Data is presented as a box and whiskers plot, with the minimum, maximum, first quartile, median, and third quartile shown. **C.** SVF cells show negligible expression of immune, epithelial, and endothelial cells. **D.** Schematic of co-culture experiments with organoids, macrophages, and 4T1 cells. **E.** Schematic of co-culture experiments of organoids and macrophages for conditioned media collection.

### 3.4.3. Direct co-culture experiments with M0 macrophages

Radiation induces significant infiltration of macrophages in normal mammary tissue<sup>193</sup>, and excess macrophages can cause tumor growth, metastasis, and recurrence<sup>45,193</sup>. We added primary mouse bone marrow derived macrophages (BMDMs) to our organoid model to study how macrophage infiltration influences tumor cell behavior. Other studies have modeled macrophage infiltration using multiple tissue types<sup>128</sup>. Based on the results of our *in vivo* studies (**Figure 3.5 A, B**), we added macrophages at a proportion of 15% of the overall cells.

Previous studies have shown that in some conditions, *in vitro* culture of macrophages can induce phenotypic changes without the addition of recombinant cytokines<sup>128</sup>. Higher M2 to M1 macrophage ratios have been shown to be associated with a poorer prognosis and therefore could be linked to a higher likelihood of recurrence<sup>133,271</sup>. We evaluated how M0 macrophage phenotypes changed after co-culture in irradiated organoids for 24 hours. Interestingly, we saw a slight shift toward an M2 phenotype (**Figure 3.5 D**), perhaps due to the anti-inflammatory response to the irradiated stroma. Additionally, irradiated organoids were co-cultured with M0 macrophages and 4T1 tumor cells. 4T1 tumor cell proliferative capacity was evaluated by Ki-67 staining. 4T1 cells co-cultured with macrophages saw a significant increase in relative Ki-67 expression in irradiated microenvironments (**Figure 3.5E**). Altogether, this data suggests that macrophages cultured in an irradiated microenvironment may adopt more of an M2, tumor associated phenotype, and therefore facilitate pro-tumor functions.

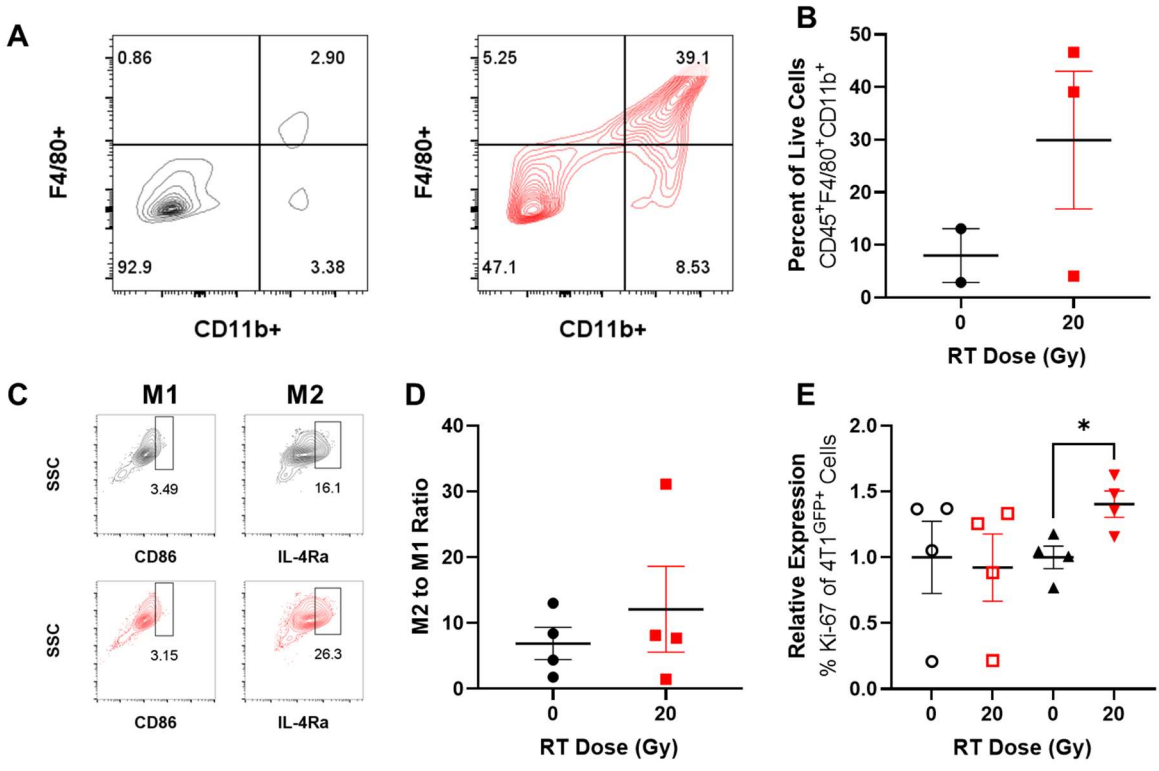


**Figure 3.5. Direct co-culture with M0 macrophages influences the irradiated microenvironment.**

**A.** Gating of macrophages in control (0 Gy, black) and irradiated (20 Gy, red) mammary fat pads, 10 days post *in vivo* RT. **B.** Quantification of infiltration of CD45<sup>+</sup>CD11b<sup>+</sup>F4/80<sup>+</sup> macrophages 10 days post-RT. **C.** Flow cytometric plots of expression of M1 and M2 markers on F4/80<sup>+</sup> macrophages in control (black) and irradiated (20 Gy, red) organoids. **D.** Quantification of ratios of M2:M1 macrophages in irradiated organoids after 24 hours co-culture. **E.** Proliferative capacity of 4T1<sup>GFP+</sup> cells co-cultured with irradiated organoids treated with 0 (black) and 20 Gy (red) irradiation, with (filled symbols) and without (open symbols) M0 macrophages, 72 hours post co-culture. Expression is normalized relative to each unirradiated control. Data is mean ± SEM with \*p<0.05 as determined by ANOVA.

### 3.4.3 The irradiated microenvironment facilitates TNBC cell recruitment through direct organoid -macrophage interactions

To examine the effects of macrophages that had already been polarized to adopt either a pro- or anti-inflammatory phenotype, we added previously polarized macrophages to co-culture models.

Using observations from *in vivo* models (**Figures 3.2, 3.5 C**), M0, M1, and M2 macrophages were added to the cultures at proportions of 85%, 5%, and 10% of the overall macrophage population, respectively. To replicate *in vivo* observations of macrophage infiltration, macrophages were added immediately after irradiation (**Figure 3.4.D,E**). Using scanning electron microscopy, we observed adhesion and infiltration of macrophages and 4T1s into organoids after irradiation (**Figure A.3.3.C**). Macrophage co-culture and irradiation did not cause any significant differences in organoid size or aspect ratio (**Figure A.3.3.D**). We confirmed infiltration of M1 and M2 macrophages into organoids after 24 hours (**Figure A.3.4.A**).

Matrix metalloproteinase 9 (MMP9) stimulates primary TNBC tumor growth, angiogenesis, and metastasis<sup>83</sup>, but the contribution of local secretion of MMP9 in the irradiated microenvironment to recurrence is relatively unexplored. We observed enhanced MMP9 expression in organoids co-cultured with macrophages 3 days following RT (**Figure 3.6**). This suggests that upon infiltration, macrophages facilitate ECM degradation that may further prime the microenvironment for 4T1 invasion.

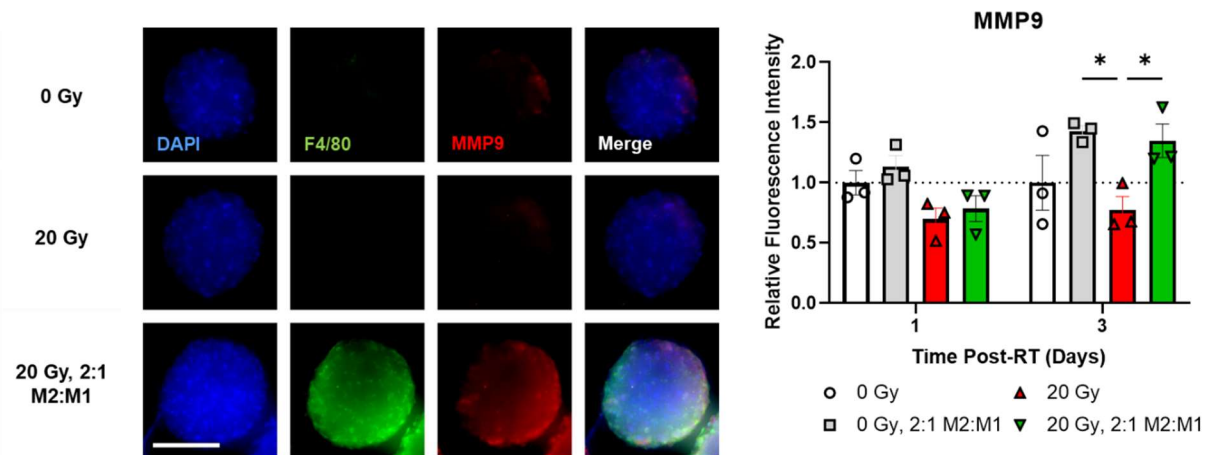


**Figure 3.6. Organoid macrophage (macs) co-culture facilitates enhanced secretion of MMP9.** Representative images of immunofluorescence staining of nuclei (blue), F4/80+ macrophages (green), and MMP9 (red) in organoids 3 days post-RT. MMP9 fluorescence intensity was quantified using Fiji and normalized to 0 Gy for each time point (n = 3). Scale bars are 200  $\mu\text{m}$ . Error bars show standard error of the mean with \* $p < 0.05$  as determined by ANOVA.

We also confirmed that 4T1 murine TNBC cells infiltrated into organoids (**Figure A.3.4.B**). We tracked individual cell infiltration via live cell imaging (**Figure 3.3.A**). When 4T1 cells were co-cultured with macrophages in irradiated organoids, they showed significantly higher motility toward the center of the organoid. GFP intensity in the inner core of the organoid was normalized to the overall GFP intensity of the organoid after 24 hours of infiltration (**Figure 3.3.B**). In the case of 2:1 M2:M1 macrophages, interior GFP intensity significantly increased, indicating that 4T1 cells were more invasive when cultured in organoids that recapitulate a microenvironment that has been shown to promote tumor cell recruitment *in vivo*<sup>193</sup>. Additionally, GFP intensity was measured as a function of radial distance from the center (**Figure 3.3.C**). After 72 hours of co-culture, GFP intensity closer to the interior of the organoid was significantly increased in irradiated organoids with macrophages relative to both the stromal only irradiated and unirradiated controls. These results show that direct interactions between macrophages and the

irradiated stroma facilitate 4T1 recruitment. Macrophages maintained relevant levels of expression of M1 (CD86) markers and M2 (IL4Ra) markers for up to 4 days within the co-culture (**Figure A.3.4.C**).

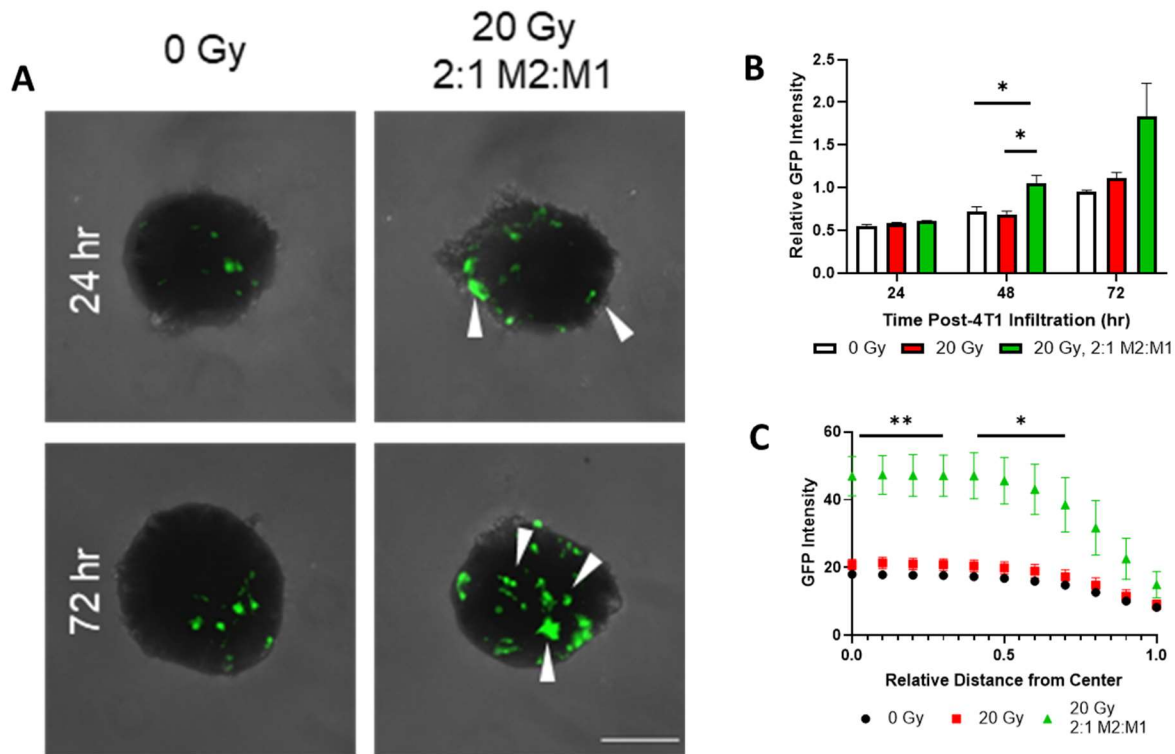


**Figure 3.7. Cell infiltration into organoids is enhanced by co-culture of irradiated stroma and infiltrating macrophages.**

**A.** GFP-labeled 4T1 infiltration was tracked at 24- and 72-hours following co-culture with organoids. Infiltration was enhanced in the presence of 2:1 M2:M1 macrophages co-cultured with irradiated organoids. **B.** GFP signal from 4T1s is enhanced in the interior of the organoid over time (n=3-4 biological replicates). Interior organoid GFP intensity was normalized to the total GFP intensity within the entire organoid at 24 hours of co-culture. **C.** GFP intensity increases with macrophage co-culture as a function of radial distance at 72 hours. Error bars show standard error of the mean with \*p < 0.05 and \*\*p < 0.01 as determined by a two-tailed unpaired t-test. White arrows indicate cell infiltration. Scale bars are 200  $\mu$ m.

#### 3.4.4 IL-6 secretion drives 4T1 cell invasiveness *in vitro*

We isolated conditioned media (CM) from co-cultures of macrophages and irradiated organoids. We characterized IL-6 secretion from organoids as a function of irradiation and macrophage infiltration to determine if *in vivo* cytokine secretion is replicated in our model. We observed that infiltration of macrophages (2:1 M2:M1) resulted in a significantly higher secretion of IL-6 relative to organoids with no macrophage infiltration (**Figure 3.8.A**). Additionally, when macrophages were co-cultured with unirradiated organoids, we observed no significant changes in IL-6 secretion. Interestingly, the co-culture of M0 macrophages with irradiated organoids did not change IL-6 secretion (**Figure 3.8.B**). These observations establish the importance of maximizing biological relevance by incorporating multiple macrophage phenotypes into organoid models.

The impact of IL-6 on 4T1 invasiveness was then investigated using a transwell assay. 4T1 invasiveness was significantly higher when incubated with CM from irradiated organoids with macrophages relative to CM collected from organoids with no macrophages (**Figure 3.8.C**), and neutralization of IL-6 in CM resulted in nearly fourfold reduction in invasiveness of 4T1 cells. Invasion was also significantly lower in CM from unirradiated organoids co-cultured with macrophages. Previous studies have shown that neutralization of IL-6 reduces invasiveness of 4T1 cells and that macrophage-derived IL-6 contributes to tumor cell migratory ability<sup>29,192</sup>. However, we are the first to show the dependence of 4T1 invasiveness on IL-6 secreted from stromal-macrophage interactions.

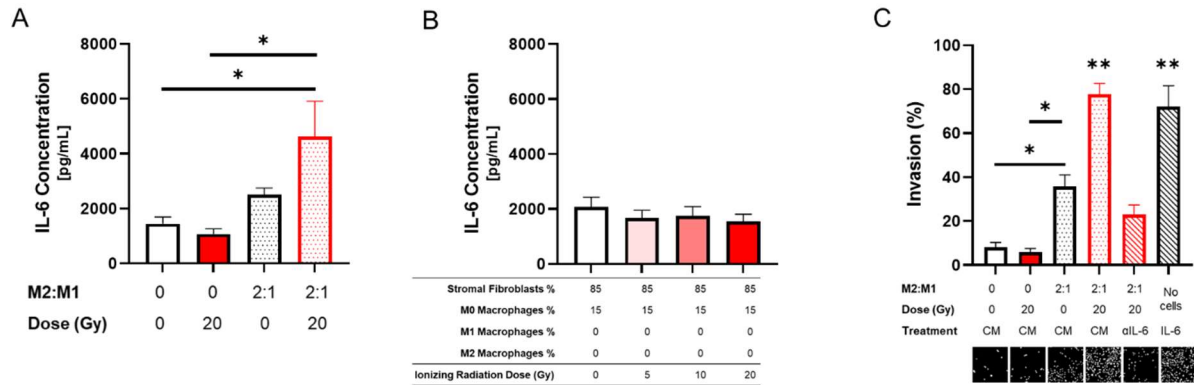


**Figure 3.8. IL-6 secretion drives tumor cell invasion post-RT in vitro.**

**A.** Organoid conditioned media (CM) incubated for 24 hours after RT promotes IL-6 secretion when cultured with a 2:1 ratio of M2:M1 macrophages (red, dotted). IL-6 secretion is lower in the absence of organoid RT (black), with organoid RT and no macrophage infiltration (solid red), or with macrophage co-culture without RT (black, dotted). **B.** IL-6 concentration in co-cultures with M0 macrophages does not change with RT dose. N=3 biological replicates per condition. **C.** IL-6 secreted from RT organoids co-cultured with macrophages promotes 4T1 cell invasion. IL-6 neutralization ( $\alpha$ IL-6, striped red) in CM of irradiated organoids with macrophage co-culture diminished invasion. Error bars show standard error of the mean with \* $p < 0.05$  and \*\* $p < 0.01$  as determined by ANOVA analysis. 20 Gy (red, dotted) and IL-6 spiked media (striped black) are significant to all other conditions.

### 3.4.5 IL-6 secretion drives 4T1 cell invasiveness *in vivo*

We then investigated the impact of IL-6 on tumor cell recruitment *in vivo*. IL-6 was systemically neutralized 6 hours before irradiation of contralateral MFPs in mice with orthotopic luciferase-labeled 4T1 tumors, and bioluminescence imaging (BLI) was used to quantify the luminescent signal from recruited tumor cells in MFPs. For each treatment, BLI was normalized to the non-irradiated control. Systemic depletion of IL-6 significantly reduced BLI levels after RT ( $p < 0.01$ ; **Figure 3.9.A**), indicating inhibition of tumor cell recruitment. IL-6 depletion was not observed to have significant off-target effects, including primary tumor growth and tumor metastasis, suggesting that this mechanism may be more specific to local recurrence (**Figures 3.9.B-D**).

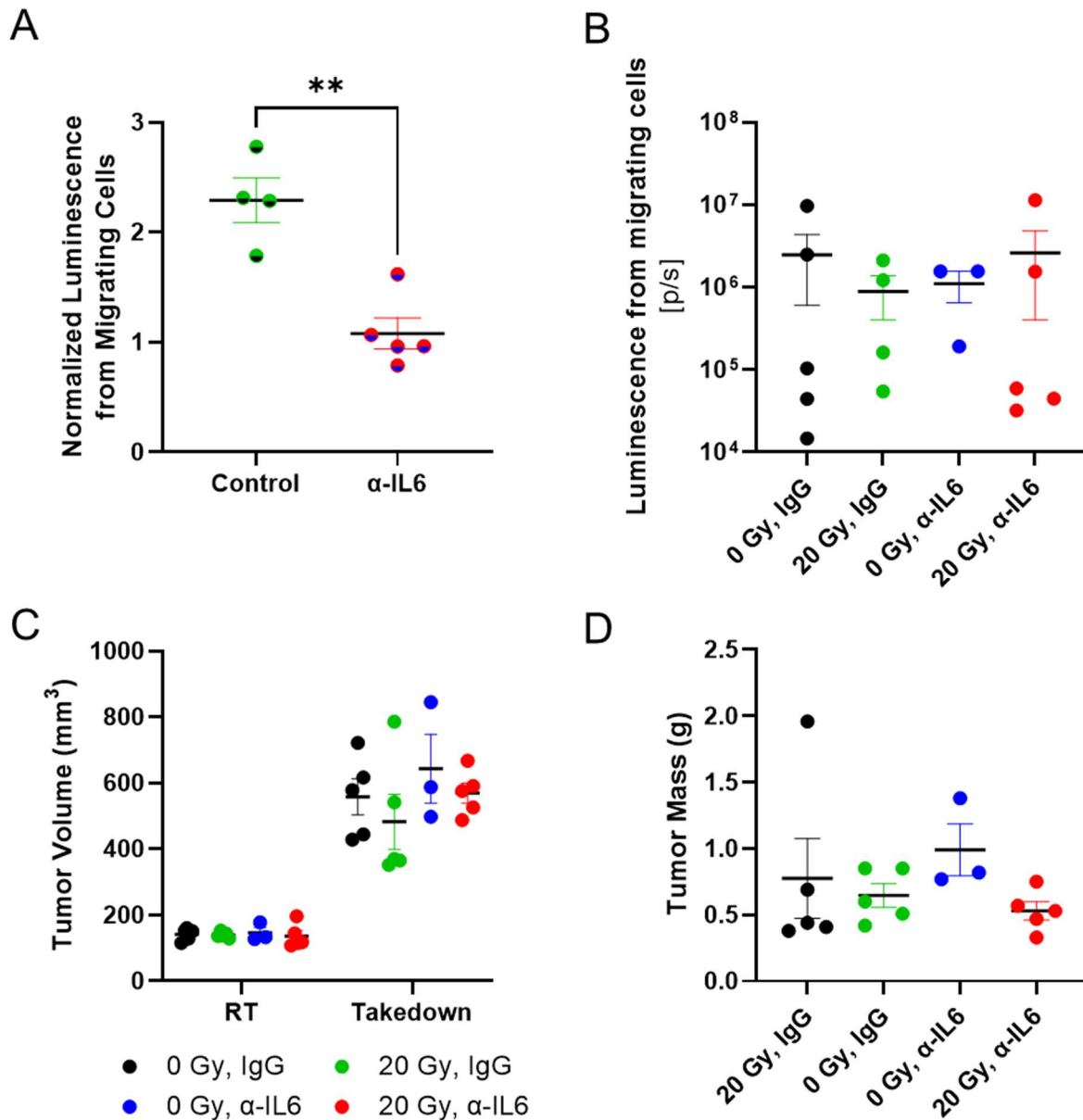


**Figure 3.9 IL-6 neutralization in vivo downregulates 4T1 cell invasion after irradiation.**

**A.** Luminescence from migrating cells was normalized to the unirradiated control for each treatment. Error bars show standard error of the mean with  $**p < 0.01$  as determined by unpaired, 2-tailed t-test. **B.** Luminescence measurements of lungs. **C.** Tumor volumes for the date of RT and takedown. **D.** Tumor masses at the date of takedown. No significant differences in tumor volume or mass were observed.

### 3.5 Conclusions and Future Work

Taken together, these data suggest that the interaction between tissue damaged from RT and M2 and M1 macrophages causes secretion of IL-6 that in turn recruits 4T1 cells (**Figure 3.10**). Myeloid-derived IL-6 has been reported in 4T1 progression and metastasis<sup>178,192</sup>. In the clinic, IL-6 inhibitors have been largely unsuccessful at preventing progression of primary disease, showing little efficacy in multiple myeloma, renal cell carcinoma, and prostate cancer<sup>200</sup>. Inhibition of IL-6R has been shown to hinder TNBC metastasis in a pre-clinical model<sup>252</sup>. However, there is limited knowledge of the clinical efficacy of IL-6 and IL-6R inhibitors in primary breast cancer progression and recurrence<sup>99</sup>. This is the first report of IL-6 driving 4T1 invasiveness post-RT in the context of local recurrence. This work highlights the importance of using 3D organoid models to elucidate mechanisms of cancer recurrence. Our results indicate that monitoring serum IL-6 levels may provide prognostic and therapeutic value in improving outcomes for TNBC patients vulnerable to recurrence.

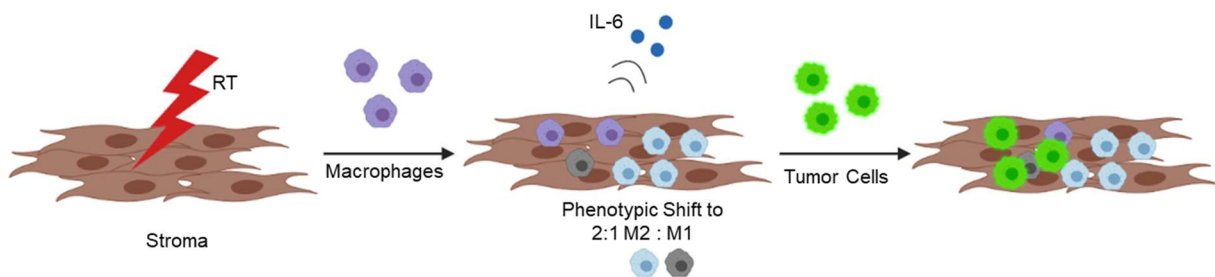


**Figure 3.10. Proposed mechanism of 4T1 tumor cell infiltration following normal tissue RT.**

## Chapter 4

### CYTOTOXIC T CELLS INFLUENCE PHENOTYPES OF RADIATION DAMAGED STROMA

#### 4.1 Summary

Triple negative breast cancer patients have vastly different outcomes depending on patient immune status. Immunocompromised patients are at much higher risk of experiencing recurrence<sup>193</sup>. Patients who are immunocompromised have low levels of white blood cells. Previous models have shown that within these population, CD8<sup>+</sup> T cells play a significant role in ablating recurrence after radiation treatment. It is known that CD8<sup>+</sup> T cells can play a role in the wound healing response. However, the mechanisms that drive aberrant wound healing post radiation treatment in the absence of CD8<sup>+</sup> T cells are unknown. Here, we developed a novel organoid model to evaluate how stromal-CD8<sup>+</sup> interactions influenced normal tissue wound healing.

First, we observed that changes in immune status significantly alter the secretome *in vivo*, which in turn affects the makeup of immune infiltrate to the irradiated site. We confirmed these observations by looking at intracellular protein expression. We observed dysfunctional cell repair and cytokine signaling cellular programs resulting from the removal of CD8<sup>+</sup> T cells from the wound healing process.

We then engineered an *in vitro* co-culture organoid model composed of fibroblasts and primary CD8<sup>+</sup> T cells. We analyzed how direct interactions with irradiated cells influenced T cell proliferation. Finally, we found that secreted factors from damaged tissue greatly inhibited

macrophage invasive capacity when in the presence of CD8+ T cells, further confirming previous *in vivo* observations.

## 4.2 Introduction

Lymphocytes play a critical role in anti-cancer immunity. Circulating lymphocytes are associated with overall prognosis in cancer patients. Patients with low absolute lymphocyte count (ALC) have poorer progression free survival, lower overall survival, and poorer prognosis for multiple cancer types, including ovarian, non-small cell lung, gastric, and nasopharyngeal cancer<sup>47,73,118,166</sup>.

In triple negative breast cancer, patients with low ALC are associated with having a higher degree of metastasis and a lower likelihood of overall survival<sup>4,116</sup>. In TNBC, ALC has been linked to tumor infiltrating lymphocytes (TILs), which are associated with improved disease free survival, complete responses, and overall survival rates<sup>81</sup>. Interestingly, in patients treated with breast conserving therapy, ALC is also an indicator of prognosis, where immunocompromised patients have a higher likelihood of locoregional recurrence<sup>193</sup>.

CD8+ T cells are a type of lymphocyte that exhibit anti-tumor immunity. Enhanced CD8+ T cell infiltration into TNBC tumors is associated with a better prognosis<sup>38,159</sup>. CD8+ T cells eliminate tumor cells via interactions between the T-cell receptor (TCR) and tumor cell major histocompatibility complex (MHC)-I. T cells recognize tumor associated antigen, which leads to the release of lysosomes containing cytotoxic granules like perforin and granzymes<sup>68</sup>.

In the tumor microenvironment, the immune response consists of an interplay between cells of the innate and adaptive immune system. The innate immune system consists of cells of a myeloid lineage, and the adaptive immune system consists of lymphocytes. Innate immune cells,

like macrophages and dendritic cells, take up tumor antigen and prime CD8<sup>+</sup> T cells via cross-presentation<sup>59</sup>. The innate immune system therefore facilitates expansion of effector CD8<sup>+</sup> T cells that can recognize and eliminate tumor cells. The maintenance of the CD8<sup>+</sup> T cell response, and the development of memory T cells also relies on signals from the innate immune system.

In non-tumor bearing environments that elicit an immune response, like infections, a similar order of interactions occur. Professional antigen presenting cells (APCs) in the innate immune compartment recognize pathogens and induce an adaptive immune response. Once again, the intensity, efficacy, and duration of the CD8<sup>+</sup> T cell response is highly influenced by innate immunity<sup>160</sup>. It is therefore interesting that in previous studies modeling tumor cell recruitment, the presence of CD8<sup>+</sup> T cells influences macrophage recruitment to damaged tissue<sup>193</sup>. This flips the conventional thinking, implying the CD8<sup>+</sup> T cells may directly influence the innate immune response.

Interestingly, CD8<sup>+</sup> T cells have been shown to be critical in mediating biological processes unrelated to anti-tumor or anti-pathogen immunity. CD8<sup>+</sup> T cells have been reported to be critical for the wound healing response in heart tissues by regulating the inflammatory response after myocardial infarction<sup>108</sup>. CD8<sup>+</sup> T cells also reduce cardiac fibrosis and improve cardiac function after injury by ablation of fibroblast activation protein<sup>5</sup>.

Exposure to stress can alter cellular phenotype. Damaged cells either undergo apoptosis or are destined for clearance by the immune system. Damaged cells attract immune cells by secreting pro-inflammatory cytokines, including interleukin (IL)-6, IL-1 $\beta$ , granulocyte-macrophage colony-stimulating factor (GM-CSF), and monocyte chemoattractant protein-1 (MCP-1)<sup>134</sup>. A variety of innate immune cells are recruited as a part of this process<sup>248</sup>. Natural killer cells have been shown to resolve cellular damage by killing senescent stellate cells, preventing liver cirrhosis<sup>127</sup>.

Additionally, stress and damage has been shown to affect how cells process self-peptides that are immunogenic<sup>85,195</sup>. CD8<sup>+</sup> T cells have also been shown to be activated upon interactions with damaged cells. For example, CD8<sup>+</sup> T cells have been shown to mediate cell death of irradiated fibroblasts<sup>185</sup>. However, very little is known about the role of CD8<sup>+</sup> T cells in the wound healing process in irradiated normal tissue microenvironments.

In this study, we developed a novel co-culture model of irradiated fibroblasts, CD8<sup>+</sup> T cells and macrophages. We then used our model to determine the contributions of CD8<sup>+</sup> T cells to resolving RT induced normal tissue damage and to further characterize stromal-CD8-macrophage interactions.

## **4.3 Materials and Methods**

### **4.3.1 Primary CD8<sup>+</sup> T cell isolation and culture**

T cells were isolated and cultured using methods previously published<sup>138,193</sup>. Spleens were resected from Balb/c mice. Excised spleens were pressed through a 40 micron cell strainer using a syringe plunger and rinsed with PBS/3% FBS. Cells were centrifuged at 1,600 rpm for 5 minutes, and resuspended in 1 mL ACK lysis buffer for 2 minutes to lyse red blood cells. ACK lysis was inactivated with PBS/3% FBS, spun down at 1,600 rpm for 5 minutes, and resuspended in PBS/3% FBS for quantification.

To separate T cells from other splenocytes, a CD8<sup>+</sup> isolation kit was used (Miltenyi). Cells were resuspended in Magnetic Activated Cell Sorting (MACS) Buffer and incubated with biotin-antibody cocktail at 4C for 5 minutes. Then, additional buffer and anti-biotin microbeads were added to the cell suspension, and cells were incubated at 4C for an additional 10 minutes. An LS column was placed on a QuadroMacs separator (Miltenyi) and prepped by rinsing with 3 mL of

buffer. After column prepping and cell incubation, the cell suspension was applied onto the column, and the flowthrough was collected as a pure CD8<sup>+</sup> T cell population. The column was rinsed with 3 mL of buffer to increase yield. The flowthrough of isolated CD8<sup>+</sup> T cells was pooled, spun down at 1100 RPM, resuspended in 1 mL of T cell media, and cell number was quantified.

To culture CD8<sup>+</sup> T cells, T cells were first activated by being cultured in activation media. This consisted of T cell media with 1 µg/mL of anti-CD3 and 0.5 µg/mL of anti-CD28. Cells were plated in the wells of a 48 well plate at a density of 6e5 cells/mL. Cells were left in activation media for 72 hours. After 3 days, cells were recovered by vigorously pipetting, spun down at 1100 RPM, and resuspended in T cell media. Cell density was adjusted to 6e5 cells/mL. For expansion media, IL-2 was added at a concentration of 60 U/mL. Cells were plated in 48 well plates at a density of 6e5 cells/mL. Every other day, cells were recovered and resuspended in fresh T cell expansion media. T cells were used for organoid co-culture experiments between 7 and 11 days post isolation. Activation and expansion media were both supplemented with 100 µM of β-mercaptoethanol.

#### **4.3.2 Cell Culture**

NIH 3T3 fibroblasts were obtained by American Type Cell Culture (ATCC) and cultured per ATCC specifications. Cells were maintained in Dulbecco's Modified Eagle Media (DMEM) supplemented with 10% bovine calf serum (BCS) and 1% penicillin-streptomycin. RMF fibroblasts were cultured in DMEM supplemented with 10% bovine calf serum (BCS) and 1% penicillin-streptomycin.

### **4.3.3 Organoid co-culture and irradiation**

Cells were plated at a density of  $2 \times 10^4$  cells per organoid in ultra low-adhesion 96 well plates (Thermo Scientific). 24-48 hours after organoid formation, plates were treated with RT. Immediately after RT, primary CD8<sup>+</sup> T cells were added to the culture at a density of 6,000 cells per organoid. 24 hours post-RT, primary bone marrow derived macrophages were added at a density of 3,000 cells per organoid. For all co-culture experiments, cell culture medium consisted of 50% complete fibroblast medium, 50% T cell media, supplemented with 60 U/mL IL-2, 10 ng/mL MCSF, and 100  $\mu$ M  $\beta$ -mercaptoethanol. Organoids were utilized for various downstream analyses.

### **4.3.4 Organoid Fixation, Staining, and Imaging**

2 and 5 days post-RT, Organoids were carefully transferred to microcentrifuge tubes using wide bore pipet tips. Organoids were rinsed in PBS and fixed in 10% Neutral Buffered Formalin overnight at 4°C. Organoids were transferred to PBS after fixation. They were blocked and permeabilized in buffer containing 1% BSA, 1% DMSO, 1% Triton-X 100, and 1% NGS for 1 hour at room temperature on an orbital shaker. After blocking, they were incubated with primary antibodies for 72 hours at 4°C. After primary antibody incubation, organoids were rinsed 5 times, then incubated with secondary antibodies (1:200), Hoechst (2  $\mu$ M), and phalloidin (Thermofisher) for 48 hours at 4°C. After secondary incubation, organoids were rinsed 5 times, carefully transferred to a glass slide, mounted with a coverslip, and imaged. Fiji was used for image analysis.

#### **4.3.5 Invasion Assay**

Conditioned media (CM) collected from organoid and T cell co-cultures was used as chemoattractants in a transwell migration assay (Corning reduced growth factor Matrigel invasion chamber, 8  $\mu\text{m}$  pore size). Organoids were irradiated to 20 Gy and then co-cultured with CD8<sup>+</sup> T cells. Supernatant was collected after 48 hours of co-culture. 100,000 bone marrow derived macrophages were seeded into the upper chambers and incubated with CM for 24 hours<sup>265</sup>. Cells that invaded through Matrigel inserts were stained with NucBlue mounting media and nuclei were counted. Normalized invasion was calculated by dividing invasion counts by average invasion counts for baseline, immunocompromised conditions.

#### **4.3.6 Reverse Phase Protein Array (RPPA)**

Proteins were analyzed at the RPPA core facility at the MD Anderson Cancer Center. Frozen mammary fat pads were lysed and protein was extracted using RPPA lysis buffer. Lysates were serially diluted in 5 two-fold dilutions with lysis buffer and printed on nitrocellulose-coated slides using an Aushon Biosystems 2470 arrayer. Slides were probed with approximately 500 validated primary antibodies followed by detection with appropriate biotinylated secondary antibodies (Goat anti-Rabbit IgG, Goat anti-Mouse IgG, or Rabbit anti-Goat IgG). The signal obtained was amplified using streptavidin-conjugated horseradish peroxidase (HRP) binding to the secondary antibody and catalyzing biotinylated tyramide to form insoluble biotinylated phenols. Signals were visualized by a secondary streptavidin-conjugated HRP and DAB colorimetric reaction. The slides were scanned, analyzed, and quantified using Array-Pro Analyzer software (MediaCybernetics) to generate spot intensity (Level 1 data). SuperCurve GUI, was used to estimate relative protein levels (in log<sub>2</sub> scale). A fitted curve ("Supercurve") was created with signal intensities on the Y-axis and

relative log<sub>2</sub> amounts of each protein on the X-axis using a non-parametric, monotone increasing B-spline model. Raw spot intensity data were adjusted to correct spatial bias before model fitting using “control spots” arrayed across the slides. A QC metric (4) was generated for each slide to determine slide quality and only slides greater than 0.8 on a 0-1 scale were included for further processing. For replicate slides, the slide with the highest QC score was used for analysis (Level 2 data). Protein measurements were corrected for loading as described using bidirectional median centering across samples and antibodies (Level 3 data). Samples with low protein levels were excluded from further analysis. Antibodies were selected to represent the breadth of cell signaling and repair pathways conditioned on a strict validation process as previously described.

#### **4.3.7. Luminex Multiplex Cytokine Assay**

Spheroid co-cultures were prepared as described above with reduced BCS media (2%). 2 and 5 days post-RT, CM was collected and flushed through a 40 µm cell strainer. Media was stored at -80°C. Samples were processed at Eve Technologies using a mouse 39-plex Affymetrix kit.

### **4.4 Results and Discussion**

#### **4.4.1 Phenotypes associated with cell damage are upregulated and persistent in immunocompromised mice**

We characterized changes in mammary fat pad cytokine expression at various timepoints after irradiation (**Figure 4.1**). Cytokine expression levels in mammary glands from immunocompromised mice were compared to levels in immunocompetent mice (**Figure 4.1 A, B**). Interestingly, we saw a sustained increase in GM-CSF, IL-1 $\beta$ , IL-6, and TGF- $\beta$  (**Figure 4.1 C**).

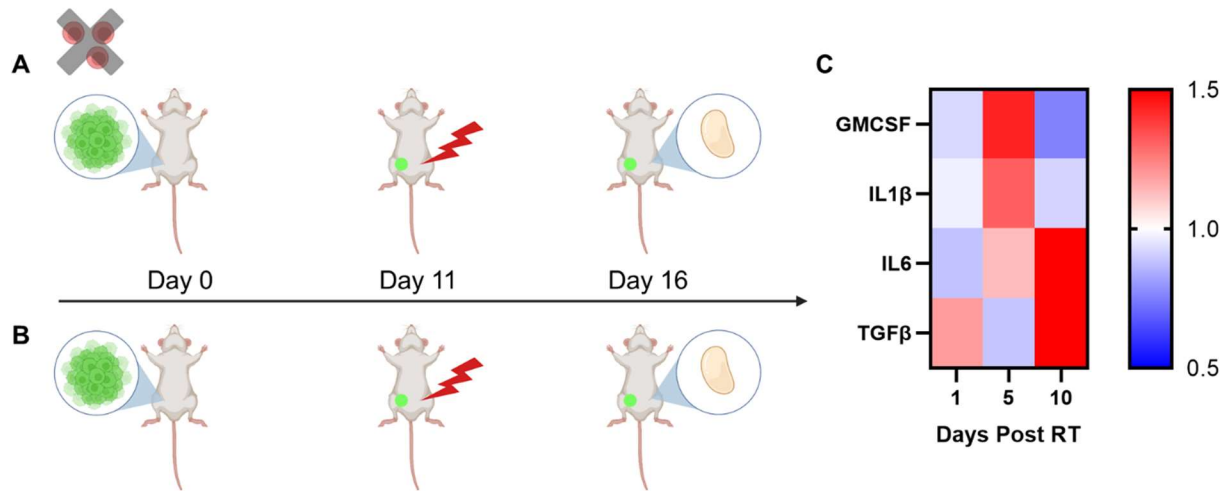


**Figure 4.1. Timeline of in vivo 4T1 recruitment studies.**

**A.** Mice immune status was modulated by (A) depleting CD8<sup>+</sup> T cells or (B) allowing mice to retain immunocompetency. In both models, mice were inoculated with 4T1 cells, and irradiated 11 days post tumor cell inoculation. Mammary glands were recovered 5 days post-RT. **C.** Fold changes of cytokines in mammary fat pads of immunocompromised mice with tumor cell recruitment. Values were normalized to those from immunocompetent healthy mice with no tumors.

GMCSF and IL1B are pro-inflammatory cytokines<sup>94,98</sup>. TGFβ is secreted in response to radiation damage, and is generally associated as an anti-inflammatory cytokine<sup>19</sup>. Taken together, the sustained upregulation of these cytokines could be associated with extended and unresolved normal tissue damage<sup>134</sup>.

#### 4.4.2 CD8<sup>+</sup> T cell depletion alters the microenvironmental damage response post *in vivo* RT

Next, to better determine the influence that CD8<sup>+</sup> T cells have on resolution of cellular stress and damage, we examined how intracellular protein expression changed after radiation therapy in the absence of cytotoxic T cells. We performed reverse phase protein array (RPPA) analysis on 246 proteins. We analyzed changes in expression at 5 days post-RT, a timepoint associated with

significant macrophage infiltration<sup>193</sup>. We noticed significant downregulation in the expression of 36 proteins, and significant upregulation in the expression of 20 proteins (**Figure 4.2**), suggesting that CD8+ T cells may play a significant role in the normal tissue wound healing response.

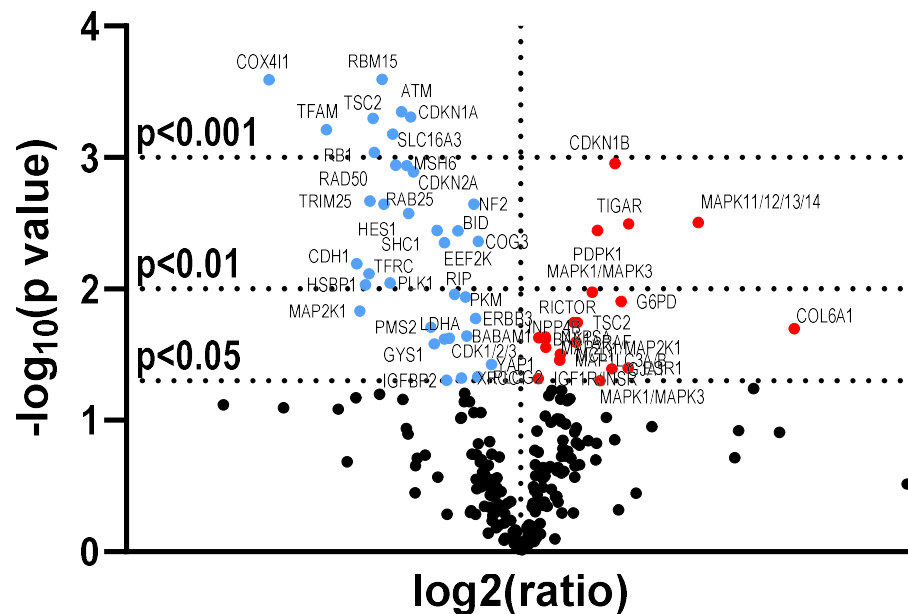


**Figure 4.2. Depletion of CD8+ T cells causes significant changes in protein expression in the wound healing response post in vivo RT.**

Volcano plot of relative change in proteins in irradiated MFPs. Differences were calculated by normalizing RPPA protein levels 5 days post-RT in immunocompromised tumor bearing mice to values from irradiated immunocompetent tumor bearing mice. N = 5 biological replicates.

We then analyzed different groups of pathways associated with significant changes in protein expression using Reactome, an open-source, peer-reviewed pathway database. We found significant changes in pathways corresponding to cellular responses to stress (**Table 4.1**).

**Table 4.1. Proteins with significant fold change and their associated pathways.**

Downregulated (blue) and upregulated proteins (red) 5 days post-RT. Values from immunocompromised mice were normalized to immunocompetent mice.

| Category                                   | Protein       | Fold Change | p value |
|--|---------------|-------------|---------|
| Regulation of Cellular Responses to Stress | Cox-IV        | 0.69        | <0.001  |
|  | HSP27_pS82    | 0.79        | <0.01   |
|  | Rb_pS807_S811 | 0.80        | <0.001  |
|  | Rad50         | 0.83        | <0.01   |
|  | ATM           | 0.84        | <0.001  |
|  | p21           | 0.85        | <0.001  |
|  | p27-Kip-1     | 1.15        | <0.01   |

Cytochrome C oxidase (Cox) -IV is involved in triggering the apoptotic cascade. It is also involved in a major step in mitochondrial respiration<sup>139</sup>. Previous studies have shown that cell stress induced by H<sub>2</sub>O<sub>2</sub> leads to a down-regulation in COX-IV mRNA<sup>140</sup>. Decreased levels of the protein may imply decreased mitochondrial respiration and elevated cellular stress levels. Heat shock protein (Hsp)-27 is normally overexpressed in cells that are stressed, so the downregulation of this chaperone protein implies a loss of its protective function<sup>132,222</sup>. Retinoblastoma (Rb)\_pS807\_S811 is involved in the regulation of cellular proliferation by controlling the cell's transition into the G1 phase of the cell cycle<sup>216</sup>. It has been reported that irradiation of fibroblasts induces phosphorylation on sites S807/S811, so decreased levels of this protein may imply that the absence of CD8<sup>+</sup> T cells results in dysregulation in the cell cycle in irradiated normal tissue cells<sup>205</sup>. Rad50 and ATM are both involved in DNA double strand break repair, so downregulation of these proteins may imply that incomplete repair due to radiation damage is occurring<sup>82</sup>. P27-Kip-1 promotes cell cycle exit in lymphocytes, has been reported to downregulate cell proliferation in epithelial cells, and is associated cell cycle arrest in mammary embryonic fibroblasts<sup>52,237,238</sup>. Taken together, these findings reveal how the absence of cytotoxic T cells results in differences in

normal tissue cell ability to self-regulate apoptosis, apply cell protection, undergo proliferation, and regulate cell cycle stages in response to stress induced by ionizing radiation.

#### 4.4.3 Development of a Fibroblast - CD8+ T cell co-culture model RT

To help eliminate effects from other biological processes associated with wound healing and fibrosis, we set out to develop an *in vitro* model that would allow us to individually isolate the effects of CD8+ T cells on the wound healing response. To do this, we sought to use primary CD8+ T cells isolated from Balb/C mice. We first confirmed that our isolation techniques were able to obtain a pure population of T cells via flow cytometry (**Figure 4.3**).

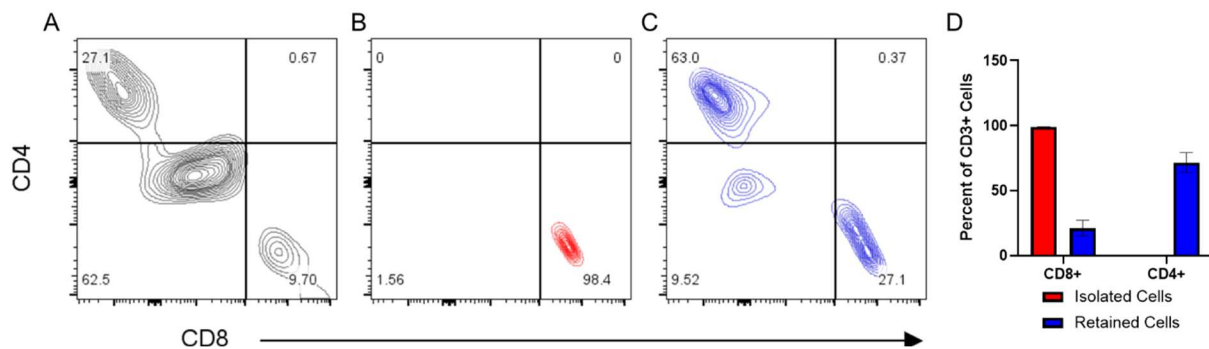


**Figure 4.3. T cell isolation produces a pure CD8+ T cell population.**

Flow cytometric plot of CD45+CD3+ cells pre-isolation (black) (A), post-isolation (red) (B), and retentate of isolation (blue) (C). **D.** Quantification of CD8+ and CD4+ T cells as a proportion of the cell isolate (red) and retentate (blue). Data is mean  $\pm$  SEM, n=2 biological replicates.

Next, we sought to incorporate our T cells into our organoid model. This would allow for direct co-culture, better mimicking *in vivo* conditions<sup>92</sup>. We labelled T cells with a fluorescent cell tracer, and then added them to organoid cultures. We performed live cell imaging every hour to monitor T cell co-localization and infiltration into organoids. We observed that within 1-2 hours, T cells adhered to and infiltrated into organoids (**Figure 4.4**).

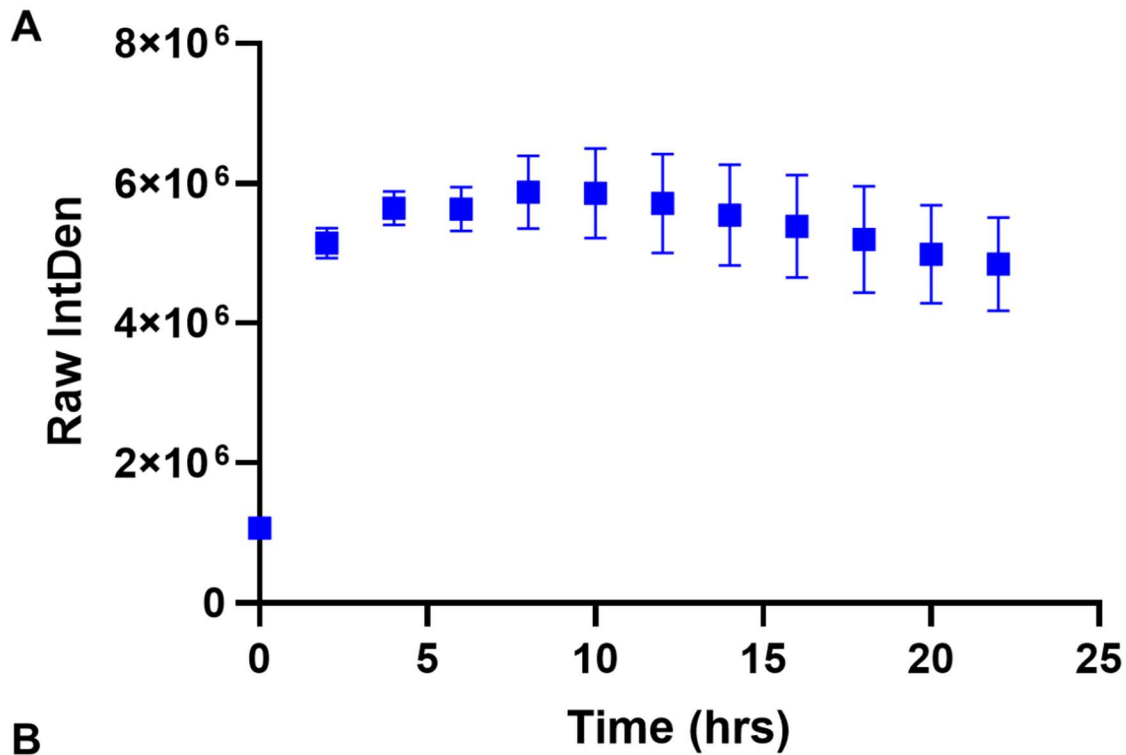


**Figure 4.4. T cell infiltration into organoids.**

**A.** Fluorescent intensity of T cells within organoids as a function of time. **B.** T cells at initial seeding point, 1, 2, and 24 hours after infiltrating into organoids. Data is mean  $\pm$  SEM, scale bar is 200  $\mu$ m. N = 4 replicates.

Due to the fast infiltration of the lymphocytes, we determined that we would be able to set up a static model of cell infiltration. In our immunocompetent irradiated microenvironment, we set up our model by irradiating organoids, performing a double media change, then immediately adding cytotoxic T cells to the organoids. This allowed us to avoid potentially altering CD8<sup>+</sup> T cell phenotypes or killing the cells from resulting radiosensitivities<sup>101</sup>.

#### **4.4.4 – CD8+ T cells are activated and proliferate in response to direct contact with irradiated fibroblasts**

In our co-culture model, we utilized cell ratios obtained from previously published data<sup>193</sup>. Organoids were plated at a size of 20,000 cells per organoid. 6,000 CD8+ T cells were added per organoid. Two days after irradiation, cells were also recovered, processed into a single cell suspension, stained, and analyzed via flow cytometry. Interestingly, CD8+ T cells made up a larger proportion in irradiated microenvironments (**Figure 4.6 A, B**). Increased CD8+ T cell *in vitro* proliferation is associated with increased levels of T cell activation<sup>138,186</sup>. This data was further bolstered with immunofluorescent staining, also performed 2 days post-RT (**Figure 4.6C-E**). We observed higher levels of CD8+ expressing cells, implying that the CD8+ T cells within the organoids were proliferating at a faster rate. While altered expression of self-peptides has been reported to elicit a T cell specific response, this is unlikely the mechanism of activation as the NIH 3T3 cells and primary CD8+ T cells have different haplotypes and are therefore not MHC matched. It is more likely that the mechanism is driven by cytokine signaling from the irradiated cells. Altogether, this data suggests that interactions between CD8+ T cells and damaged tissue may be a necessary and normal part of the wound healing response.

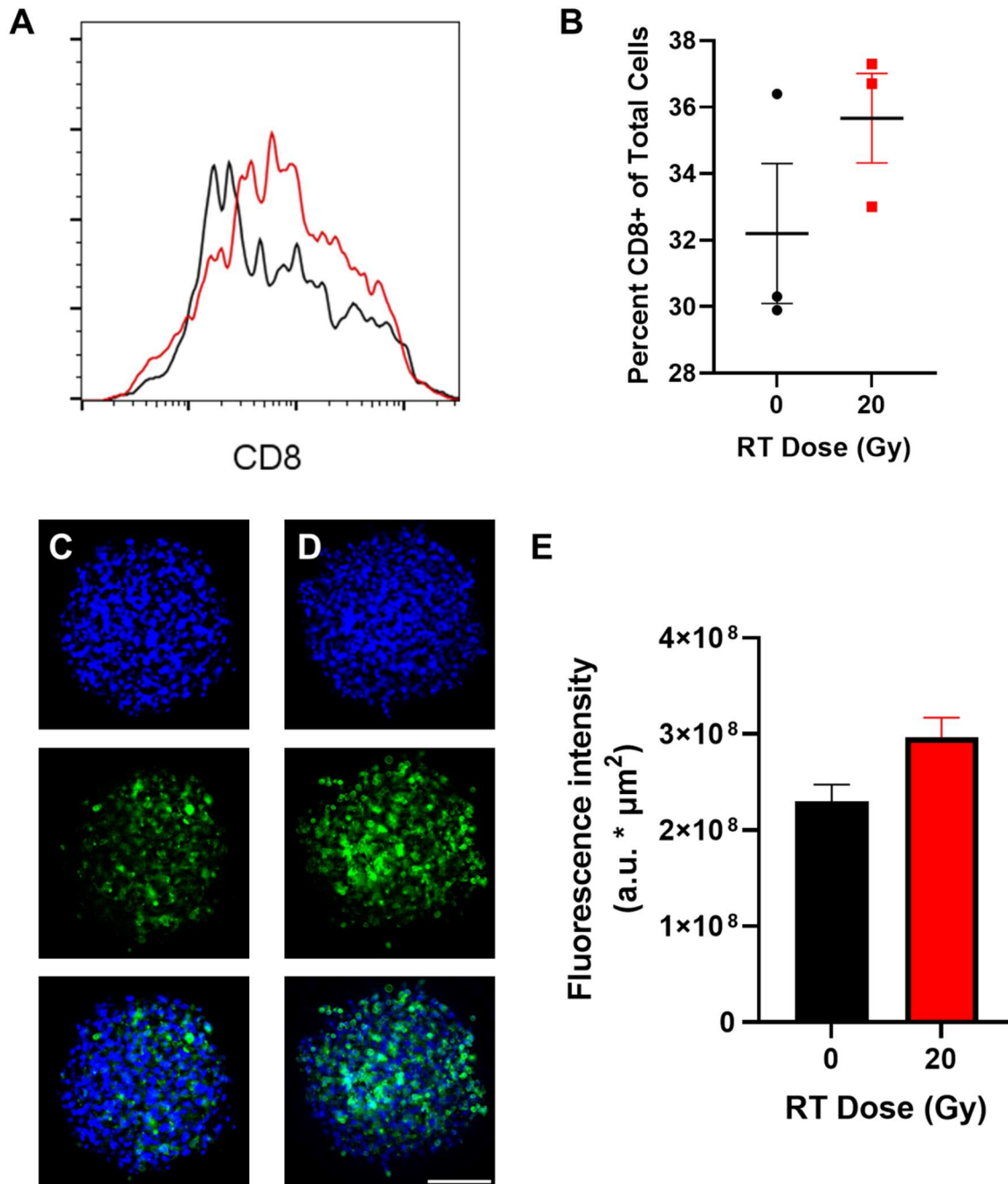


**Figure 4.6. CD8+ T cell proliferation is enhanced when co-cultured in irradiated organoids.** **A.** Overlay of CD8+ T cells in unirradiated (black) and irradiated (red) organoids. **B.** CD8+ T cells as a proportion of total cells after 2 days of co-culture. N=3 biological replicates. Immunofluorescent images of control (**C**) and irradiated (**D**) organoids after 2 days of co-culture with CD8+ T cells. Blue = Hoechst nuclear stain; green = CD8+ stain. Scale bar is 100  $\mu\text{m}$ . **E.** Fluorescence intensity of CD8+ positive cells in organoid co-cultures, N = 3 biological replicates. Data is mean  $\pm$  SEM.

#### 4.4.5 CD8+ T cells may contribute to macrophage phenotypic changes.

Macrophages are professional APCs, and they express low levels of MHC II endogenously. Higher MHC II expression on macrophages is associated with anti-tumor immunity<sup>182</sup>. Interestingly, when macrophages were co-cultured with CD8+ T cells in irradiated organoids, we observed a significant increase in MHC II expression (**Figure 4.7**).

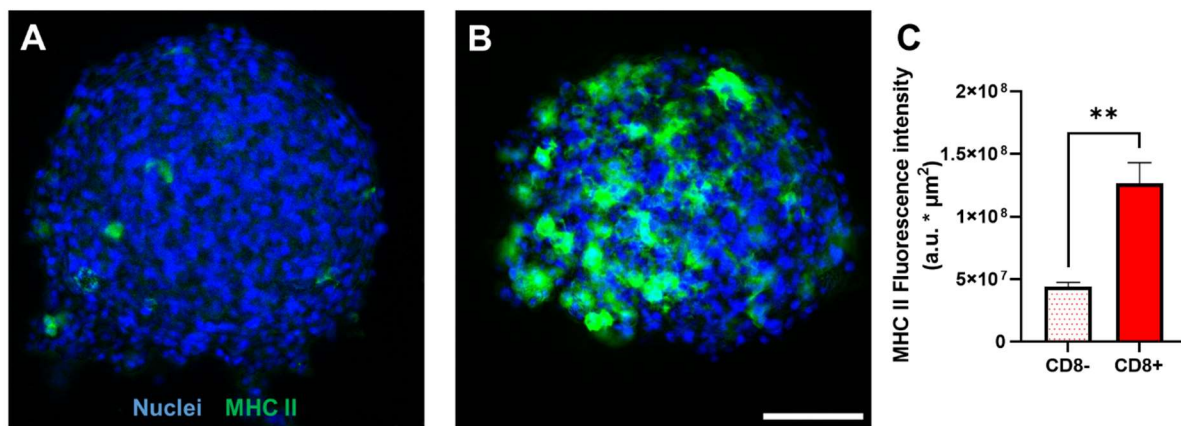


**Figure 4.7. Co-culture with CD8+ T cells enhances macrophage MHC II expression.**

Macrophages were cultured in CD8- (A) and CD8+ organoids. Blue = Hoechst nuclear stain; green = MHC II. C. MHC II fluorescence intensity was quantified. Data is mean ± SEM, N = 3 biological replicates.

MHC II expression can be induced by secretion of IFN  $\gamma$  from CD8+ T cells<sup>34</sup>. Interestingly, macrophages utilize MHC II to express antigen to CD4+ T cells as part of the adaptive immune response. This data suggests that the absence of CD8+ T cells may influence macrophage-CD4+ T cell signaling, suggesting that the interplay between all three of these cell types is crucial for preventing tumor cell recruitment to irradiated sites.

#### 4.4.6 Co-culture with CD8<sup>+</sup> T cells alters the secretome *in vitro*

Cytokines are proteins that are involved in cellular communication and signaling, immune modulation, and promoting and regulating inflammation<sup>241</sup>. Cytokines can have a variety of complex and sometimes contradictory roles depending on the cells they are being secreted from and the biological context. To better understand the role that CD8<sup>+</sup> T cells play in the wound healing process, we analyzed conditioned media for secreted cytokines 48 hours after irradiation and co-culture with CD8<sup>+</sup> T cells (**Figure 4.8**).

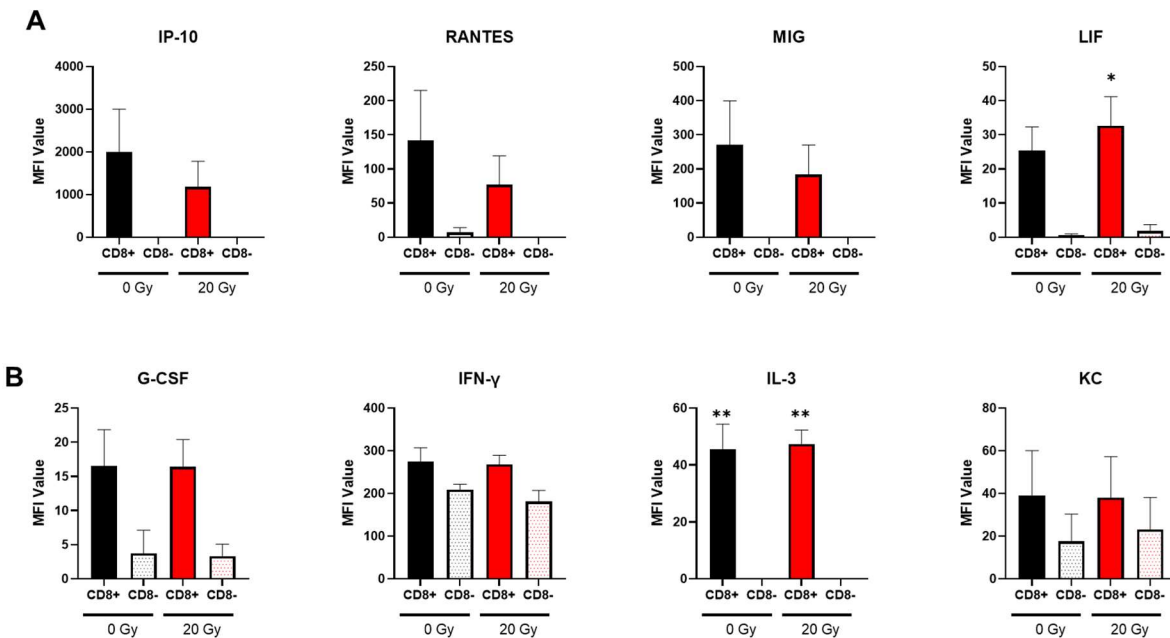


**Figure 4.8. MFI values of various cytokines 48 hours after irradiation and co-culture with CD8<sup>+</sup> T cells.**

A. MFI values of cytokines with variation in expression after irradiation in CD8<sup>+</sup> organoids. B. MFI values of cytokines with variation in expression after co-culture with CD8<sup>+</sup> T cells. Data is mean  $\pm$  SEM, N = 3 biological replicates. \* p < 0.05; \*\* p < 0.01 as determined by one way ANOVA.

Interferon gamma-induced protein 10 (IP-10), regulated upon activation, normal T cell expressed and presumably secreted (RANTES), and monokine induced by gamma interferon (MIG)

expression were all decreased after irradiation in CD8<sup>+</sup> organoids. IP-10 can act as a chemoattractant for CD8<sup>+</sup> T cells and is associated with recruiting cells for a Th1 response<sup>184</sup>. RANTES is another chemokine that acts to recruit a variety of lymphocytes. Lower levels of RANTES have been shown to increase CD8<sup>+</sup> T cell antitumor immunity; however, complete knockout of RANTES limits CD8<sup>+</sup> T cell cytotoxic efficacy against viruses<sup>55,272</sup>. MIG has been shown to increase CD8<sup>+</sup> T cell motility into tumors<sup>183</sup>. Leukemia inhibitory factor (LIF) expression was upregulated after irradiation in CD8<sup>+</sup> organoids. Interestingly, LIF has been shown to promote immuno-regulatory T cells<sup>113</sup>.

Granulocyte colony-stimulating factor (G-CSF), interferon gamma (IFN- $\gamma$ ), IL-3, and keratinocyte chemoattractant (KC) were upregulated in CD8<sup>+</sup> organoids irrespective of irradiation status. G-CSF has been shown to alter APC capability; yet can also cause recruitment of regulatory T cells<sup>201</sup>. IFN- $\gamma$  secretion is a hallmark of CD8<sup>+</sup> T cell activity, and its upregulation in CD8<sup>+</sup> organoids may explain increased MHC II expression observed in **figure 4.7**. IL-3 can be secreted to promote inflammation and cytotoxic T cell proliferation<sup>256</sup>. Interestingly, KC has been shown to downregulate CD8<sup>+</sup> T cell responses<sup>103</sup>.

Altogether, this data suggests that CD8<sup>+</sup> T cells are exhibiting some of their normal effector functions while also potentially secreting factors that would result in their regulation. However, because of the tight control and complex interplay exhibited between various T cell phenotypes, it is difficult to determine how these cytokines will further influence the microenvironment and the RT wound healing response without further investigation. To develop co-cultures with more biological relevance, complexity and heterogeneity, the following steps must be utilized. First, CD8<sup>+</sup> T cells and normal tissue cells must be MHC matched, making it possible for fibroblasts to present self-peptides to CD8<sup>+</sup> T cells. Additionally, fibroblasts must be

evaluated for their capability of expressing co-stimulatory factors. Wounded fibroblasts have been shown to express CD40, which is crucial for CD8<sup>+</sup> T cell differentiation into memory cells<sup>54,163</sup>. The absence of co-stimulatory factors may prevent CD8<sup>+</sup> T cells from developing a complete response and could be significantly influencing *in vitro* observations. Finally, additional T cell phenotypes must be incorporated into co-cultures. The timing and proportions of these cells are something that must be optimized and corroborated in conjunction with *in vivo* data.

#### **4.4.7 CD8<sup>+</sup> T cell mediated tissue damage resolution downregulates macrophage recruitment to irradiated sites**

To further determine how stromal-CD8<sup>+</sup> T cell interactions can indirectly affect macrophage behavior, we evaluated macrophage invasive capacity toward secreted factors from fibroblast-organoid co-cultures. Macrophages were plated in a Matrigel coated Boyden chamber and migrated toward conditioned media. We observed that secreted factors from “immunocompromised” irradiated organoids facilitated macrophage invasion at over a five-fold rate relative to factors from “immunocompetent” irradiated organoids (**Figure 4.9**). This data reinforces that without CD8<sup>+</sup> T cells present at the site of irradiation damage, excessive macrophage infiltration will occur, recapitulating *in vivo* observations of macrophage recruitment in CD8<sup>-</sup> mouse models<sup>193</sup>.

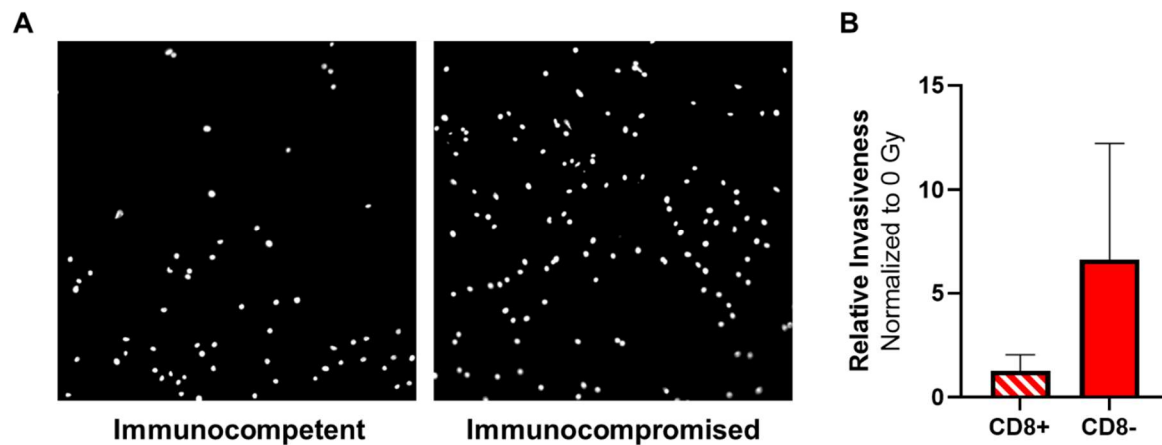


**Figure 4.9. Macrophage invasion as a function of RT and immunocompetency.**

**A.** Representative images and **B.** Quantification for invasiveness of macrophages toward conditioned media collected from organoid co-cultures 2 days post-RT. All values are normalized relative to the unirradiated condition matching immune status. Data is mean  $\pm$  SEM, N = 3 biological replicates.

## 4.5 Conclusions and Future Work

Taken together, this data suggests that in tissue wounded from RT, stromal-CD8<sup>+</sup> T cell interactions are a necessary part of the wound healing process. When CD8<sup>+</sup> T cells are absent, the wound healing process post-RT is altered, resulting in excess secretion of cytokines that recruit myeloid cells. This work further highlights the importance of using three-dimensional models to study the effects of radiation damage of normal tissue.

Despite these interesting findings, further investigation is required. First, more in-depth characterization of changes in genotype due to unresolved irradiation damage is required. Additionally, more robust characterization of changes in the secretome in co-culture models at short, mid, and long term time points after RT would provide more knowledge on specific cytokines that may be most involved in facilitating macrophage recruitment.

MHC class I molecules are expressed on the surface of all cells. These molecules present fragments of peptides derived from intracellular proteins<sup>100</sup>. This is the primary way in which CD8<sup>+</sup> T cells and cells directly communicate. Co-stimulatory molecules like CD28 and PD-1 can amplify or downregulate the initial activation of T cells, influencing T cell fate<sup>152</sup>. While it is known that irradiation can induce the presentation of immunogenic self-peptides, the types of peptides and the way they influence the CD8<sup>+</sup> T cell response is unknown. Therefore, it would be necessary to conduct experiments to characterize changes in presentation of self-peptides and subsequent CD8<sup>+</sup> T cell phenotypes. This could be accomplished utilizing *in vivo* systems first. The immunocompetent tumor cell recruitment *in vivo* model would be utilized, with mice receiving irradiation at the mammary gland contralateral from the tumor. 1, 5, and 10 days after irradiation, irradiated mammary fat pads would be isolated. The immune cells could be sorted out from the non-immune cells via magnetic activated cell sorting (MACS). CD8<sup>+</sup> T cell cytotoxicity

and phenotype would be characterized via granzyme, perforin, and interferon  $\gamma$  activity via flow cytometry<sup>84</sup>. Changes in stromal (CD45-) immune cell peptide presentation could be characterized via immunopeptidomics<sup>85,195</sup>. In this technique, mass spectrometry is used to identify and quantify MHC-I associated peptides<sup>37</sup>. This could identify specific peptides induced by radiation that are involved in eliciting an immunogenic response from CD8+ T cells.

Further characterization of CD4+ T cell phenotype and behavior *in vivo* is required as well. Although evaluating CD4+ T cell phenotypes and incorporating them into our models was outside the scope of the work, they remain extremely important to influencing CD8+ T cell response, promoting DC-CD8+ T cell interactions, supporting maintenance of effector T cells, and inducing memory CD8+ T cells<sup>131</sup>. There has been extensive characterization of how CD4+ T cells influence CD8+ T cell phenotype in the literature; however, it would be interesting to characterize changes in CD4+ T cells in a microenvironment lacking CD8+ T cells. These experiments could be easily carried out *in vivo*, characterizing CD4+ T cell infiltrates 1, 5, and 10 days post-RT in CD8+ and CD8- mice. CD4+ T cell subsets could be characterized by looking at expression of markers IL-12 (Th1), IL-4 (Th2), IL-17 (Th17), and IL-10 (Treg)<sup>84</sup>.

## Chapter 5

### CONCLUSIONS AND FUTURE WORK

#### 5.1 Conclusions

In this dissertation I have discussed various methods of more accurate *in vitro* models of irradiation induced recurrence. Mammary organoid models can be utilized as a robust model to complement *in vivo* studies. Using these models, we have been able to further determine mechanisms of recurrence by modeling and characterizing normal tissue microenvironments with co-cultures, cytokine profiling, live cell imaging, and various *in vitro* assays with TNBC cells.

##### 5.1.1 Irradiated Mammary Epithelial Organoids

In the first chapter, I reviewed the literature surrounding organoids, radiation research, and co-cultures with immune cells. There are many exciting advances in organoid research for advancing understanding of basic biological processes, modeling metastasis, and drug screening, there is still very limited work that has utilized a three-dimensional model to study the effects of irradiation of normal tissue.

With advances in organoid techniques comes additional challenges. As irradiation-motivated organoid and spheroid studies progress, researchers need to take steps to prioritize consideration of reproducibility, scale, and biological relevance. I argue that researchers will benefit from maximizing transparency with their setup and analytical techniques. Only then will these models gain the ubiquity currently seen by monolayer cell culture.

An additional comment that I made was that regarding biological relevance. With co-culture studies, the number of cell lines chosen, the type, and proportion can all drastically influence results. Therefore, decisions about heterogeneous cell cultures must be made with sound scientific and biological reasoning. For researchers unsure how to go about this, a combination of literature and observations from *in vivo* characterizations are good places to start. As mentioned previously, justifications for all these decisions must be made readily transparent.

I then built off this literature review and to develop a three-dimensional low-adhesion organoid model, described in chapter 2. In these studies, I have developed co-culture and imaging techniques to glean interesting insights that can be applied to further *in vivo* studies. Importantly, I have isolated and begun to characterize the how irradiated breast epithelium contribute to recurrence. In the future, these techniques can be easily applied to patient derived samples, utilizing primary macrophages and MDA-MB-231 and other human based cancer cell lines.

### **5.1.2 Irradiated mammary fibroblast organoids**

In the third chapter, I develop an immunocompromised co-culture organoid model that is easily scalable. To make this model realistic, I incorporated macrophages and 4T1s at proportions observed *in vivo*. Typically, this depth of reasoning is not used in other co-culture models, as researchers tend choose somewhat arbitrary proportions of cells within their model microenvironment. My study was therefore among the first to use this justification in selecting different ratios of fibroblasts, M0, M1, and M2 macrophages in modeling an irradiated microenvironment. This rationale and attention to maintaining relevant heterogenous cell populations proved to have substantial implications, as including relevant macrophage ratios

resulted in elevated secretion of IL-6, something not observed when M0 macrophages alone were used.

In this model, we showed that IL-6 secreted from macrophage-stromal interactions served as a chemoattractant for TNBC cells *in vitro*. We also showed that systemic depletion of IL-6 resulted in a significant decrease in tumor cell recruitment to irradiated sites *in vivo*. We were therefore the first to link IL-6 to TNBC recurrence post-RT. Future work for this project may entail employing other pharmaceutically approved IL-6 inhibitors as a potential therapeutic to prevent recurrence *in vivo*.

### **5.1.3 Immunocompetent irradiated mammary fibroblast organoids**

In the fourth chapter, I outline the development of an immunocompetent organoid model. I did this by engineering a fibroblast- CD8<sup>+</sup> T cell co-culture model utilizing primary murine CD8<sup>+</sup> T cells. I showed that CD8<sup>+</sup> T cells infiltrate into organoids within a few hours of co-culture. From these co-culture studies, I determined that CD8<sup>+</sup> T cell – stromal interactions facilitate the wound healing response in the irradiated microenvironment. We are the first to develop organoids that can model various stages of immunocompetence to study the effects of the immune system on post-RT wound healing.

## **5.2 Future Directions**

### **5.2.1 IL-6 inhibitors**

In the clinic, IL-6 inhibitors have been primarily used to study various rheumatic diseases, including rheumatoid arthritis, adult onset Still's disease, and juvenile idiopathic arthritis<sup>48</sup>. A

summary of these therapies can be found in **Table 5.1**. Tocilizumab was developed in the early 2000's by Chogai, a subsidiary of Roche. Tocilizumab is an antibody that binds to the IL-6 receptor and prevents IL-6 signaling by inhibiting binding of IL-6 to IL-6R. IL-6 treatments like tocilizumab and siltuximab have been largely successful at improving outcomes for patients with these autoimmune diseases.

IL-6 treatment has also been used as a method of treating cytokine release syndrome (CRS) associated with chimeric antigen receptor (CAR-) T cell treatments in both children and adults. CAR T cells are T cells modified *ex vivo* to respond to tumor antigen. CAR-T cell treatment is typically used to treat hematological cancers, including B-cell lymphoblastic leukemia, and various T-cell engaging therapies are being studied for treatment of multiple myeloma and acute myeloid leukemia<sup>97</sup>. Unfortunately, up to 70% of patients treated with CAR-T cells experience CRS, which is an overactivation of the immune system marked by a sustained increase in inflammatory cytokines in circulation and in tissues, leading to organ failure and in some cases death<sup>97</sup>. Tocilizumab has been approved for treatment of CAR-T cell induced CRS.

In cancer, IL-6 inhibitors have been largely unsuccessful at preventing progression of primary disease, showing little efficacy in multiple myeloma, renal cell carcinoma, and prostate cancer<sup>200</sup>. In a pre-clinical TNBC model, inhibition of IL-6R has been shown to hinder metastasis<sup>252</sup>. However, there is limited knowledge of the clinical efficacy of IL-6 and IL-6R inhibitors in primary breast cancer recurrence<sup>99</sup>.

While anti-IL-6 agents have been studied and shown to be mostly unsuccessful at preventing primary tumor progression and metastasis, their role in recurrence has not been studied. Our work shows that TNBC patients vulnerable to recurrence may benefit from therapies inhibiting IL-6. Patient IL-6 serum levels could be monitored, similar to how patients with auto-immune

diseases have their biomarkers defined. This work and potential therapy could also be relevant to other breast cancers with high rates of recurrence, including HER2-positive BC<sup>146</sup>, and cancers of other organs with high recurrence rates, like head and neck cancer<sup>213</sup>.

**Table 5.1. IL-6 targeting agents in clinical trials as anti-cancer therapeutics. Adapted from**

48

| Disease                                | Cell-based assays  | Animal models   | Biomarkers  | Clinical trials  | Drugs indicated         |
|--|--|---|---|--|-------------------------|
| Multiple myeloma                       | IL-6 promotes myeloma cell proliferation   | In the KPMM2 xenograft model, growth is IL-6 dependent  | Serum concentrations of IL-6 correlate with disease severity in plasma cell leukaemia   | No improvement in clinical outcomes  | None                    |
| Crohn's disease                        | IL-6 activates mucosal T cells   | IL-6R blockade promotes T cell apoptosis, which contributes to chronic intestinal inflammation in the CD4 adoptive transfer colitis model | Serum concentrations of sIL-6R are increased in active disease; concentrations of IL-6 and sIL-6R are increased in colonic organ cultures using specimens from patients with active disease | Tocilizumab had a clinical effect in a pilot study   | None                    |
| Castleman disease                      | IL-6 is produced by affected germinal centres  | IL6 transgenic mice develop clinical features of Castleman disease  | Increased serum concentrations of IL-6 in active disease  | Tocilizumab and siltuximab showed efficacy in clinical studies   | Tocilizumab, siltuximab |
| Rheumatoid Arthritis                   | IL-6 is involved in osteoporosis, cartilage destruction and synovial inflammation associated with RA | IL-6 inhibition prevented development of arthritis in collagen-induced arthritis and antibody-induced arthritis                           | Serum concentrations of IL-6 are elevated in active RA  | IL-6 pathway inhibition is effective in many clinical trials   | Tocilizumab, sarilumab  |
| Systemic Juvenile Idiopathic Arthritis | Increased production of IL-6 by PBMCs  | IL6 transgenic mice develop a skeletal phenotype resembling abnormalities observed in children with chronic inflammatory diseases         | Serum concentrations of IL-6 are increased in patients with JIA and correlate with disease activity   | Tocilizumab improved disease activity and reversed growth retardation  | Tocilizumab             |
| Adult-onset Still's disease            | NA   | NA  | Serum concentrations of IL-6 are increased  | Tocilizumab showed some clinical benefit and steroid-sparing effects   | Tocilizumab             |
| Ankylosing spondylitis                 | NA   | NA  | Serum concentrations of IL-6 are increased and correlate with disease activity  | Tocilizumab and sarilumab failed to show therapeutic benefit in randomized controlled trials                     | None                    |
| Psoriatic arthritis                    | NA   | NA  | Serum and synovial fluid concentrations of IL-6 are increased   | Clazakizumab improved arthritis, enthesitis and dactylitis but not skin disease                                  | None                    |
| Systemic lupus erythematosus           | Increased production of IL-6 by B cells  | IL-6 implicated in autoimmune disease pathogenesis in NZB/W F1 mice   | IL-6 concentrations increased in cerebrospinal fluid  | IL-6 pathway inhibition affected autoantibody-producing cells, but no clinically meaningful benefit demonstrated | None                    |
| Systemic sclerosis                     | Increased production of IL-6 by PBMCs  | IL-6 blockade improved disease in the bleomycin mouse model   | Production of IL-6 increased in dermal fibroblasts and serum concentrations of IL-6 increased   | Tocilizumab had a potentially clinically important effect on the preservation of lung function                   | None                    |
| Giant cell arteritis                   | NA   | NA  | Serum concentrations of IL-6 increased in active disease  | Tocilizumab was superior to placebo with regard to sustained glucocorticoid-free remission                       | Tocilizumab             |
| Takayasu arteritis                     | NA   | NA  | Serum concentrations of IL-6 increased in active disease  | Tocilizumab had some effect on time to relapse, but the primary end point was not met                            | Tocilizumab             |
| Cytokine Release Syndrome              | NA   | NA  | Serum concentrations of IL-6 increased  | Tocilizumab was used to successfully treat CRS occurring in trials of CAR T cell therapy                         | Tocilizumab             |

### 5.2.2 Macrophage reprogramming therapeutics

Because of the prevalence of macrophages within the tumor microenvironment, techniques to reprogram macrophages away from a tumor associated phenotype have been explored in a variety of cancers (**Table 5.2**). A variety of vectors for delivering therapeutics have been studied, including viral vectors, antibodies, nanoparticles, small molecule inhibitors and cytokines, and adoptive transfer of *ex vivo* stimulated bone marrow derived macrophages<sup>22</sup>.

A variety of targets, stimuli, and pathways have been studied to target tumor associated macrophages (TAM) and repolarize TAM associated phenotypes. Researchers have developed vaccines to induce a CD8+ T cell response against TAMs, which reduced pro-angiogenic cytokine secretion and suppressed tumor growth<sup>148</sup>. Aside from interfering with TAM survival, other approaches have been taken to target TAMs. Qian et al. showed that tumors attract TAMs with the chemokine CCL2. This in turn creates a positive feedback loop, where macrophages attract more tumor cells. Qian et al. used anti-CCL2 antibodies to prevent macrophage recruitment, significantly ablating tumor growth and metastasis in humanized TNBC murine models<sup>191</sup>. Furthermore, in multiple *in vitro* models, Duluc et al. showed that treating TAMs with IFN- $\gamma$  reduced secretion of immunosuppressive cytokines from TAMs and reprogrammed them to have an M1 associated phenotype<sup>66</sup>.

On macrophages, the CSFR receptor interactions with ligands associated with cell proliferation and survival, making CSFR an attractive therapeutic target. In an *in vivo* mouse glioblastoma model, Pyonteck et al. used BLZ945, a CSFR inhibitor, to increase mouse survival time by reprogramming the microenvironment away from a TAM phenotype<sup>190</sup>. The authors determined that gene expression in 4 out of 5 genes associated with an M2 macrophage phenotype

were significantly reduced. M-CSFR has also been studied as a therapeutic target in multiple clinical studies of glioblastoma, prostate cancer, and breast cancer<sup>22</sup>.

Toll like receptors (TLR) facilitate immune cell surveillance, and their stimulation by agonists facilitates an immunogenic response<sup>120</sup>. Activation of TLR7 can induce a type 1 interferon immune response, making it a target of interest when aiming to elevate anti-tumor immunity. Therapeutic development and testing to stimulate macrophage expressed TLR7 has been explored extensively clinically in breast cancer<sup>22</sup>.

An additional receptor that has been targeted is CD40, which is a costimulatory receptor expressed on the surface of macrophages and other myeloid cells<sup>243</sup>. Ligation of CD40 induces maturation and activation of antigen presenting cells, which can stimulate Type 1 CD4+ and CD8+ T cells<sup>260</sup>. Clinical trials have examined targeting CD40 in pancreatic cancer<sup>22</sup>.

Multiple receptors on macrophages have been studied as potential therapeutic targets in pre-clinical and clinical studies for various cancers. However, they have not been studied to reduce TNBC recurrence. Macrophage reprogramming could be utilized for patients receiving radiation and surgery. Certain care and considerations must be considered when skewing macrophages toward a different phenotype, as it has the potential to significantly alter the microenvironment. Radiation damage to normal tissue initiates a wound healing process. The interactions and contributions from M1- and M2-macrophages are all part of a tightly controlled process that requires both upregulation and downregulation of inflammation at various timepoints. Significantly altering the cell makeup in this microenvironment could lead to incomplete tissue repair, fibrosis, and potential further organ damage. Therefore, extensive *in vitro* and *in vivo* characterization of any drug, biomaterial, or other targeted therapeutic must be performed to ensure that inflammation is adequately resolved.

**Table 5.2. Select clinical studies of macrophage reprogramming compounds. Adapted from**

22

| Compound                                     | Target                     | Clinical phase | Clinicaltrials.gov identifier | Status   | Results  | Type of malignancy                                      |
|--|----------------------------|----------------|-------------------------------|----------|--|---|
| Imiquimod                                    | TLR7                       | Phase II       | NCT00031759                   | Complete | No impact on recurrence of cervical dysplasia  | Cervical cancer   |
| 852A   | TLR7                       | Phase I        | NCT00095160                   | Complete | No results available   | Refractory solid organ tumours                          |
| 852A   | TLR7                       | Phase II       | NCT00189332                   | Complete | No results available   | Metastatic cutaneous melanoma                           |
| 852A   | TLR7                       | Phase II       | NCT00319748                   | Complete | Evidence of immune activation as evaluated by cytokine production                                      | Breast, ovarian, endometrial and cervical cancers       |
| CD40 mAb CP-870,893 and chemotherapy         | CD40                       | Phase I        | NCT00711191                   | Complete | Partial response in 4/21 patients, stable diseases in 11/21 patients                                   | Advanced cancer of the pancreas                         |
| Imo-2055                                     | TLR9                       | Phase II       | NCT00729053                   | Complete | Treatment-emergent adverse events observed in > 90% of patients  | Renal cell carcinoma                                    |
| Imiquimod together with Abraxane             | TLR7                       | Phase II       | NCT00821964                   | Complete | Pathologic clinical response in 71.4% of patients  | Advanced breast cancer                                  |
| Imiquimod                                    | TLR7                       | Phase III      | NCT00941252                   | Complete | Histologic regression in 73% of patients   | Cervical intraepithelial neoplasia                      |
| Imiquimod                                    | TLR7                       | Phase IV       | NCT01161888                   | Complete | No results available   | Lentigo malignant of the face                           |
| Imiquimod, cyclophosphamide and radiotherapy | TLR7                       | Phase II       | NCT01421017                   | Complete | No results available   | Skin metastasis in breast cancer                        |
| CD40 mAb CP-870,893 and gemcitabine          | CD40                       | Phase I        | NCT01456585                   | Complete | No results available   | Pancreatic ductal adenocarcinoma                        |
| Resiquimod                                   | TLR7/8                     | Phase I/II     | NCT01676831                   | Complete | Significant improvements of treated lesions in 75% of patients, clearing of all treated lesions in 30% | Cutaneous T-cell lymphoma                               |
| PLX3397                                      | M-CSFR (+ cKit, Flt3)      | Phase Ib/II    | NCT01790503                   | Complete | Stable disease in 24/50 patients, complete response in 2/50, partial response in 5/50 patients         | Glioblastoma  |
| PLX3397 + radiation therapy                  | M-CSFR (+ cKit, Flt3)      | Phase Ib/II    | NCT01790503                   | Complete | Stable disease in 24/50 patients, complete response in 2/50, partial response in 5/50 patients         | Glioblastoma  |
| PLX3397 + temozolomide                       | M-CSFR (+ cKit, Flt3)      | Phase Ib/II    | NCT01790503                   | Complete | Stable disease in 24/50 patients, complete response in 2/50, partial response in 5/50 patients         | Glioblastoma  |
| CD40 mAb CP-870,893                          | CD40                       | Phase I        | NCT02225002                   | Complete | No results available   | Advanced solid tumours                                  |
| LY3022855                                    | M-CSFR                     | Phase I        | NCT02265536                   | Complete | Stable disease in 5/22 MBC and 3/7 MCRPC patients  | Metastatic breast cancer (MBC)                          |
| LY3022855                                    | M-CSFR                     | Phase I        | NCT02265536                   | Complete | Stable disease in 5/22 MBC and 3/7 MCRPC patients  | Metastatic castration-resistant prostate cancer (MCRPC) |
| MCS110 with carboplatin and gemcitabine      | M-CSF                      | Phase II       | NCT02435680                   | Complete | No results available   | Advanced triple negative breast cancer with high TAMs   |
| MCS110 with PDR001                           | M-CSFR (+/- PD-1 blockade) | Phase Ib/II    | NCT02807844                   | Complete | Partial response in 1/48, stable disease in 9/48 patients  | Advanced malignancies                                   |

### 5.2.3 Controlling Normal Tissue Radiation Damage with Radioprotectants and Modified Dosing Regimes

The standard of care for over 70% of TNBC patients includes ionizing radiation therapy, which does not spare normal tissue. Any method of reducing RT induced normal tissue damage is desirable as it allows for a dose escalation, improving overall outcomes and decreasing the likelihood of recurrence<sup>167</sup>. Radioprotectors are agents designed to reduce the cytotoxic effects of ionizing radiation. Radioprotectants have been studied for applications ranging from protecting biological systems from accidental radiation release to protecting normal cells that exposed to radiation as a part of cancer radiotherapy treatment. A variety of radioprotective agents have been published in both *in vitro* and *in vivo* systems (**Table 5.3**). These agents act to reduce radiation damage in a variety of ways, including minimizing DNA damage, increasing free radical scavenging activity, and decreasing lipid peroxidation<sup>226</sup>.

Organs commonly associated with radiotherapy toxicities include the brain, reproductive organs, pituitary gland, and GI tract<sup>202</sup>. Conversely, acute radiation damage to normal mammary tissue is known to generally be well tolerated, and the most common challenges associated with radiotherapy toxicity occur in other organs, like the heart and lungs<sup>202</sup>. Therefore, there has been very little research examining how the influence of radioprotectants on the wound healing response post-RT in normal mammary tissue. Because of the high recurrence rates associated with TNBC post-RT, it may be an interesting area to explore. 3-dimensional *in vitro* models of normal tissue could be a useful starting point to see how different radioprotectants influence the wound healing response. It would be relatively straightforward to analyze how treatment influences the wound healing response by investigating markers that are commonly altered after radiation damage, like cell proliferation, cellular senescence, lipid peroxidation, and changes in cytokine secretion.

There are other factors that could help alleviate radiotherapy toxicities. Radiation doses have typically been applied at a rate of 2-3 Gy/min. FLASH-RT involves the delivery of radiation at dose rates orders of magnitudes higher than traditional rates, exceeding rates of 100 Gy/s<sup>167</sup>. Higher delivery rates of radiation have been shown to have a radioprotective effect on normal tissues while still maintaining anti-tumor effects<sup>30,167,168</sup>. Although normal mammary tissue radiation damage is generally well tolerated, high recurrence rates in TNBC may motivate the need to explore the efficacy of enhanced dosage delivery rates on lowering rates of locoregional failure.

**Table 5.3. List of Radioprotective Agents and Their Mechanism of Action. Adapted from <sup>117</sup>.**

| List of radioprotectors/mitigators   | Radioprotective effect and mechanism of action   |
|--|--|
| Cytoprotective agents approved by FDA: mesna, dexrazoxane, amifostine  | Reduced toxicity of chemo-therapeutic drugs, decreased urothelial toxicity and nephrotoxicity  |
| Plant extracts and single active components from plants  | Reduction of primary and secondary ROS, antioxidant effect; reduced DNA damage   |
| Antioxidants: Vitamin A, C, and E, melatonin, tempce   | Free radical scavenging, inhibition of chromosomal aberrations and creation of micronuclei in lymphocytes  |
| Selenium compounds: seleno methionine, sodium selenite   | Preventing mutagenic changes induced by IR   |
| Nitroxides: tempol, tempol-H, tempce, troxyl   | Superoxide dismutase mimics, free-radical scavenging   |
| DNA-binding ligands: bis-benzimidazoles, hoechst 33342, DMA  | Electron transfer, free-radical scavenging   |
| Fullerenes: fullereneol C <sub>60</sub> (OH) <sub>24</sub>   | Free-radical scavenging in biological systems  |
| HMG-CoA reductase inhibitors (statins): lovastatin, simvastatin, pravastatin   | Mitigation of radiation enteropathy, pulmonary fibrosis  |
| Lipopolysaccharides and prostaglandins: misoprostol  | Prostaglandin synthesis, DNA repair, elevated levels of cyclic AMP   |
| Chelators: diethylenetriaminepentaacetate (DTPA)   | Chelating with transuranium radionuclides (Pu, Am, Cm)   |
| Sulfhydryl compounds: cysteine, cysteamine, glutathione, aminoethyl-isothiourea, amifostine, and other WR compounds                | Free-radical scavenging, donation of H-atom, hypoxia in cells and tissues  |
| Metallo elements and metallo-thionine, bismuth subnitrate and manganese chloride   | Protection of hematopoietic system from lethal effects of IR, induction of metallothionine synthesis in bone marrow cells  |
| Potassium iodide (KI)  | Protective measure to reduce thyroid radioiodine uptake  |
| ACE inhibitors: captopril, enalapril, ramipril, perindopril and ACE receptor antagonist: penicillamine, pentoxifylline             | Inhibition of angiotensin II production, suppression of proliferation, prevention of development of radiation- induced late effects (kidney and lung damages), suppression of chronic oxidative stress |
| Ca-antagonist and Zn salts: synergistic combinations (diltiazem, nifedipine, nitrendipine, nimodipine) and Zn salts (Zn aspartate) | Inhibition of calcium influx through plasma membrane   |
| Immunomodulators: $\gamma$ -interferon, polysaccharides AM218, AM5   | Increased production of cytokines, immune stimulation  |
| Steroids and hormones: 5-androstendiol, oxymetholone, melanin  | Myelopoiesis stimulation and enhancement of circulating neutrophil and platelet numbers  |

## REFERENCES

1. Acerbi, I. *et al.* Human breast cancer invasion and aggression correlates with ECM stiffening and immune cell infiltration. *Integr. Biol. (United Kingdom)* 7:1120–1134, 2015.
2. Adkins, F.C. *et al.* Triple-negative breast cancer is not a contraindication for breast conservation. *Ann. Surg. Oncol.* 18:3164–3173, 2011.
3. Adra, J. *et al.* Distribution of Locoregional Breast Cancer Recurrence in Relation to Postoperative Radiation Fields and Biological Subtypes. *Int. J. Radiat. Oncol.* 105:285–295, 2019.
4. Afghahi, A. *et al.* Higher absolute lymphocyte counts predict lower mortality from early-stage triple-negative breast cancer. *Clin. Cancer Res.* 24:2851–2858, 2018.
5. Aghajanian, H. *et al.* Targeting cardiac fibrosis with engineered T cells. *Nature* 573:430–433, 2019.
6. Ahn, G.O., and J.M. Brown. Matrix metalloproteinase-9 Is required for tumor vasculogenesis but not for angiogenesis: role of bone marrow-derived myelomonocytic cells. *Cancer Cell* 13:193–205, 2008.
7. Al-Mahmood, S., J. Sapiezynski, O.B. Garbuzenko, and T. Minko. Metastatic and triple-negative breast cancer: challenges and treatment options. *Drug Deliv. Transl. Res.* 8:1483–1507, 2018.
8. Alcaraz, J. *et al.* Laminin and biomimetic extracellular elasticity enhance functional differentiation in mammary epithelia. *EMBO J.* 27:2829–2838, 2008.
9. Alessandri, K., B. Ranjan, V. Valériévitch, and B. Sinha. Cellular capsules as a tool for multicellular spheroid production and for investigating the mechanics of tumor progression in

vitro. *Proc. Natl. Acad. Sci.* 110:14843–14848, 2013.

10. Ambroggi, M. *et al.* Metastatic breast cancer to the gastrointestinal tract: report of five cases and review of the literature. *Int. J. Breast Cancer* 2012:1–8, 2012.

11. Andarawewa, K.L. *et al.* Ionizing radiation predisposes nonmalignant human mammary epithelial cells to undergo transforming growth factor  $\beta$ -induced epithelial to mesenchymal transition. *Cancer Res.* 67:8662–8670, 2007.

12. Avivar-Valderas, A. *et al.* Functional significance of co-occurring mutations in PIK3CA and MAP3K1 in breast cancer. *Oncotarget* 9:21444–21458, 2018.

13. Ayuso, J.M. *et al.* Organotypic microfluidic breast cancer model reveals starvation-induced spatial-temporal metabolic adaptations. *EBioMedicine* 37:144–157, 2018.

14. Bagley, J.A., D. Reumann, S. Bian, J. Lévi-Strauss, and J.A. Knoblich. Fused cerebral organoids model interactions between brain regions. *Nat. Methods* 14:743–751, 2017.

15. Bakal, C., G. Church, and N. Perrimon. Regulating Cell Morphology. *Science* (80-. ). 316:1753–1756, 2007.

16. Baker, D.G., and R.J. Krochak. The response of the microvascular system to radiation: A review. *Cancer Invest.* 7:287–294, 1989.

17. Balermipas, P. *et al.* Head and neck cancer relapse after chemoradiotherapy correlates with CD163+ macrophages in primary tumour and CD11b+ myeloid cells in recurrences. *Br. J. Cancer* 111:1509–1518, 2014.

18. Barcellos-Hoff, M., R. Derynck, M.-S. Tsang, and J. Weatherbee. Transforming growth factor- $\beta$  activation in irradiated murine mammary gland. *J Clin Invest.* 92:2065–2072, 1993.

19. Barcellos-Hoff, M.H. Radiation-induced transforming growth factor beta and subsequent extracellular matrix reorganization in murine mammary gland. *Cancer Res* 53:3880–3886, 1993. Available from: [http://www.ncbi.nlm.nih.gov/entrez/query.fcgi?cmd=Retrieve&db=PubMed&dopt=Citation&list\\_uids=8358713](http://www.ncbi.nlm.nih.gov/entrez/query.fcgi?cmd=Retrieve&db=PubMed&dopt=Citation&list_uids=8358713).
20. Barcellos-Hoff, M.H., and S.A. Ravani. Irradiated mammary gland stroma promotes the expression of tumorigenic potential by unirradiated epithelial cells. *Cancer Res.* 60:1254–1260, 2000.
21. Barreto-Andrade, J.C. *et al.* Response of Human Prostate Cancer Cells and Tumors to Combining PARP Inhibition with Ionizing Radiation. *Mol. Cancer Ther.* 10:1185–1193, 2011.
22. Bart, V.M.T., R.J. Pickering, and P.R. Taylor. Macrophage reprogramming for therapy. *Immunology* 128–144, 2021.
23. Benesch, M.G. *et al.* Tumor-induced inflammation in mammary adipose tissue stimulates a vicious cycle of autotaxin expression and breast cancer progression. *FASEB J* 29:3990–4000, 2015.
24. Bertozzi, S. *et al.* Prevalence, risk factors, and prognosis of peritoneal metastasis from breast cancer. *Springerplus* 4:1–8, 2015.
25. Bierie, B., and H.L. Moses. Tumour microenvironment - TGFB: The molecular Jekyll and Hyde of cancer. *Nat. Rev. Cancer* 6:506–520, 2006.
26. Bochet, L., A. Meulle, S. Imbert, B. Salles, P. Valet, and C. Muller. Cancer-associated adipocytes promotes breast tumor radioresistance. *Biochem. Biophys. Res. Commun.* 411:102–

106, 2011.

27. Bond, M.D., and H.E. Van Wart. Characterization of the Individual Collagenases from *Clostridium histolyticum*. *Biochemistry* 23:3085–3091, 1984.

28. Borten, M.A., S.S. Bajikar, N. Sasaki, H. Clevers, and K.A. Janes. Automated brightfield morphometry of 3D organoid populations by OrganoSeg. *Sci. Rep.* 8:1–10, 2018.

29. Bouaouiche, S. *et al.* Nitric Oxide-Releasing Drug Glyceryl Trinitrate Targets JAK2 / STAT3 Signaling , Migration and Invasion of Triple-Negative Breast Cancer Cells. *Int. J. Mol. Sci.* 22, 2021.

30. Bourhis, J. *et al.* Treatment of a first patient with FLASH-radiotherapy. *Radiother. Oncol.* 139:18–22, 2019. Available from: <https://doi.org/10.1016/j.radonc.2019.06.019>.

31. Boutin, M.E., T.C. Voss, S.A. Titus, K. Cruz-Gutierrez, S. Michael, and M. Ferrer. A high-throughput imaging and nuclear segmentation analysis protocol for cleared 3D culture models. *Sci. Rep.* 8:1–14, 2018.

32. Brown, J.M., and J.C. Probert. Long-term recovery of connective tissue after irradiation. *Radiology* 108:205–207, 1973.

33. Brown, P.D. *et al.* Memantine for the prevention of cognitive dysfunction in patients receiving whole-brain radiotherapy: a randomized, double-blind, placebo-controlled trial. *Neuro. Oncol.* 15:1429–1437, 2013.

34. Buxadé, M. *et al.* Macrophage-specific MHC II expression is regulated by a remote Ciita enhancer controlled by NFAT5. *J. Exp. Med.* 215:2901–2918, 2018.

35. Campbell, J.J., L.A. Botos, T.J. Sargeant, N. Davidenko, R.E. Cameron, and C.J. Watson. A

- 3-D in vitro co-culture model of mammary gland involution. *Integr. Biol. (United Kingdom)* 6:618–626, 2014.
36. Camphausen, K. *et al.* Radiation abscopal antitumor effect is mediated through p53. *Cancer Res.* 63:1990–1993, 2003.
37. Caron, E., D.J. Kowalewski, C.C. Koh, T. Sturm, H. Schuster, and R. Aebbersold. Analysis of Major Histocompatibility Complex ( MHC ) Immunopeptidomes Using Mass Spectrometry \*. 3105–3117, 2015.
38. Carpenter, K.J. *et al.* LXR-inverse agonism stimulates immune-mediated tumor destruction by enhancing CD8 T-cell activity in triple negative breast cancer. *Sci. Rep.* Springer US, 1–18, 2019. Available from: <http://dx.doi.org/10.1038/s41598-019-56038-1>.
39. Casella, G. *et al.* IL4 induces IL6-producing M2 macrophages associated to inhibition of neuroinflammation in vitro and in vivo. *J. Neuroinflammation* Journal of Neuroinflammation, 13:1–10, 2016.
40. Casey, J. *et al.* 3D hydrogel-based microwell arrays as a tumor microenvironment model to study breast cancer growth. *Biomed. Mater.* 12:1–12, 2017.
41. Centenera, M.M. *et al.* A patient-derived explant (PDE) model of hormone-dependent cancer. *Mol. Oncol.* 12:1608–0622, 2018.
42. Chanson, L. *et al.* Self-organization is a dynamic and lineage-intrinsic property of mammary epithelial cells. *Proc. Natl. Acad. Sci.* 14:2293–2306, 2011.
43. Chatterjee, S., P. Basak, E. Buchel, L.C. Murphy, and A. Raouf. A robust cell culture system for large scale feeder cell-free expansion of human breast epithelial progenitors. *Stem Cell Res.*

*Ther.* 9:1–10, 2018.

44. Chen, C.S., M. Mrksich, S. Huang, G.M. Whitesides, and D.E. Ingber. Geometric control of cell life and death. *Science (80-. )*. 276:1425–1428, 1997.

45. Chen, Y., Y. Song, W. Du, L. Gong, H. Chang, and Z. Zou. Tumor-associated macrophages: an accomplice in solid tumor progression. *J. Biomed. Sci. Journal of Biomedical Science*, 26:1–13, 2019.

46. Chida, S., K. Okada, N. Suzuki, C. Komori, and Y. Shimada. Infiltration by macrophages and lymphocytes in transplantable mouse sarcoma after irradiation with high-intensity focused ultrasound. *Anticancer Res.* 29:3877–3882, 2009.

47. Cho, O., Y. Oh, M. Chun, O. Noh, J. Hoe, and H. Kim. Minimum absolute lymphocyte count during radiotherapy as a new prognostic factor for nasopharyngeal cancer. *Head Neck* 1061–1067, 2016.

48. Choy, E.H., M.R. John, and T. Kishimoto. Translating IL-6 biology into effective treatments. *Nat. Rev. Rheumatol.* Springer US, 16:335–345, 2020. Available from: <http://dx.doi.org/10.1038/s41584-020-0419-z>.

49. Chua, A.C.L., L.J. Hodson, L.M. Moldenhauer, S.A. Robertson, and W. V Ingman. Dual roles for macrophages in ovarian cycle-associated development and remodelling of the mammary gland epithelium. *Development* 137:4229–4238, 2010.

50. Clevers, H. The intestinal crypt, a prototype stem cell compartment. *Cell* 154:274–284, 2013.

51. Cline, J. *et al.* Post-Irradiation Treatment with a Superoxide Dismutase Mimic, MnTnHex-2-PyP5+, Mitigates Radiation Injury in the Lungs of Non-Human Primates after Whole-Thorax

Exposure to Ionizing Radiation. *Antioxidants* 7:1–17, 2018.

52. Cockburn, K. *et al.* Gradual differentiation uncoupled from cell cycle exit generates heterogeneity in the epidermal stem cell layer. *Nat. Cell Biol.* Springer US, 24, 2022.

53. Conesa, M.A.V. *et al.* Predictive value of peripheral blood lymphocyte count in breast cancer patients treated with primary chemotherapy. *The Breast* 21:468–474, 2012.

54. Corre-Gallegos, D., D. Jiang, and Y. Rinkevich. Fibroblasts as confederates of the immune system. *Immunol. Rev.* 302:147–162, 2021.

55. Crawford, A., J.M. Angelosanto, K.L. Nadwodny, S.D. Blackburn, and E.J. Wherry. A Role for the Chemokine RANTES in Regulating CD8 T Cell Responses during Chronic Viral Infection. *PLoS Pathog.* 7, 2011.

56. Däster, S. *et al.* Induction of hypoxia and necrosis in multicellular tumor spheroids is associated with resistance to chemotherapy treatment. 8:1725–1736, 2017.

57. Dekkers, J.F. *et al.* High-resolution 3D imaging of fixed and cleared organoids. *Nat. Protoc.* 14:1756–1771, 2019. Available from: <http://dx.doi.org/10.1038/s41596-019-0160-8>.

58. Deleon-Pennell, K.Y., T.H. Barker, and M.L. Lindsey. Fibroblasts: The arbiters of extracellular matrix remodeling. *Matrix Biol.* Elsevier B.V., 91–92:1–7, 2020.

59. Demaria, O., S. Cornen, M. Daëron, Y. Morel, R. Medzhitov, and E. Vivier. Harnessing innate immunity in cancer therapy. *Nature* 574:45–56, 2019.

60. Demaria, S. *et al.* Ionizing radiation inhibition of distant untreated tumors (abscopal effect) is immune mediated. *Int. J. Radiat. Oncol. Biol. Phys.* 58:862–870, 2004.

61. DeNardo, D.G. *et al.* CD4<sup>+</sup>T Cells Regulate Pulmonary Metastasis of Mammary Carcinomas

by Enhancing Protumor Properties of Macrophages. *Cancer Cell* Elsevier Ltd, 16:91–102, 2009. Available from: <http://dx.doi.org/10.1016/j.ccr.2009.06.018>.

62. Dijkstra, K.K. *et al.* Generation of tumor-reactive T cells by co-culture of peripheral blood lymphocytes and tumor organoids. *Cell* 174:1586–1598, 2018.

63. Dou, Z. *et al.* Cytoplasmic chromatin triggers inflammation in senescence and cancer. *Nature* Nature Publishing Group, 550:402–406, 2017. Available from: <http://dx.doi.org/10.1038/nature24050>.

64. Dragun, A.E., J. Pan, S.N. Rai, B. Kruse, and D. Jain. Locoregional recurrence in patients with triple-negative breast cancer: preliminary results of a single institution study. *Am. J. Clin. Oncol. Cancer Clin. Trials* 34:231–237, 2011.

65. Drost, J., and H. Clevers. Organoids in cancer research. *Nat. Rev. Cancer* Springer US, , 2018. Available from: <http://dx.doi.org/10.1038/s41568-018-0007-6>.

66. Duluc, D. *et al.* Interferon- $\gamma$  reverses the immunosuppressive and protumoral properties and prevents the generation of human tumor-associated macrophages. *Int. J. Cancer* 125:367–373, 2009.

67. Durante, M., and S.C. Formenti. Radiation-Induced Chromosomal Aberrations and Immunotherapy: Micronuclei, Cytosolic DNA, and Interferon-Production Pathway. *Front. Oncol.* 8:1–9, 2018.

68. Durgeau, A., Y. Virk, S. Corgnac, and F. Mami-Chouaib. Recent Advances in Targeting CD8 T-Cell immunity for More effective Cancer immunotherapy. *Front. Immunol.* 9, 2018.

69. Ewald, A.J. Isolation of mouse mammary organoids for long-term time-lapse imaging. *Cold*

*Spring Harb. Protoc.* 8:130–133, 2013.

70. Ewald, A.J. Practical considerations for long-term time-lapse imaging of epithelial morphogenesis in three-dimensional organotypic cultures. *Cold Spring Harb. Protoc.* 8:100–117, 2013.

71. Ewald, A.J., A. Brenot, M. Duong, B.S. Chan, and Z. Werb. Collective Epithelial Migration and Cell Rearrangements Drive Mammary Branching Morphogenesis. *Dev. Cell* 14:570–581, 2008.

72. Fajardo, L.F. The pathology of ionizing radiation as defined by morphologic patterns. *Acta Oncol. (Madr)*. 44:13–22, 2005.

73. Feng, F. *et al.* Low lymphocyte count and high monocyte count predicts poor prognosis of gastric cancer. *BMC Gastroenterol.* BMC Gastroenterology, 1–7, 2018.

74. Fessenden, T.B. *et al.* Dia1-dependent adhesions are required for invasion by epithelial tissues. *J. Cell Biol.* 217:1485–1502, 2018.

75. Feys, L. *et al.* Radiation-induced lung damage promotes breast cancer lung-metastasis through CXCR4 signaling. *Oncotarget* 6:26615–26632, 2015.

76. Folkman, J., and K. Camphausen. What does Radiotherapy do to Endothelial Cells? *Science (80-. )*. 293:227–228, 2001.

77. Francke, A., J. Herold, S. Weinert, R.H. Strasser, R.C. Braun-dullaesus, and D. Cells. Generation of Mature Murine Monocytes from Heterogeneous Bone Marrow and Description of Their Properties. *J. Histochem. Cytochem.* 59:813–825, 2011.

78. Furuta, S., G. Ren, J.H. Mao, and M.J. Bissell. Laminin signals initiate the reciprocal loop that

informs breast-specific gene expression and homeostasis by activating NO, p53 and microRNAs. *Elife* 7:1–40, 2018.

79. Gabryś, D., O. Greco, G. Patel, K.M. Prise, G.M. Tozer, and C. Kanthou. Radiation Effects on the Cytoskeleton of Endothelial Cells and Endothelial Monolayer Permeability. *Int. J. Radiat. Oncol. Biol. Phys.* 69:1553–1562, 2007.

80. Garcia-Barros, M. *et al.* Tumor response to radiotherapy regulated by endothelial cell apoptosis. *Science (80-. )*. 300:1155–1159, 2003.

81. García-Tejido, P., M.L. Cabal, I.P. Fernández, and Y.F. Pérez. Tumor-Infiltrating Lymphocytes in Triple Negative Breast Cancer: The Future of Immune Targeting. *Clin. Med. Insights Oncol.* 10:31–39, 2016.

82. Gatei, M. *et al.* ATM Protein-dependent Phosphorylation of Rad50 Protein Regulates DNA Repair and Cell Cycle Control \* □. *J. Biol. Chem.* Â© 2011 ASBMB. Currently published by Elsevier Inc; originally published by American Society for Biochemistry and Molecular Biology., 286:31542–31556, 2011. Available from: <http://dx.doi.org/10.1074/jbc.M111.258152>.

83. Gautam, J. *et al.* Down-regulation of cathepsin S and matrix metalloproteinase-9 via Src, a non-receptor tyrosine kinase, suppresses triple-negative breast cancer growth and metastasis. *Exp. Mol. Med.* Springer US, 50:1–14, 2018.

84. Golubovskaya, V., and L. Wu. Different Subsets of T Cells, Memory, Effector Functions, and CAR-T Immunotherapy. *Cancers (Basel)*. 137, 2016.

85. Gravett, A.M. *et al.* Gemcitabine alters the proteasome composition and immunopeptidome of tumour cells. *Oncoimmunology* Taylor & Francis, 7:1–13, 2018. Available from:

<https://doi.org/10.1080/2162402X.2018.1438107>.

86. Gregoire, F.M., C.M. Smas, and H.S. Sul. Understanding Adipocyte Differentiation. *Physiol. Rev.* 78:783–809, 1998. Available from: <http://www.physiology.org/doi/10.1152/physrev.1998.78.3.783>.
87. Grither, W.R., and G.D. Longmore. Inhibition of tumor–microenvironment interaction and tumor invasion by small-molecule allosteric inhibitor of DDR2 extracellular domain. *Proc. Natl. Acad. Sci.* 115:E7786–E7794, 2018.
88. Groselj, B. *et al.* Radiosensitization In Vivo by Histone Deacetylase Inhibition with No Increase in Early Normal Tissue Radiation Toxicity . *Mol. Cancer Ther.* 17:381–392, 2017.
89. Grudzenski, S., A. Raths, S. Conrad, C.E. Rube, and M. Löbrich. Inducible response required for repair of low-dose radiation damage in human fibroblasts. *Proc. Natl. Acad. Sci.* 107:14205–14210, 2010.
90. Guet, R. *et al.* The Process of Macrophage Migration Promotes Matrix Metalloproteinase-Independent Invasion by Tumor Cells. *J. Immunol.* 187:3806–3814, 2011.
91. Hacker, B.C., J.D. Gomez, C.A. Silvera Batista, and M. Rafat. Growth and characterization of irradiated organoids from mammary glands. *J. Vis. Exp.* 147:e59293, 2019.
92. Hacker, B.C., and M. Rafat. Organoids as Complex In Vitro Models for Studying Radiation-Induced Cell Recruitment. *Cell. Mol. Bioeng.* 13:341–357, 2020.
93. Hama, H. *et al.* ScaleS: An optical clearing palette for biological imaging. *Nat. Neurosci.* 18:1518–1529, 2015.
94. Hamilton, J.A. Colony-stimulating factors in inflammation and autoimmunity. *Nat. Rev.*

*Immunol.* 8:533–544, 2008.

95. Han, Y.L. *et al.* Cell contraction induces long-ranged stress stiffening in the extracellular matrix. *Proc. Natl. Acad. Sci.* 115:4075–4080, 2018.

96. Hanahan, D., and R.A. Weinberg. Hallmarks of cancer: the next generation. *Cell* 144:646–674, 2011.

97. Hay, K.A. Br J Haematol - 2018 - Hay - Cytokine release syndrome and neurotoxicity after CD19 chimeric antigen receptor-modified .pdf. *Br. J. Haematol.* 364–374, 2018.

98. Henao-mejia, J., E. Elinav, T. Strowig, and R.A. Flavell. Inflammasomes: far beyond inflammation. *Nat. Publ. Gr.* Nature Publishing Group, 13:321–324, 2012.

99. Heo, T., J. Wahler, and N. Suh. Potential therapeutic implications targeting agents in breast cancer. *Oncotarget* 7:15460–15473, 2016.

100. Hewitt, E.W. The MHC class I antigen presentation pathway : strategies for viral immune evasion. *Immunology* 163–169, 2003.

101. Heylmann, D., F. Rödel, T. Kindler, and B. Kaina. Biochimica et Biophysica Acta Radiation sensitivity of human and murine peripheral blood lymphocytes , stem and progenitor cells. *BBA - Rev. Cancer* Elsevier B.V., 1846:121–129, 2014. Available from: <http://dx.doi.org/10.1016/j.bbcan.2014.04.009>.

102. Horder, H. *et al.* Bioprinting and Differentiation of Adipose-Derived Stromal Cell Spheroids for a 3D Breast Cancer-Adipose Tissue Model. *Cells* 10:1–17, 2021.

103. Hu, J. *et al.* Regulation of tumor immune suppression and cancer cell survival by CXCL1 / 2 elevation in glioblastoma multiforme. *Sci. Adv.* 1–12, 2021.

104. Huang, Q. *et al.* Caspase 3-mediated stimulation of tumor cell repopulation during cancer radiotherapy. *Nat. Med.* 17:860–866, 2011.
105. Huang, X. *et al.* M-HIFU inhibits tumor growth, suppresses STAT3 activity and enhances tumor specific immunity in a transplant tumor model of prostate cancer. *PLoS One* 7:1–11, 2012.
106. Huebner, R.J., N.M. Neumann, and A.J. Ewald. Mammary epithelial tubes elongate through MAPK-dependent coordination of cell migration. *Development* 143:983–995, 2016.
107. Hwang, P.Y., A. Brenot, A.C. King, G.D. Longmore, and S.C. George. Randomly distributed K14+ breast tumor cells polarize to the leading edge and guide collective migration in response to chemical and mechanical environmental cues. *Cancer Res.* 79:1899–1912, 2019.
108. Ilatovskaya, D. V, G. V Halade, and X.K.Y. Deleon-pennell. Adaptive immunity-driven inflammation and cardiovascular disease. 1:1254–1257, 2023.
109. Ingber, D., and J. Folkman. Mechanochemical switching between growth and differentiation during fibroblast growth factor-stimulated angiogenesis in vitro: role of extracellular matrix. *J. Cell Biol.* 109, 1989. Available from: <http://jcb.rupress.org/content/109/1/317.abstract>.
110. Jдалиha, M. *et al.* A natural antisense lncRNA controls breast cancer progression by promoting tumor suppressor gene mRNA stability. *PLoS Genet.* 1–24, 2018.
111. Jalili-Firoozinezhad, S. *et al.* Modeling radiation injury-induced cell death and countermeasure drug responses in a human Gut-on-a-Chip. *Cell Death Dis.* 9:1–14, 2018.
112. Jamieson, P.R., J.F. Dekkers, A.C. Rios, N.Y. Fu, G.J. Lindeman, and J.E. Visvader. Derivation of a robust mouse mammary organoid system for studying tissue dynamics. *Development* 144:1065–1071, 2016.

113. Janssens, K. *et al.* Leukemia inhibitory factor tips the immune balance towards regulatory T cells in multiple sclerosis. *Brain Behav. Immun.* Elsevier Inc., 45:180–188, 2015. Available from: <http://dx.doi.org/10.1016/j.bbi.2014.11.010>.
114. Jardé, T. *et al.* Wnt and Neuregulin1/ErbB signalling extends 3D culture of hormone responsive mammary organoids. *Nat. Commun.* 7:1–14, 2016.
115. Jiang, Y. *et al.* Hypoxia potentiates the radiation-sensitizing effect of olaparib in human non-small cell lung cancer xenografts by contextual synthetic lethality. *Int. J. Radiat. Oncol. Biol. Phys.* 95:772–781, 2016. Available from: <http://dx.doi.org/10.1016/j.ijrobp.2016.01.035>.
116. Jimbo, H., Y. Horimoto, Y. Ishizuka, N. Nogami, A. Shikanai, and M. Saito. Absolute lymphocyte count decreases with disease progression and is a potential prognostic marker for metastatic breast cancer. *Breast Cancer Res. Treat.* Springer US, 196:291–298, 2022. Available from: <https://doi.org/10.1007/s10549-022-06748-4>.
117. Kamran, M.Z., A. Ranjan, N. Kaur, S. Sur, and V. Tandon. Radioprotective Agents : Strategies and Translational Advances. *Med. Res. Rev.* 461–493, 2016.
118. Karantanos, T., and S.K.B.S.G. Gignac. The absolute lymphocyte count can predict the overall survival of patients with non - small cell lung cancer on nivolumab : a clinical study. *Clin. Transl. Oncol.* Springer International Publishing, 21:206–212, 2019. Available from: <https://doi.org/10.1007/s12094-018-1908-2>.
119. Kaur, S., Y. Bansal, R. Kumar, and G. Bansal. Bioorganic & Medicinal Chemistry A panoramic review of IL-6 : Structure , pathophysiological roles and inhibitors. *Bioorg. Med. Chem.* Elsevier, 28:115327, 2020.

120. Kawai, T., and S. Akira. Signaling to NF- $\kappa$ B by Toll-like receptors. *Trends Mol. Med.* 13, 2007.
121. Ke, M.T., S. Fujimoto, and T. Imai. SeeDB: A simple and morphology-preserving optical clearing agent for neuronal circuit reconstruction. *Nat. Neurosci.* Nature Publishing Group, 16:1154–1161, 2013.
122. Kim, M.Y. *et al.* Tumor self-seeding by circulating cancer cells. *Cell* 139:1315–1326, 2009.
123. Kioi, M., J.M. Brown, H. Vogel, G. Schultz, R.M. Hoffman, and G.R. Harsh. Inhibition of vasculogenesis, but not angiogenesis, prevents the recurrence of glioblastoma after irradiation in mice. *J. Clin. Invest.* 120:694–705, 2010.
124. Klingelhutz, A.J. *et al.* Scaffold-free generation of uniform adipose spheroids for metabolism research and drug discovery. *Sci. Rep.* 8:1–12, 2018. Available from: <http://dx.doi.org/10.1038/s41598-017-19024-z>.
125. Koledova, Z. 3D coculture of mammary organoids with fibrospheres: A model for studying epithelial–stromal interactions during mammary branching morphogenesis. In: *Methods in Molecular Biology*, edited by Z. Koledova. Humana Press, New York, NY, 2017.
126. Kopanska, K.S., Y. Alcheikh, R. Staneva, D. Vignjevic, and T. Betz. Tensile forces originating from cancer spheroids facilitate tumor invasion. *PLoS One* 11:1–23, 2016.
127. Krizhanovsky, V. *et al.* Senescence of Activated Stellate Cells Limits Liver Fibrosis. 657–667, 2008.
128. Kuen, J., D. Darowski, T. Kluge, and M. Majety. Pancreatic cancer cell/fibroblast co-culture induces M2 like macrophages that influence therapeutic response in a 3D model. *PLoS One* 12:1–

19, 2017.

129. Kuo, P. *et al.* Galectin-1 Mediates Radiation-Related Lymphopenia and Attenuates NSCLC Radiation Response. *Clin. Cancer Res.* 20:5558–5569, 2014.

130. LaBarge, M.A., J.C. Garbe, and M.R. Stampfer. Processing of Human Reduction Mammoplasty and Mastectomy Tissues for Cell Culture. *J. Vis. Exp.* 1–7, 2013.

131. Laidlaw, B.J., J.E. Craft, and S.M. Kaech. The multifaceted role of CD4 + T cells in CD8 + T cell memory. *Nat. Publ. Gr.* Nature Publishing Group, 16, 2016.

132. Lampros, M., N. Vlachos, S. Voulgaris, and G.A. Alexiou. The Role of Hsp27 in Chemotherapy Resistance. , 2022.

133. Lan, C. *et al.* Expression of M2-polarized macrophages is associated with poor prognosis for advanced epithelial ovarian cancer. *Technol. Cancer Res. Treat.* 12:259–267, 2013.

134. Langhi Parata, L.G.P., I.G. Ovsyannikova, T. Tchkonja, and J.L. Kirkland. Seminars in Immunology Senescent cell clearance by the immune system : Emerging therapeutic opportunities. *Semin. Immunol.* Elsevier, 40:101275, 2019. Available from: <https://doi.org/10.1016/j.smim.2019.04.003>.

135. Laperrousaz, B. *et al.* Direct transfection of clonal organoids in Matrigel microbeads: a promising approach toward organoid-based genetic screens. *Nucleic Acids Res.* 46:1–13, 2018.

136. Lasfargues, E. Cultivation and behavior in vitro of the normal mammary epithelium of the adult mouse. *Anat. Rec.* 127:117–129, 1957.

137. Lautner, M. *et al.* Disparities in the Use of Breast-Conserving Therapy Among Patients With Early-Stage Breast Cancer. *J. Am. Med. Assoc. Surg.* 150:778–786, 2015.

138. Lewis, M.D., E. De Leenheer, S. Fishman, L. Khai, G. Gross, and F.S. Wong. Technical note A reproducible method for the expansion of mouse CD8 + T lymphocytes. *J. Immunol. Methods* Elsevier B.V., 417:134–138, 2015. Available from: <http://dx.doi.org/10.1016/j.jim.2015.01.004>.
139. Li, Y., J.-S. Park, J.-H. Deng, and Y. Bai. Cytochrome c Oxidase Subunit IV is Essential for Assembly and Respiratory Function of the Enzyme Complex. *J Bionerg Biomembr.* 38:283–291, 2006.
140. Liang, D. *et al.* SIRT1 / PGC-1 pathway activation triggers autophagy / mitophagy and attenuates oxidative damage in intestinal epithelial cells. *Biochimie* Elsevier Ltd, 170:10–20, 2020. Available from: <https://doi.org/10.1016/j.biochi.2019.12.001>.
141. Linde, N. *et al.* Macrophages orchestrate breast cancer early dissemination and metastasis. *Nat. Commun.* 9:1–14, 2018.
142. Linnemann, J.R. *et al.* Quantification of regenerative potential in primary human mammary epithelial cells. *Development* 142:3239–3251, 2015. Available from: <http://dev.biologists.org/cgi/doi/10.1242/dev.123554>.
143. Liu, H.L., H.Y. Hsieh, L.A. Lu, C.W. Kang, M.F. Wu, and C.Y. Lin. Low-pressure pulsed focused ultrasound with microbubbles promotes an anticancer immunological response. *J. Transl. Med.* 10:1–14, 2012.
144. Loi, S. *et al.* Tumor infiltrating lymphocytes are prognostic in triple negative breast cancer and predictive for trastuzumab benefit in early breast cancer: results from the FinHER trial. *Ann. Oncol.* 25:1544–1550, 2014.
145. López Alfonso, J.C. *et al.* Temporally feathered intensity-modulated radiation therapy: A

planning technique to reduce normal tissue toxicity. *Med. Phys.* pp. 3466–3474, 2018.

146. Lowery, A., M. Kell, R. Glynn, M. Kerin, and K. Sweeney. Locoregional recurrence after breast cancer surgery : a systematic review by receptor phenotype. *Breast Cancer Res. Treat.* 133:831–841, 2012.

147. Lu, L., M. Jiang, C. Zhu, J. He, and S. Fan. Amelioration of whole abdominal irradiation-induced intestinal injury in mice with 3,3'-Diindolylmethane (DIM). *Free Radic. Biol. Med.* pp. 244–255, 2019.

148. Luo, Y. *et al.* Targeting tumor-associated macrophages as a novel strategy against breast cancer. *J. Clin. Invest.* 116:2132–2141, 2006.

149. Ma, J., L. Liu, G. Che, N. Yu, F. Dai, and Z. You. The M1 form of tumor-associated macrophages in non-small cell lung cancer is positively associated with survival time. *BioMed Cent. Cancer* 10:112, 2010. Available from: <http://dx.doi.org/10.1186/1471-2407-10-112>.

150. Ma, R.Y. *et al.* Monocyte-derived macrophages promote breast cancer bone metastasis outgrowth. *J. Exp. Med.* 217:1–12, 2020.

151. Macarak, E.J., J. Rosenbloom, T. Joan, C. Biology, and T. Jefferson. Therapeutic Approaches to Radiation-Induced Fibrosis. *J Cancer Treat. Diagn* 2:7–9, 2018.

152. Magee, C.N., O. Boenisch, and N. Najafian. THE ROLE OF CO-STIMULATORY MOLECULES IN DIRECTING THE FUNCTIONAL DIFFERENTIATION OF ALLO-REACTIVE T HELPER CELLS. *Am J Transpl.* 12:2588–2600, 2012.

153. Maier, P., L. Hartmann, F. Wenz, and C. Herskind. Cellular pathways in response to ionizing radiation and their targetability for tumor radiosensitization. *Int. J. Mol. Sci.* 17, 2016.

154. Malandrino, A., M. Mak, R.D. Kamm, and E. Moeendarbary. Complex mechanics of the heterogeneous extracellular matrix in cancer. *Extrem. Mech. Lett.* Elsevier Ltd, 21:25–34, 2018. Available from: <https://doi.org/10.1016/j.eml.2018.02.003>.
155. Malandrino, A., X. Trepast, R.D. Kamm, and M. Mak. Dynamic filopodial forces induce accumulation, damage, and plastic remodeling of 3D extracellular matrices. *PLoS Comput. Biol.* 15:1–26, 2019.
156. Mandl, I., J.D. McLennan, and E.L. Howes. Isolation and Characterization of Proteinase and Collagenase From *Cl. histolyticum*. *J. Clin. Invest.* 32:1323–1329, 1953.
157. Mandl, I., and S.F. Zaffuto. Serological Evidence for a Specific *Clostridium histolyticum* Gelatinase. *J. Gen. Microbiol.* 18:13–15, 1958.
158. Martin, I., D. Wendt, and M. Heberer. The role of bioreactors in tissue engineering. *Trends Biotechnol.* 22:80–86, 2004.
159. Matsumoto, H., A. Aye, T. Huihua, and L. Joe. Increased CD4 and CD8-positive T cell infiltrate signifies good prognosis in a subset of triple-negative breast cancer. *Breast Cancer Res. Treat.* Springer US, 156:237–247, 2016.
160. Medzhitov, R., and C.A. Janeway. Innate immune recognition and control of adaptive immune responses. *Semin. Immunol.* 10:351–353, 1998.
161. Meng, L. *et al.* Tumor oxygenation and hypoxia inducible factor-1 functional inhibition via a reactive oxygen species responsive nanoplatform for enhancing radiation therapy and abscopal effects. *ACS Nano* 12:8308–8322, 2018.
162. Metcalfe, C., N.M. Kljavin, R. Ybarra, and F.J. De Sauvage. Lgr5+stem cells are

indispensable for radiation-induced intestinal regeneration. *Cell Stem Cell* 14:149–159, 2014.

163. Meunier, S., L. Rapetti, L. Beziaud, C. Pontoux, A. Lgrand, and C. Tanchot. Synergistic CD40 signaling on APCs and CD8 T cells drives efficient CD8 response and memory differentiation. *J. Leukoc. Biol.* 91:859–869, 2012.

164. Miller, D.H. *et al.* BCL11B drives human mammary stem cell self-renewal in vitro by inhibiting basal differentiation. *Stem Cell Reports* 10:1131–1145, 2018.

165. Miller, J.S. *et al.* Rapid casting of patterned vascular networks for perfusable engineered three-dimensional tissues. *Nat. Mater.* 11:768–774, 2012.

166. Milne, K. *et al.* Absolute lymphocyte count is associated with survival in ovarian cancer independent of tumor-infiltrating lymphocytes. *J. Transl. Med.* 1–12, 2012.

167. Montay-Gruel, P. *et al.* Irradiation in a flash: Unique sparing of memory in mice after whole brain irradiation with dose rates above 100 Gy/s. *Radiother. Oncol.* 124:365–369, 2017. Available from: <http://dx.doi.org/10.1016/j.radonc.2017.05.003>.

168. Montay-Gruel, P. *et al.* X-rays can trigger the FLASH effect: Ultra-high dose-rate synchrotron light source prevents normal brain injury after whole brain irradiation in mice. *Radiother. Oncol.* Elsevier Ireland Ltd, 129:582–588, 2018. Available from: <https://doi.org/10.1016/j.radonc.2018.08.016>.

169. Morgan, M.M. *et al.* Mammary fibroblasts reduce apoptosis and speed estrogen-induced hyperplasia in an organotypic MCF7-derived duct model. *Sci. Rep.* 8:1–13, 2018.

170. Morini, J., G. Babini, S. Barbieri, G. Baiocco, and A. Ottolenghi. The interplay between radioresistant Caco-2 cells and the immune system increases epithelial layer permeability and

alters signaling protein spectrum. *Front. Immunol.* 8:1–12, 2017.

171. Nagle, P.W. *et al.* Lack of DNA damage response at low radiation doses in adult stem cells contributes to organ dysfunction. *Clin. Cancer Res.* 24:6583–6593, 2018.

172. Nguyen-Ngoc, K.-V. *et al.* ECM microenvironment regulates collective migration and local dissemination in normal and malignant mammary epithelium. *Proc. Natl. Acad. Sci.* 89:E2595–E2604, 2012.

173. Nguyen-Ngoc, K.-V., E.R. Shamir, R.J. Huebner, J.N. Beck, K.J. Cheung, and A.J. Ewald. 3D culture assays of murine mammary branching morphogenesis and epithelial invasion. In: *Tissue Morphogenesis: Methods and Protocols*, edited by C.M. Nelson. New York: Springer Science and Business Media, 2015, pp. 135–162.

174. Nguyen, D.H. *et al.* Radiation acts on the microenvironment to affect breast carcinogenesis by distinct mechanisms that decrease cancer latency and affect tumor type. *Cancer Cell* 19:640–651, 2011.

175. Noël, G., C. Godon, M. Fernet, N. Giocanti, F. Mégnin-Chanet, and V. Favaudon. Radiosensitization by the poly(ADP-ribose) polymerase inhibitor 4-amino-1,8-naphthalimide is specific of the S phase of the cell cycle and involves arrest of DNA synthesis. *Mol. Cancer Ther.* 5:564–574, 2006.

176. Noman, A.S., M. Uddin, A.A. Chowdhury, M.J. Nayeem, Z. Raihan, and M.I. Rashid. Serum sonic hedgehog and interleukin-6 as dual prognostic biomarkers in progressive metastatic breast cancer. *Sci. Rep.* 7:1–12, 2017.

177. Nozaki, K. *et al.* Co-culture with intestinal epithelial organoids allows efficient expansion

and motility analysis of intraepithelial lymphocytes. *J. Gastroenterol.* 51:206–213, 2016.

178. Oh, K., O. Lee, S.Y. Shon, O. Nam, P.M. Ryu, and M.W. Seo. A mutual activation loop between breast cancer cells and myeloid-derived suppressor cells facilitates spontaneous metastasis through IL-6 trans-signaling in a murine model. *Breast Cancer Res.* 15:1–16, 2013.

179. Ohuchida, K. *et al.* Radiation to stromal fibroblasts increases invasiveness of pancreatic cancer cells through tumor-stromal interactions. *Cancer Res.* 64:3215–3222, 2004.

180. Panciera, T. *et al.* Induction of expandable tissue-specific stem/progenitor cells through transient expression of YAP/TAZ. *Cell Stem Cell* 19:725–737, 2016.

181. Paris, F. *et al.* Endothelial apoptosis as the primary lesion initiating intestinal radiation damage in mice. *Science (80-. ).* 293:293–297, 2001.

182. Park, I.A., S. Hwang, I.H. Song, S. Heo, and Y. Kim. Expression of the MHC class II in triple-negative breast cancer is associated with tumor-infiltrating lymphocytes and interferon signaling. 1–14, 2017.

183. Pascual-García, M. *et al.* LIF regulates CXCL9 in tumor-associated macrophages and prevents CD8<sup>+</sup> T cell tumor-infiltration impairing anti-PD1 therapy. *Nat. Commun.* 10:1–11, 2019.

184. Peperzak, V., E.A.M. Veraar, Y. Xiao, N. Ba, and K. Thiadens. CD8<sup>+</sup> T Cells Produce the Chemokine CXCL10 in Response to CD27/CD70 Costimulation To Promote Generation of the CD8 Effector T Cell Pool. *J. Immunol.* , 2018.

185. Pereira, B.I. *et al.* Senescent cells evade immune clearance via HLA-E-mediated NK and CD8<sup>+</sup> T cell inhibition. *Nat. Commun.* Springer US, 10:1–13, 2019. Available from:

<http://dx.doi.org/10.1038/s41467-019-10335-5>.

186. Philip, M., and A. Schietinger. CD8+ T cell differentiation and dysfunction in cancer. *Nat. Rev. Immunol.* Springer US, 22:209–223, 2022.

187. Plaks, V. *et al.* Adaptive Immune Regulation of Mammary Postnatal Organogenesis. *Dev. Cell* Elsevier Inc., 34:493–504, 2015. Available from: <http://dx.doi.org/10.1016/j.devcel.2015.07.015>.

188. Poglio, S. *et al.* Adipose tissue sensitivity to radiation exposure. *Am. J. Pathol.* 174:44–53, 2009.

189. Powell, D.R., and A. Huttenlocher. Neutrophils in the tumor microenvironment. *Trends Immunol.* 37:41–52, 2016.

190. Pyonteck, S.M. *et al.* CSF-1R inhibition alters macrophage polarization and blocks glioma progression. *Nat. Med.* Nature Publishing Group, 19:1264–1272, 2013. Available from: <http://dx.doi.org/10.1038/nm.3337>.

191. Qian, B. *et al.* CCL2 recruits inflammatory monocytes to facilitate breast tumor metastasis. *Nature* 475:222–225, 2012.

192. Radharani, N.N. V, A.S. Yadav, R. Nimma, T.V.S. Kumar, and A. Bulbule. Tumor-associated macrophage derived IL-6 enriches cancer stem cell population and promotes breast tumor progression via Stat-3 pathway. *Cancer Cell Int.* BioMed Central, 22:1–19, 2022.

193. Rafat, M. *et al.* Macrophages promote circulating tumor cell-mediated local recurrence following radiotherapy in immunosuppressed patients. *Cancer Res.* 78:4241–4252, 2018.

194. Ray, G. *et al.* Lipid peroxidation, free radical production and antioxidant status in breast

cancer. *Breast Cancer Res. Treat.* 59:163–170, 2000.

195. Reits, E.A. *et al.* Radiation modulates the peptide repertoire , enhances MHC class I expression , and induces successful antitumor immunotherapy. 203:1259–1271, 2006.

196. Richert, M.M. *et al.* An atlas of mouse mammary gland development. *J. Mammary Gland Biol. Neoplasia* 5:227–41, 2000. Available from: <http://www.ncbi.nlm.nih.gov/pubmed/11149575>.

197. Rodemann, H.P., and M.A. Blaese. Responses of normal cells to ionizing radiation. *Semin. Radiat. Oncol.* 17:81–88, 2007.

198. Rodney Withers, H. Biological basis of radiation therapy for cancer. *Lancet* 339:156–159, 1992.

199. Rossi, G., A. Manfrin, and M.P. Lutolf. Progress and potential in organoid research. *Nat. Rev. Genet.* 19:671–687, 2018. Available from: <http://dx.doi.org/10.1038/s41576-018-0051-9>.

200. Rossi, J.-F., Z.-Y. Lu, M. Jourdna, and B. Klein. Interleukin-6 as a Therapeutic Target. *Clin. Cancer Res.* 21:1248–1257, 2015.

201. Rutella, S., F. Zavala, S. Danese, H. Kared, and G. Leone. Granulocyte Colony-Stimulating Factor: A Novel Mediator of T cell Tolerance. *J. Immunol.* , 2005.

202. Ruysscher, D. De, G. Niedermann, N.G. Burnet, S. Siva, A.W.M. Lee, and F. Hegi-Johnson. Radiotherapy toxicity. *Nat. Rev. Dis. Prim.* 13:1–20, 2019.

203. Sachs, N. *et al.* A living biobank of breast cancer organoids captures disease heterogeneity. *Cell* 172:373–386, 2018.

204. Sachs, N. *et al.* Long-term expanding human airway organoids for disease modeling. *EMBO*

*J.* 38:1–20, 2019.

205. Sanidas, I. *et al.* Article A Code of Mono-phosphorylation Modulates the Function of RB. Article A Code of Mono-phosphorylation Modulates the Function of RB. *Mol. Cell* Elsevier Inc., 73:985-1000.e6, 2019. Available from: <https://doi.org/10.1016/j.molcel.2019.01.004>.

206. Sato, T. *et al.* Long-term expansion of epithelial organoids from human colon, adenoma, adenocarcinoma, and Barrett's epithelium. *Gastroenterology* 141:1762–1772, 2011.

207. Sato, T., and H. Clevers. SnapShot: Growing organoids from stem cells. *Cell* 161:1700-1700.e1, 2015.

208. Sayarath, M. *et al.* Ultrahigh dose-rate FLASH irradiation increases the differential response between normal and tumor tissue in mice. *Sci. Transl. Med.* 6:1–9, 2014.

209. Schae, D., E.L. Kachikwu, and W.H. McBride. Cytokines in Radiobiological Responses: A Review. *Radiat. Res.* 178:505–523, 2012.

210. Scott, M.A., V.T. Nguyen, B. Levi, and A.W. James. Current Methods of Adipogenic Differentiation of Mesenchymal Stem Cells. *Stem Cells Dev.* 20:1793–1804, 2011. Available from: <http://www.liebertonline.com/doi/abs/10.1089/scd.2011.0040>.

211. Sebastian, A. *et al.* Single-Cell Transcriptomic Analysis of Heterogeneity in Breast Cancer. *Cancers (Basel)*. 12:1–22, 2020.

212. Senra, J.M. *et al.* Inhibition of PARP-1 by Olaparib (AZD2281) Increases the Radiosensitivity of a Lung Tumor Xenograft. *Mol. Cancer Ther.* 10:1949–1958, 2011. Available from: <http://mct.aacrjournals.org/cgi/doi/10.1158/1535-7163.MCT-11-0278>.

213. Shabo, I., O. Stål, H. Olsson, S. Doré, and J. Svanvik. Breast cancer expression of CD163, a

macrophage scavenger receptor, is related to early distant recurrence and reduced patient survival. *Int. J. Cancer* 123:780–786, 2008.

214. Shamir, E.R. *et al.* Twist1-induced dissemination preserves epithelial identity and requires E-cadherin. *J. Cell Biol.* 204:839–856, 2014.

215. Shamir, E.R., and A.J. Ewald. Three-dimensional organotypic culture: Experimental models of mammalian biology and disease. *Nat. Rev. Mol. Cell Biol.* Nature Publishing Group, 15:647–664, 2014. Available from: <http://dx.doi.org/10.1038/nrm3873>.

216. Sherr, C.J. Cancer Cell Cycles. *Science (80-. )*. 274:1672–1677, 1996.

217. Sherry, A.D. *et al.* Systemic Inflammation After Radiation Predicts Locoregional Recurrence, Progression, and Mortality in Stage II-III Triple-Negative Breast Cancer. *Int. J. Radiat. Oncol. Biol. Phys.* Elsevier Inc., 108:268–276, 2020.

218. Siegel, R.L., K.D. Millder, H.E. Fuchs, and A. Jemal. Cancer statistics, 2022. *CA. Cancer J. Clin.* 72:7–33, 2022.

219. Siegel, R.L., K.D. Miller, and A. Jemal. Cancer statistics, 2018. *CA. Cancer J. Clin.* 69:7–34, 2019.

220. Simian, M., Y. Hirai, M. Navre, Z. Werb, A. Lochter, and M.J. Bissell. The interplay of matrix metalloproteinases, morphogens and growth factors is necessary for branching of mammary epithelial cells. *Development* 128:3117–3131, 2001.

221. Simmons, D.A. *et al.* Reduced cognitive deficits after FLASH irradiation of whole mouse brain are associated with less hippocampal dendritic spine loss and neuroinflammation. *Radiother. Oncol.* 139:4–10, 2019. Available from: <https://doi.org/10.1016/j.radonc.2019.06.006>.

222. Singh, M.K., B. Sharma, and P.K. Tiwari. The small heat shock protein Hsp27 : Present understanding and future prospects. *J. Therm. Biol.* Elsevier Ltd, 69:149–154, 2017. Available from: <http://dx.doi.org/10.1016/j.jtherbio.2017.06.004>.
223. Sirka, O.K., E.R. Shamir, and A.J. Ewald. Myoepithelial cells are a dynamic barrier to epithelial dissemination. *J. Cell Biol.* 217:3368–3381, 2018.
224. Skrzydlewska, E., S. Sulkowski, M. Koda, B. Zalewski, L. Kanczuga-Koda, and M. Sulkowska. Lipid peroxidation and antioxidant status in colorectal cancer. *World J Gastroenterol* 11:403–406, 2005.
225. Slonina, D., B. Biesaga, K. Urbanski, and Z. Kojs. Low-dose radiation response of primary keratinocytes and fibroblasts from patients with cervix cancer. *Radiat. Res.* 167:251–259, 2007.
226. Smith, T.A. *et al.* Radioprotective agents to prevent cellular damage due to ionizing radiation. *J. Transl. Med.* 1–18, 2017.
227. Sofia Vala, I. *et al.* Low doses of ionizing radiation promote tumor growth and metastasis by enhancing angiogenesis. *PLoS One* 5:1–13, 2010.
228. Sokol, E.S., D.H. Miller, A. Breggia, K.C. Spencer, L.M. Arendt, and P.B. Gupta. Growth of human breast tissues from patient cells in 3D hydrogel scaffolds. *Breast Cancer Res. Breast Cancer Research*, 18:1–13, 2016. Available from: <http://dx.doi.org/10.1186/s13058-016-0677-5>.
229. Sommerfeld, S.D. *et al.* Interleukin-36 gamma-producing macrophages drive IL-17 mediated fibrosis. *Sci. Immunol.* 4:1–13, 2019.
230. Spill, F., C. Bakal, and M. Mak. Mechanical and Systems Biology of Cancer. *Comput. Struct. Biotechnol. J.* 16:237–245, 2018. Available from: <https://doi.org/10.1016/j.csbj.2018.07.002>.

231. Stephens, T.C., G.A. Currie, and J.H. Peacock. Repopulation of gamma-irradiated lewis lung carcinoma by malignant cells and host macrophage progenitors. *Br. J. Cancer* 38:573–582, 1978.
232. Stovgaard, E.S., D. Nielsen, E. Hogdall, and E. Balslev. Triple negative breast cancer–prognostic role of immune-related factors: a systematic review. *Acta Oncol. (Madr)*. Informa UK Limited, trading as Taylor & Francis Group, 57:74–82, 2018.
233. Szumiel, I. Ionizing radiation-induced oxidative stress, epigenetic changes and genomic instability: The pivotal role of mitochondria. *Int. J. Radiat. Biol.* 91:1–12, 2015.
234. Taniguchi, C.M. *et al.* PHD inhibition mitigates and protects against radiation-induced gastrointestinal toxicity via HIF2. *Sci. Transl. Med.* 6:1–9, 2014.
235. Taylor, J. *et al.* Generation of immune cell containing adipose organoids for in vitro analysis of immune metabolism. *Sci. Rep.* Nature Publishing Group UK, 10:1–14, 2020.
236. Tevis, K.M., R.J. Cecchi, Y.L. Colson, and M.W. Grinstaff. Mimicking the tumor microenvironment to regulate macrophage phenotype and assessing chemotherapeutic efficacy in embedded cancer cell/macrophage spheroid models. *Acta Biomater.* 50:271–279, 2017. Available from: <http://dx.doi.org/10.1016/j.actbio.2016.12.037>.
237. Thwaites, M.J., M.J. Cecchini, D.T. Passos, I. Welch, and F.A. Dick. Interchangeable Roles for E2F Transcriptional Repression by the Retinoblastoma Protein and p27 KIP1 – Cyclin-Dependent Kinase Regulation in Cell Cycle Control and Tumor Suppression. *Mol. Cell. Biol.* 37, 2017.
238. Tooze, R.M. A replicative self-renewal model for long-lived plasma cells: questioning irreversible cell cycle exit. *Front. Immunol.* 4:1–11, 2013.

239. Tsai, K.K.C., E.Y.Y. Chuang, J.B. Little, and Z.M. Yuan. Cellular mechanisms for low-dose ionizing radiation-induced perturbation of the breast tissue microenvironment. *Cancer Res.* 65:6734–6744, 2005.
240. Tsikas, D. Assessment of lipid peroxidation by measuring malondialdehyde (MDA) and relatives in biological samples: Analytical and biological challenges. *Anal. Biochem.* 524:13–30, 2017.
241. Turner, M.D., B. Nedjai, T. Hurst, and D.J. Pennington. Biochimica et Biophysica Acta Cytokines and chemokines : At the crossroads of cell signalling and in fl ammatory disease. *BBA - Mol. Cell Res.* Elsevier B.V., 1843:2563–2582, 2014. Available from: <http://dx.doi.org/10.1016/j.bbamcr.2014.05.014>.
242. Unver, N., and F. Mcallister. IL-6 family cytokines : Key inflammatory mediators as biomarkers and potential therapeutic targets. *Cytokine Growth Factor Rev.* 1–8, 2018.
243. van Kooten, C., and J. Banchereau. CD40-CD40 ligand. *J. Leukoc. Biol.* 67, 2000.
244. van Luijk, P. *et al.* Sparing the region of the salivary gland containing stem cells preserves saliva production after radiotherapy for head and neck cancer. *Sci. Transl. Med.* 7:1–8, 2015.
245. Vanpouille-Box, C. *et al.* DNA exonuclease Trex1 regulates radiotherapy-induced tumour immunogenicity. *Nat. Commun.* 8:1–15, 2017. Available from: <http://dx.doi.org/10.1038/ncomms15618>.
246. Venkatesulu, B.P. *et al.* Radiation-Induced Endothelial Vascular Injury. *JACC Basic to Transl. Sci.* 3:563–572, 2018.
247. Venning, F.A. *et al.* Deciphering the temporal heterogeneity of cancer-associated fibroblast

- subpopulations in breast cancer. *J. Exp. Clin. Cancer Res.* 40:1–21, 2021.
248. Vicente, R., C. Jorgensen, P. Louis-plence, and J. Brondello. Cellular senescence impact on immune cell fate and function *Aging Cell.* 33:400–406, 2016.
249. Vilalta, M., M. Rafat, A.J. Giaccia, and E.E. Graves. Recruitment of Circulating Breast Cancer Cells Is Stimulated by Radiotherapy. *Cell Rep.* The Authors, 8:402–409, 2014. Available from: <http://dx.doi.org/10.1016/j.celrep.2014.06.011>.
250. Vilalta, M., M. Rafat, and E.E. Graves. Effects of radiation on metastasis and tumor cell migration. *Cell. Mol. Life Sci.* 73:2999–3007, 2016.
251. von Essen, C.F. Radiation enhancement of metastasis: a review. *Clin. Exp. Metastasis* 9:77–104, 1991.
252. Wakabayashi, H., T. Hamaguchi, N. Nagao, S. Kato, T. Iino, and T. Nakamura. Interleukin - 6 receptor inhibitor suppresses bone metastases in a breast cancer cell line. *Breast Cancer Springer Japan*, 25:566–574, 2018.
253. Wang, F. *et al.* Reciprocal interactions between  $\beta$ 1-integrin and epidermal growth factor receptor in three-dimensional basement membrane breast cultures: A different perspective in epithelial biology. *Proc. Natl. Acad. Sci.* 95:14821–14826, 1998.
254. Wang, X., Q. Sun, and J. Pei. Microfluidic-based 3D engineered microvascular networks and their applications in vascularized microtumor models. *Micromachines* 9:1–26, 2018.
255. Wang, X.Y., Z.H. Jin, B.W. Gan, S.W. Lv, M. Xie, and W.H. Huang. Engineering interconnected 3D vascular networks in hydrogels using molded sodium alginate lattice as the sacrificial template. *Lab Chip* 14:2709–2716, 2014.

256. Weber, G.F. *et al.* Interleukin-3 amplifies acute inflammation and is a potential therapeutic target in sepsis. *Science (80-. )*. 347:1260–1265, 2015.
257. Weigelt, B., J.L. Peterse, and L.J. Van't Veer. Breast cancer metastasis: Markers and models. *Nat. Rev. Cancer* 5:591–602, 2005.
258. Welsch, C.W. Review of the effects of dietary fat on experimental mammary gland tumorigenesis: Role of lipid peroxidation. *Free Radic. Biol. Med.* 18:757–773, 1995.
259. Weng, Y. *et al.* MCT-1/miR-34a/IL-6/IL-6R signaling axis promotes EMT progression, cancer stemness and M2 macrophage polarization in triple-negative breast cancer. *Mol. Cancer* 18:1–15, 2019.
260. Wiehagen, K.R. *et al.* Combination of CD40 Agonism and CSF-1R Blockade Reconditions Tumor-Associated Macrophages and Drives Potent Antitumor Immunity. *Cancer Immunol. Res.* 26–30, 2017.
261. Winslow, S. *et al.* Macrophages attenuate the transcription of CYP1A1 in breast tumor cells and enhance their proliferation. *PLoS One* 14:1–12, 2019.
262. Wong, E., S. Chaudhry, and M. Rossi. Breast cancer. *McMaster Pathophysiol. Rev.* , 2012.
263. Wouters, B.G. Oncology scan-how radiation effects on cells in the stromal microenvironment influence tumor development, proliferation, and recovery. *Int. J. Radiat. Oncol. Biol. Phys.* 86:593–595, 2013.
264. Xu, K., and R.J. Buchsbaum. Isolation of mammary epithelial cells from three-dimensional mixed-cell spheroid co-culture. *J. Vis. Exp.* 1–5, 2012.
265. Yang, Y., N. Lu, J. Zhou, Z. Chen, and P. Zhu. Cyclophilin A up-regulates MMP-9 expression

and adhesion of monocytes / macrophages via CD147 signalling pathway in rheumatoid arthritis. *Rheumatology* 1299–1310, 2008.

266. Ying, W., P.S. Cheruku, F.W. Bazer, S.H. Safe, and B. Zhou. Investigation of Macrophage Polarization Using Bone Marrow Derived Macrophages. *J. Vis. Exp.* 76:1–8, 2013.

267. Yurdagul, A. *et al.* Macrophage Metabolism of Apoptotic Cell-Derived Arginine Promotes Continual Efferocytosis and Resolution of Injury. *Cell Metab.* Elsevier Inc., 31:518–533, 2020.

268. Zanoni, M. *et al.* 3D tumor spheroid models for in vitro therapeutic screening: A systematic approach to enhance the biological relevance of data obtained. *Sci. Rep.* Nature Publishing Group, 6:1–11, 2016.

269. Zhang, C. *et al.* Higher locoregional recurrence rate for triple-negative breast cancer following neoadjuvant chemotherapy, surgery and radiotherapy. *Springerplus* 4:1–9, 2015.

270. Zhang, L. *et al.* Establishing estrogen-responsive mouse mammary organoids from single Lgr5+cells. *Cell. Signal.* Elsevier B.V., 29:41–51, 2016. Available from: <http://dx.doi.org/10.1016/j.cellsig.2016.08.001>.

271. Zhang, M. *et al.* A high M1/M2 ratio of tumor-associated macrophages is associated with extended survival in ovarian cancer patients. *J. Ovarian Res.* 7:1–16, 2014.

272. Zhang, S., M. Zhong, C. Wang, Y. Xu, W. Gao, and Y. Zhang. CCL5-deficiency enhances intratumoral infiltration of CD8 + T cells in colorectal cancer. *Cell Death Dis.* , 2018.

273. Zhang, X., R. Goncalves, and D.M. Mosser. The Isolation and Characterization of Murine Macrophages. *Curr. Protoc. Immunol.* 1–18, 2008.

274. Zhang, Z. *et al.* Genistein promotes ionizing radiation-induced cell death by reducing

cytoplasmic Bcl-xL levels in non-small cell lung cancer. *Sci. Rep.* 8:1–9, 2018. Available from: <http://dx.doi.org/10.1038/s41598-017-18755-3>.

275. Zhao, J., M. Griffin, J. Cai, S. Li, P.E.M. Bulter, and D.M. Kalaskar. Bioreactors for tissue engineering: An update. *Biochem. Eng. J.* 109:268–281, 2016. Available from: <http://dx.doi.org/10.1016/j.bej.2016.01.018>.

276. Zheng, Z., S. Jia, C. Shao, and Y. Shi. Irradiation induces cancer lung metastasis through activation of the cGAS–STING–CCL5 pathway in mesenchymal stromal cells. *Cell Death Dis.* Springer US, 11, 2020.

277. Zhong, J. *et al.* Temporal profiling of the secretome during adipogenesis in humans. *J. Proteome Res.* 9:5228–5238, 2010.

278. Zubeldia-Plazaola, A. *et al.* Glucocorticoids promote transition of ductal carcinoma in situ to invasive ductal carcinoma by inducing myoepithelial cell apoptosis. *Breast Cancer Res.* 20:1–16, 2018.

## APPENDICES

### APPENDIX A – Appendix Data

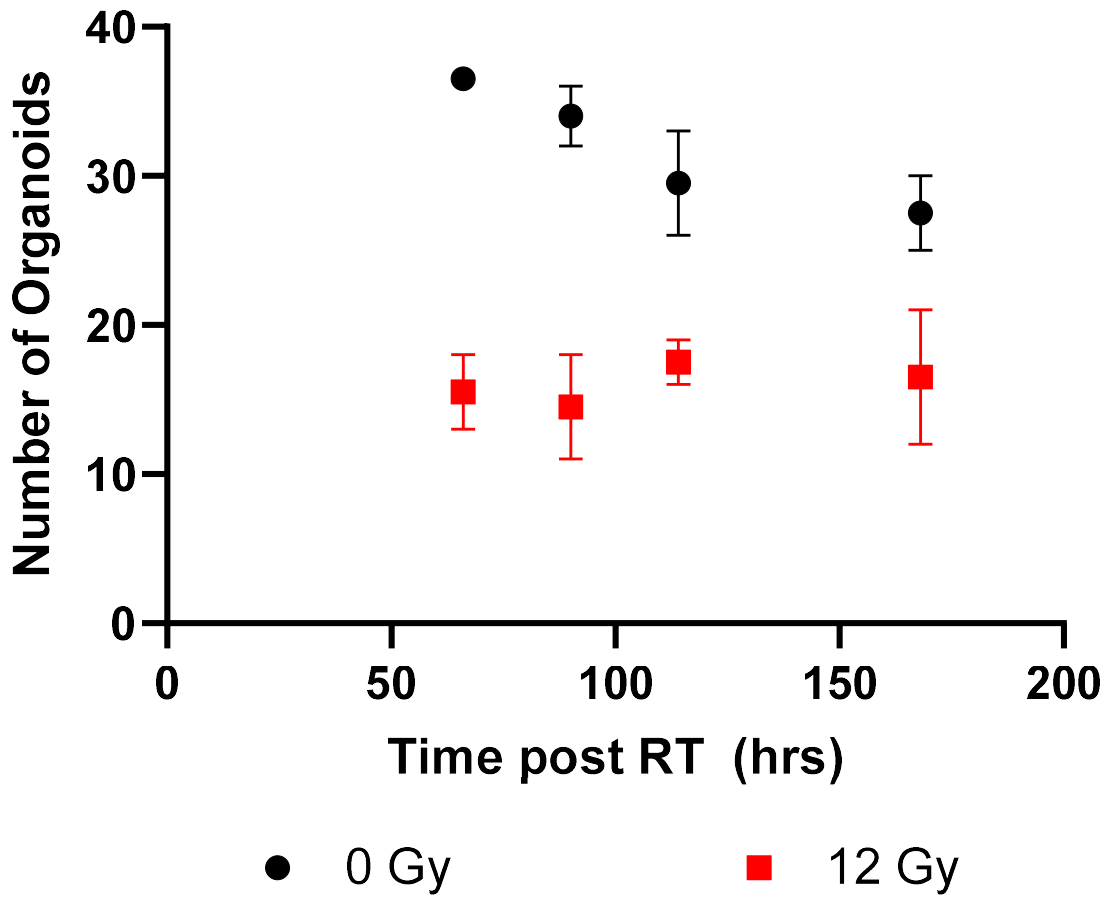


**Figure A.1. Organoid clumping over time.**

Organoid numbers over time after RT. Data is mean  $\pm$  SEM, N = 2 biological replicates.

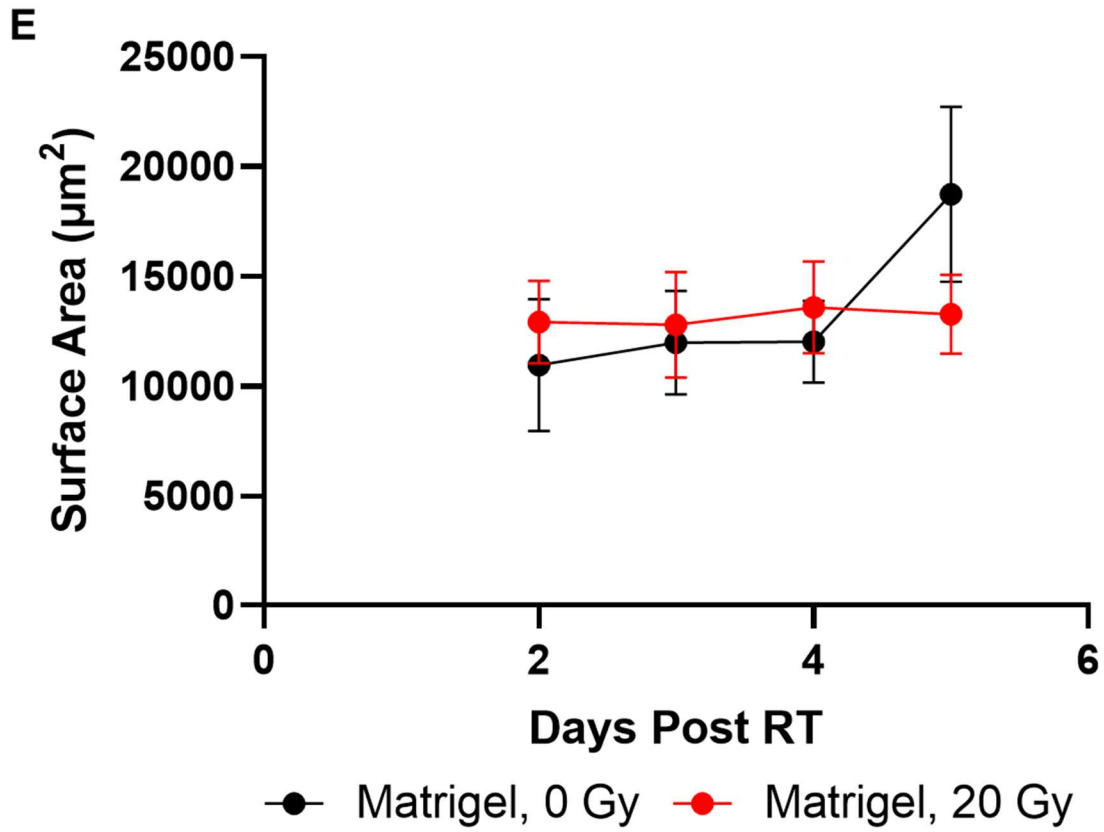
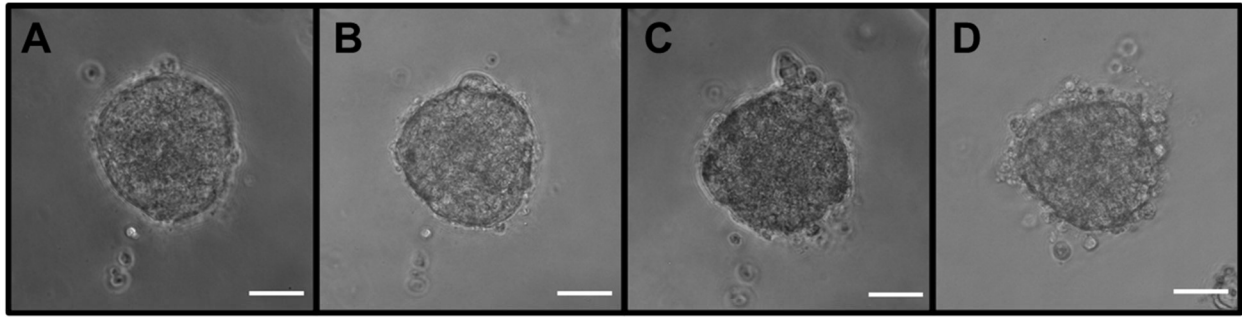


**Figure A.2. Organoid growth in Matrigel Basement Membrane.**

Organoid surface area over time after RT. Data is mean  $\pm$  SEM, N = 4 biological replicates. Scale bars are 50  $\mu$ m.

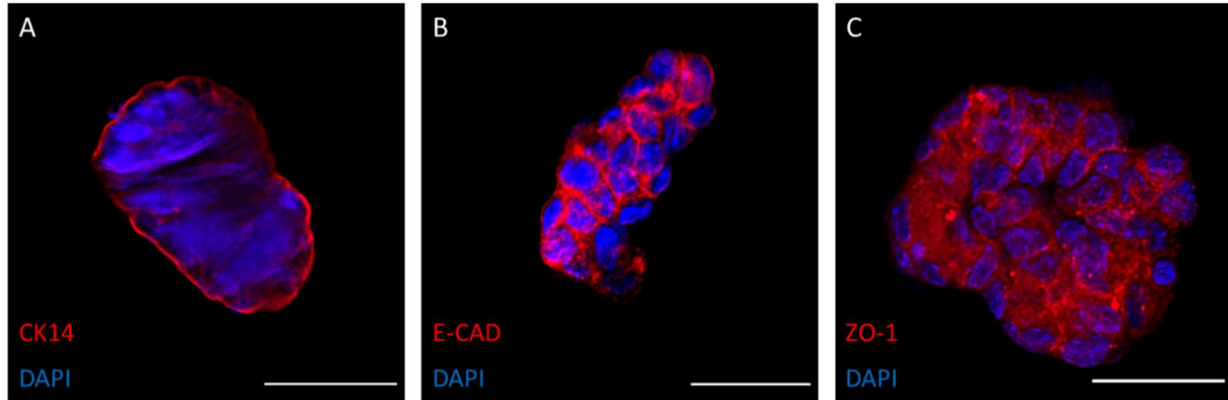


**Figure A.3. Epithelial Marker Expression on Irradiated Organoids.**

Cytokeratin 14 (K14, green), a marker for the basal layer of squamous and non-squamous epithelia, was expressed on irradiated organoids (A). E-cadherin (E-Cad), a protein essential for adhesion, was expressed within the junctions between cells in irradiated organoids (B). Tight junction protein one (ZO-1) was also expressed within cell junctions of irradiated organoids (C). Images were obtained in chamber slides via confocal microscopy. A nucleic acid stain was used to visualize nuclei (blue). All organoids were fixed and imaged after one week of growth. Scale bars are 50  $\mu\text{m}$ .

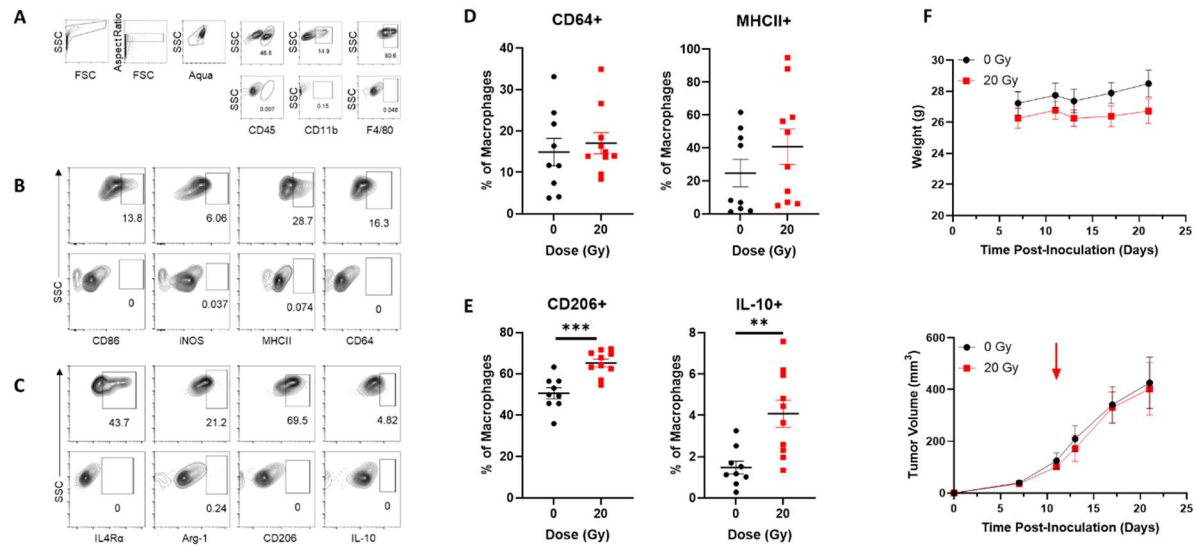


**Figure A.4. Macrophage infiltration in normal tissues 10 days post-RT**

**A.** Flow cytometry gating strategy for infiltrating macrophages in mammary fat pads (MFPs) with unstained controls. Flow cytometry gating strategy for M1 (**B**) and M2 (**C**) macrophages with unstained controls. Quantification of infiltrating F480+ M1 (**D**) and M2 (**E**) macrophages post-RT. Expression of CD64 and MHCII (M1) and CD206 and IL-10 (M2) were quantified. **F.** Mouse weight and tumor volume curves. Arrow indicates time of irradiation. Data is mean  $\pm$  standard error of mean. N=9-10 biological replicates per treatment. \*\*p<0.01 and \*\*\*p<0.001 as determined by a two-tailed unpaired t-test.

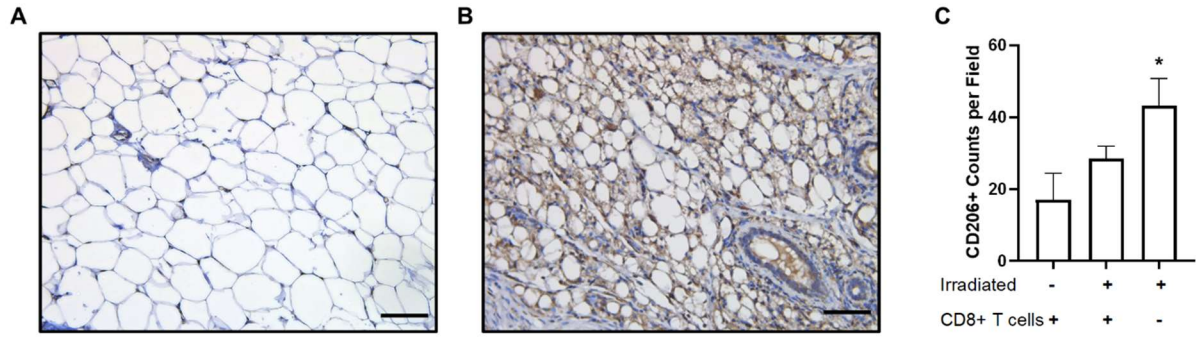


**Figure A.5. M2 Macrophage infiltration is increased 10 days post-RT after CD8+ T cell depletion.**

Bright field images of mammary fat pad sections from **A.** unirradiated, immunocompetent mice and **B.** irradiated immunocompromised mice. **C.** CD206+ cell counts per field. Scale bars are 50  $\mu$ m, data is mean  $\pm$  SEM, \* $p$ <0.05 as determined by ANOVA.

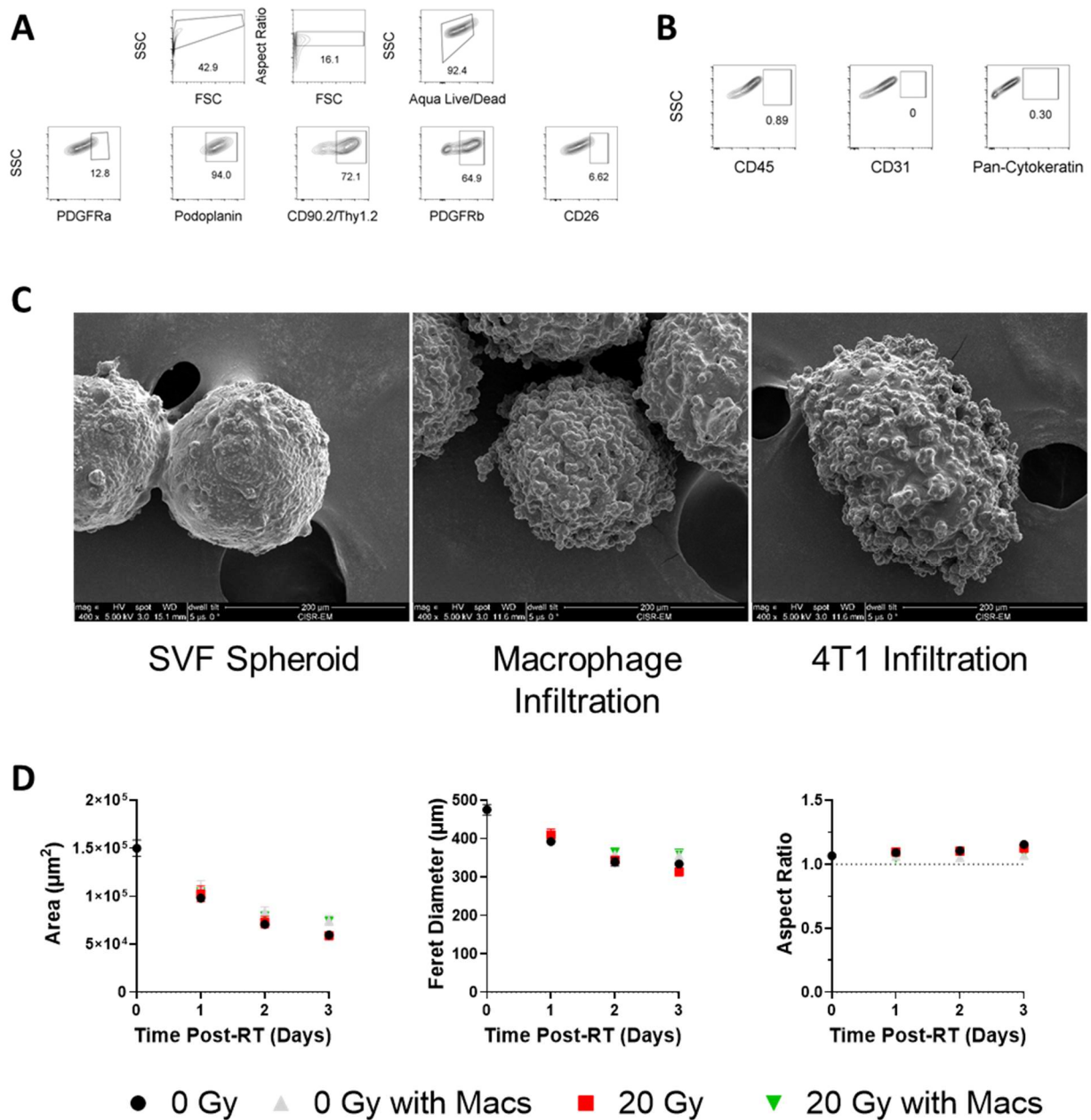


**Figure A.6. SVF organoid characterization.**

**A.** Full gating strategy for SVF markers. **B.** Negligible expression of immune cell, endothelial cell, and epithelial cell markers. **C.** Scanning electron microscopy images of SVF organoids alone, with macrophage infiltration, and with 4T1 infiltration. Images were taken at 400x magnification. **D.** Organoid area ( $\mu\text{m}^2$ ), feret diameter ( $\mu\text{m}$ ), and aspect ratio were quantified. No significant differences were observed after irradiation or with co-culture with macrophages. Data is mean  $\pm$  SEM,  $n=3$  biological replicates.

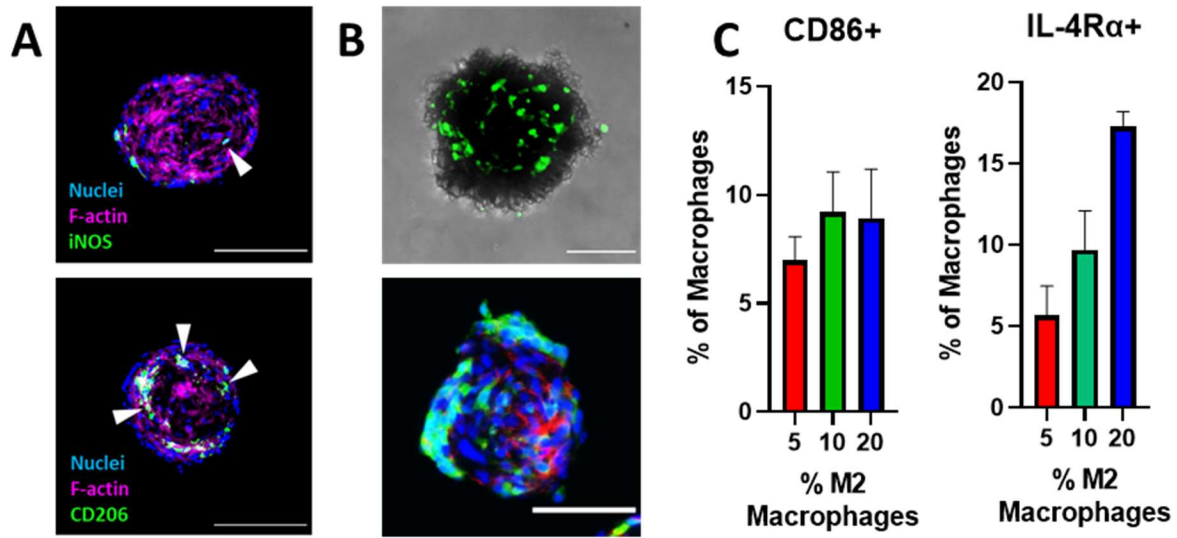


**Figure A.7. Polarized Macrophage and 4T1 Co-Culture Validation.**

**A.** M1 (iNOS) and M2 (CD206) macrophages infiltrate into organoids within 24 hours. F-actin was used to stain the cytoskeleton (magenta). **B.** Confirmation of 4T1 (GFP-labeled) infiltration via live cell imaging. Sections were stained with phalloidin (red) and NucBlue (blue), respectively. Scale bars are 200  $\mu$ m. **C.** Confirmation of expression of M1 and M2 markers 4 days after co-culture (n=3 biological replicates). For **C**, data is mean  $\pm$  standard error of mean, n=3 biological replicates.

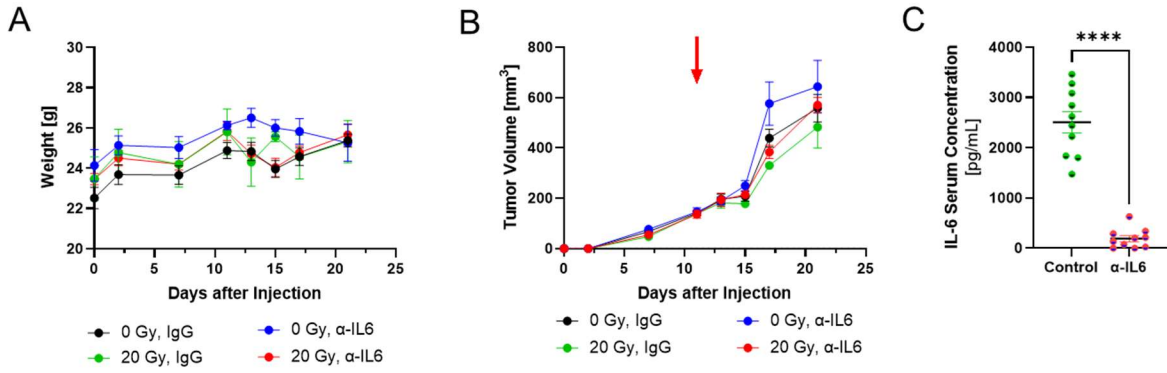


**Figure A.8. In vivo validation of IL-6 depletion model.**

**A.** For *in vivo* experiments, mouse weights (**B**) and tumor curves are shown. Arrow indicates time of irradiation. **C.** Systemic IL-6 depletion was confirmed via ELISA. Data is mean ± standard error of mean. N=4-5 biological replicates per treatment. \*\*\*\*p<0.0001, statistical significance determined by a two-tailed unpaired t-test.

**Table A.1. Table of all proteins analyzed in RPPA.**

| <b>Antibody Name</b> | <b>Gene Name</b> |
|----------------------|------------------|
| 14-3-3-zeta          | YWHAZ            |
| 14-3-3-beta          | YWHAB            |
| 4E-BP1               | EIF4EBP1         |
| 4E-BP1_pS65          | EIF4EBP1         |
| 53BP1                | TP53BP1          |
| A-Raf                | ARAF             |
| ACC1                 | ACACA/ ACACB     |
| ACC_pS79             | ACACA/ACACB      |
| Akt                  | AKT1/2/3         |
| Akt_pS473            | AKT1/2/3         |
| Akt_pT308            | AKT1/2/3         |
| AMPK-a2_pS345        | PRKAA2           |
| AMPKa                | PRKAA1/2         |
| AMPKa_pT172          | PRKAA1/2         |
| AR                   | AR               |
| ARID1A               | ARID1A           |
| Atg3                 | ATG3             |
| Atg7                 | ATG7             |
| ATM                  | ATM              |
| ATM_pS1981           | ATM              |

| <b>Antibody Name</b> | <b>Gene Name</b> |
|----------------------|------------------|
| ATR_pS428            | ATR              |
| Aurora-B             | AURKB            |
| Axl                  | AXL              |
| b-Actin              | ACTB             |
| b-Catenin            | CTNNB1           |
| b-Catenin_pT41_S45   | CTNNB1           |
| B-Raf                | BRAF             |
| B-Raf_pS445          | BRAF             |
| B7-H4                | VTCN1            |
| Bad_pS112            | BAD              |
| Bak                  | BAK1             |
| Bax                  | BAX              |
| Bcl-xL               | BCL2L1           |
| Beclin               | BECN1            |
| Bid                  | BID              |
| Bim                  | BCL2L11          |
| BRD4                 | BRD4             |
| c-Abl                | ABL1             |
| c-IAP2               | BIRC3            |
| c-Jun_pS73           | JUN              |
| c-Kit                | KIT              |

| <b>Antibody Name</b> | <b>Gene Name</b> |
|----------------------|------------------|
| c-Met_pY1234_Y1235   | MET              |
| c-Myc                | MYC              |
| C-Raf                | RAF1             |
| C-Raf_pS338          | RAF1             |
| Caspase-3            | CASP3            |
| Caspase-7-cleaved-   | CASP7            |
| Caveolin-1           | CAV1             |
| CD134                | TNFRSF4          |
| CD20                 | MS4A1            |
| CD4                  | CD4              |
| cdc25C               | CDC25C           |
| cdc2_pY15            | CDK1             |
| CDK1_pT14            | CDK1/2/3         |
| Chk1_pS296           | CHEK1            |
| Chk2_pT68            | CHEK2            |
| Claudin-7            | CLDN7            |
| COG3                 | COG3             |
| Collagen-VI          | COL6A1           |
| Connexin-43          | GJA1             |

| <b>Antibody Name</b> | <b>Gene Name</b> |
|----------------------|------------------|
| Cox-IV               | COX4I1           |
| Cox2                 | PTGS2            |
| Creb                 | CREB1            |
| Cyclin-B1            | CCNB1            |
| Cyclin-D1            | CCND1            |
| D-a-Tubulin          | TUBA4A/TUBA3C    |
| DJ1                  | PARK7            |
| DM-Histone-H3        | HIST1H3A         |
| DUSP4                | DUSP4            |
| E-Cadherin           | CDH1             |
| eEF2                 | EEF2             |
| eEF2K                | EEF2K            |
| EGFR                 | EGFR             |
| EGFR_pY1173          | EGFR             |
| eIF4E                | EIF4E            |
| eIF4E_pS209          | EIF4E            |
| eIF4G                | EIF4G1           |
| Elk1_pS383           | ELK1             |
| ER                   | ESR1             |

| <b>Antibody Name</b> | <b>Gene Name</b> |
|----------------------|------------------|
| ER-a_pS118           | ESR1             |
| ERCC5                | ERCC5            |
| Ets-1                | ETS1             |
| FAK                  | PTK2             |
| FAK_pY397            | PTK2             |
| FASN                 | FASN             |
| Fibronectin          | FN1              |
| FOXM1                | FOXM1            |
| FoxO3a               | FOXO3            |
| FoxO3a_pS318_S321    | FOXO3            |
| G6PD                 | G6PD             |
| Gab2                 | GAB2             |
| GATA6                | GATA6            |
| GCLM                 | GCLM             |
| GCN5L2               | KAT2A            |
| Glutamate-D1-2       | GLUD1            |
| Glutaminase          | GLS              |
| Granzyme-B           | GZMB             |
| GSK-3a-b_pS21_S9     | GSK3A/GSK3B      |

| <b>Antibody Name</b> | <b>Gene Name</b> |
|----------------------|------------------|
| Gys                  | GYS1             |
| Gys_pS641            | GYS1             |
| HER2_pY1248          | ERBB2            |
| HER3                 | ERBB3            |
| HER3_pY1289          | ERBB3            |
| Heregulin            | NRG1             |
| HES1                 | HES1             |
| Hexokinase-II        | HK2              |
| Histone-H3           | HIST3H3          |
| HSP27_pS82           | HSBP1            |
| HSP70                | HSPA1A           |
| IGF1R_pY1135_Y1136   | IGF1R/INSR       |
| IGFBP2               | IGFBP2           |
| IGFRb                | IGF1R            |
| INPP4b               | INPP4B           |
| IR-b                 | INSR             |
| IRF-1                | IRF1             |
| IRS1                 | IRS1             |
| Jagged1              | JAG1             |
| Jak2                 | JAK2             |
| JNK2                 | MAPK9            |

| <b>Antibody Name</b> | <b>Gene Name</b> |
|----------------------|------------------|
| JNK_pT183_Y185       | MAPK8            |
| LC3A-B               | MAP1LC3A/B       |
| Lck                  | LCK              |
| LDHA                 | LDHA             |
| LRP6_pS1490          | LRP6             |
| MAPK_pT202-Y204      | MAPK1/MAPK3      |
| Mcl-1                | MCL1             |
| MCT4                 | SLC16A3          |
| MDM2_pS166           | MDM2             |
| MEK1                 | MAP2K1           |
| MEK1_p_S217-S221     | MAP2K1/MAP2K1    |
| MERIT40_pS29         | BABAM1           |
| Merlin               | NF2              |
| MIF                  | MIF              |
| MMP14-[EP1264Y]      | MMP14            |
| MMP2                 | MMP2             |
| Mnk1                 | MKNK1            |
| MSH6                 | MSH6             |

| <b>Antibody Name</b> | <b>Gene Name</b> |
|----------------------|------------------|
| MSI2                 | MSI2             |
| mTOR                 | MTOR             |
| mTOR_pS2448          | MTOR             |
| Myosin-11            | MYH11            |
| Myosin-IIa_pS1943    | MYH9             |
| Myt1                 | PKMYT1           |
| N-Cadherin           | CDH2             |
| NAPSIN-A             | NAPSA            |
| NDRG1_pT346          | NDRG1            |
| NF-kB-p65_pS536      | RELA             |
| Notch1               | NOTCH1           |
| Notch3               | NOTCH3           |
| Oct-4                | POU5F1           |
| P-Cadherin           | CDH3             |
| p16INK4a             | CDKN2A           |
| p21                  | CDKN1A           |
| p27-Kip-1            | CDKN1B           |
| p27_pT198            | CDKN1B           |

| <b>Antibody Name</b> | <b>Gene Name</b> |
|----------------------|------------------|
| p38-MAPK             | MAPK14/11/12     |
| p38_pT180_Y182       | MAPK11/12/13/14  |
| p44-42-MAPK          | MAPK1/MAPK3      |
| p53                  | TP53             |
| p70-S6K1             | RPS6KB1          |
| p70-S6K_pT389        | RPS6KB1          |
| p90RSK_pT573         | RPS6K            |
| PAICS                | PAICS            |
| PAK1                 | PAK1             |
| PAK4                 | PAK4             |
| PAR                  | PAR              |
| PARP                 | PARP1            |
| Paxillin             | PXN              |
| PD-L1                | CD274            |
| Pcdcd4               | PDCD4            |
| PDHK1                | PDHK1            |
| PDK1                 | PDPK1            |
| PDK1_pS241           | PDPK1            |

| <b>Antibody Name</b> | <b>Gene Name</b> |
|----------------------|------------------|
| PEA-15               | PEA15            |
| PEA-15_pS116         | PEA15            |
| PI3K-p110-a          | PIK3CA           |
| PI3K-p85             | PIK3R1           |
| PKA-a                | PRKAR1A          |
| PKC-b-II_pS660       | PRKCA/B/D/E/H/Q  |
| PKC-delta_pS664      | PRKCD            |
| PKCa                 | PRKCA            |
| PKM2                 | PKM              |
| PLC-gamma2_pY759     | PLCG2            |
| PLK1                 | PLK1             |
| PMS2                 | PMS2             |
| PR                   | PGR              |
| PRAS40_pT246         | AKT1S1           |
| PREX1                | PREX1            |
| PTEN                 | PTEN             |
| Rab11                | RAB11A/B         |

| <b>Antibody Name</b> | <b>Gene Name</b> |
|----------------------|------------------|
| Rab25                | RAB25            |
| Rad50                | RAD50            |
| Rad51                | RAD51            |
| Raptor               | RPTOR            |
| RBM15                | RBM15            |
| Rb_pS807_S811        | RB1              |
| Rictor               | RICTOR           |
| Rictor_pT1135        | RICTOR           |
| RIP                  | RIP              |
| RPA32_pS4-S8         | RPA2             |
| RSK                  | RPS6KA1/2/3      |
| S6_pS235_S236        | RPS6             |
| S6_pS240_S244        | RPS6             |
| SDHA                 | SDHA             |
| Shc_pY317            | SHC1             |
| SHP-2_pY542          | PTPN11           |
| SLC1A5               | SLC1A5           |
| Slfn11               | SLFN11           |

| <b>Antibody Name</b> | <b>Gene Name</b> |
|----------------------|------------------|
| Smad1                | SMAD1            |
| Smad3                | SMAD3            |
| SOD2                 | SOD2             |
| Sox2                 | SOX2             |
| Src_pY419            | SRC              |
| Src_pY527            | SRC              |
| Stat3                | STAT3            |
| Stat3_pY705          | STAT3            |
| Stat5a               | STAT5A           |
| Stathmin-1           | STMN1            |
| STING                | TMEM173          |
| TAZ                  | WWTR1            |
| TFAM                 | TFAM             |
| TFRC                 | TFRC             |
| TIGAR                | TIGAR            |
| TRIM25               | TRIM25           |
| TSC1                 | TSC1             |
| TTF1                 | NKX2-1           |
| Tuberin              | TSC2             |
| Tuberin_pT1462       | TSC2             |
| TUFM                 | TUFM             |

| <b>Antibody Name</b> | <b>Gene Name</b> |
|----------------------|------------------|
| Tyro3                | TYRO3            |
| U-Histone-H2B        | HIST1H2BB        |
| UBAC1                | UBAC1            |
| ULK1_pS757           | ULK1             |
| VASP                 | VASP             |
| VEGFR-2              | KDR              |
| Wee1                 | WEE1             |
| Wee1_pS642           | WEE1             |
| WIPI1                | WIPI1            |
| WIPI2                | WIPI2            |
| XBP-1                | XBP1             |
| XPF                  | ERCC4            |
| XRCC1                | XRCC1            |
| YAP                  | YAP1             |
| YAP_pS127            | YAP1             |
| YB1_pS102            | YBX1             |
| ZAP-70               | ZAP70            |

**Table A.2. Table of cytokine abbreviations**

|                       |  |
|-----------------------|--|
| GSCF/CSF3             | Granulocyte colony-stimulating factor                                      |
| GMCSF                 | Granulocyte-macrophage colony-stimulating factor                           |
| GROA / GRO $\alpha$   | Growth-regulated alpha protein   |
| IFNA / IFN $\alpha$   | Interferon alpha   |
| IFNG / IFN $\gamma$   | Interferon gamma   |
| IL10                  | Interleukin 10   |
| IL12P70               | Interleukin 12p70  |
| IL13                  | Interleukin 13   |
| IL15/IL15R            | Interleukin 15/Interleukin 15R   |
| IL17A / IL17 $\alpha$ | Interleukin 17A  |
| IL18                  | Interleukin 18   |
| IL1A / IL1 $\alpha$   | Interleukin 1 alpha  |
| IL1B / IL1 $\beta$    | Interleukin 1 beta   |
| IL2                   | Interleukin 2  |
| IL22                  | Interleukin 22   |
| IL23                  | Interleukin 23   |
| IL27                  | Interleukin 27   |
| IL28                  | Interleukin 28   |
| IL3                   | Interleukin 3  |
| IL31                  | Interleukin 31   |
| IL4                   | Interleukin 4  |
| IL5                   | Interleukin 5  |
| IL6                   | Interleukin 6  |
| IL9                   | Interleukin 9  |
| IP10                  | Interferon gamma-induced protein 10  |
| KC                    | Keratinocyte-derived chemokine   |
| LIF                   | Leukemia inhibitory factor   |
| LIX                   | Lipopolysaccharide-induced CXC chemokine                                   |
| MCSF                  | Macrophage colony-stimulating factor                                       |
| MCP1                  | Monocyte chemoattractant protein-1   |
| MCP3                  | Monocyte chemotactic protein-3   |
| MIG                   | Monokine induced by gamma interferon                                       |
| MIP1A / MIP1 $\alpha$ | Macrophage inflammatory protein-1 alpha                                    |
| MIP1B / MIP1 $\beta$  | Macrophage inflammatory protein-1 beta                                     |
| MIP2                  | Macrophage inflammatory-2  |
| RANTES                | Regulated upon Activation, Normal T cell Expressed and Presumably Secreted |
| TGFB / TGF $\beta$    | Transforming growth factor beta  |
| TNFA / TNF $\alpha$   | Tumor necrosis factor alpha  |
| VEGF                  | Vascular endothelial growth factor   |

## APPENDIX B – Code

```
Clear all
Image_count=16; %edit with each data set for number of images within set
Imtool(calibration_image)
Bar= ; %insert value of scale bar in real life length
Scale_factor=bar/pixels; %um/pixels
C=[ ];
Average_value=[ ];
For i=[1:image_count]
url_bw= "GRAY IMAGE FOLDER" + num2str(i) + ".tif"
url_gfp= "GREEN IMAGE FOLDER" + num2str(i) + ".tif"
image_bw=imread(url_bw);
image_gfp=imread(url_gfp);
imshow(image_bw);
e = drawcircle('FaceSelectable');
wait(e);
bw = createMask(e)
%imshow(bw);
s = regionprops(bw, { ...
'Centroid'
'MajorAxisLength', ...
'MinorAxisLength', ...
'Orientation' });
t = linspace(0,2*pi,50); %angular displacement increments for scanning organoid; takes samples
along 50 radial segments
a = s(1).MajorAxisLength/2;
b = s(1).MinorAxisLength/2;
Xc = s(1).Centroid(1);
Yc = s(1).Centroid(2);
Fluorescence_matrix=[ ];
N=1000; %number of points sampled along each radial segment
For j=t
X = Xc + a*cos(j);
Y = Yc + b*sin(j);
Xi=[Xc x];
Yi=[Yc y];
[cx,cy,c,xi2,yi2] = improfile(image_gfp,xi,yi,n);
%green_pixels-c, if your Tiff image has just one channel, use this command
Green_pixels=c(:,2); %works with green channel; 1 is R, 2 is G, and 3 is blue
Green_pixels=green_pixels;
Fluorescence_matrix=[fluorescence_matrix;green_pixels]; %each row corresponds with a line
segment
```

```

End
Mean_profile=mean(fluorescence matrix);
Distances=[a/n:a/n:a]*scale_factor; %convert pixel values from arbitrary units to microns across
sampled radial segments for the organoid
Distance_intensity_matrix= [distances; fluorescence_matrix]; %concatenate average fluorescence
and corresponding radial distance to get x-y pairs in one matrix
Distance_intensity_matrix=distance_intensity_matrix';
C=[C;distance_intensity_matrix]; %add the x-y pairs for the organoid to the end of ongoing data
table for the image set
Close
End
Filename = "OUTPUT FOLDER"; %url to excel sheet for data output
Sheet = 12;
xlRange = 'G3'; %A3 D3 G3 J3 M3 P3 S3 V3 Y3 AB3 AE3 AH3
xlswrite(filename,C,sheet,xlRange)

```

**Figure B.1. Custom script used to analyze the intensity of a fluorophore as a function of distance from the center of a organoid.**

Along the radial axis, 1,000 readings of fluorescent intensity are evaluated over every angle of each organoid. Readings are normalized to the overall length of each radius to generate relative intensity values.

```

dir1 = getDirectory("Choose directory where images are located");
dir2 = getDirectory("Choose directory where to save montages");

list = getFileList(dir1);
num=list.length;

//determine the thresholding parameters for the phase image

min=65;
max=255;

i = 0;
while (i < num)

{

//first open all channels for the image and rename them to get rid of the ".tif" at the end

open(dir1 + list[i]);
title1=getTitle();
title2=replace(title1, ".tif", "");
rename(title2);
//rename("DAPI");
open(dir1 + list[i+1]);
title3=getTitle();
title4=replace(title3, ".tif", "");
rename(title4);
//rename("GFP");
open(dir1 + list[i+2]);
title5=getTitle();
title6=replace(title5, ".tif", "");
rename(title6);
//rename("TXR");

//duplicate the DAPI image and convert the duplicate to binary, using the thresholding parameters
from above

selectWindow(title2);
run("Duplicate...", " ");
//setMinAndMax(0, 100);
//run("Apply LUT");
setAutoThreshold("Default dark");
setThreshold(min, max);
setOption("BlackBackground", false);
run("Convert to Mask");
run("Fill Holes");

```

```
run("Set Measurements...", "area mean integrated area_fraction display redirect=None  
decimal=3");
```

```
//create the ROI from the DAPI channel
```

```
setTool("wand");  
selectWindow(title2 + "-1");  
//doWand(1260, 992);  
waitForUser("select ROI with wand, then hit ok");  
roiManager("Add");
```

```
//Apply the ROI to other channel(s) and measure the intensity within
```

```
selectWindow(title6);  
roiManager("Select", 0);  
roiManager("Measure");  
run("Flatten");  
roiManager("Deselect");
```

```
//label DAPI with the thresholding values
```

```
selectWindow(title2 + "-1");  
setFont("SansSerif", 80, "antialiased");  
setColor("black");  
drawString("Threshold " + min + " min: " + min + " max: " + max, 960, 174);  
roiManager("Select", 0);  
roiManager("Measure");  
run("Flatten");  
roiManager("Deselect");
```

```
//Delete ROI so you can create a new one for the next image
```

```
roiManager("Select", 0);  
roiManager("Delete");
```

```
//create a montage of images to be able to visually double check ROI's later
```

```
selectWindow(title2 + "-1");  
close();  
selectWindow(title6);  
close();  
run("Images to Stack", "use");  
run("Make Montage...", "columns=4 rows=1 scale=0.25");  
saveAs("Jpeg", dir2 + title6 + " montage");  
close();  
selectWindow("Stack");  
close();
```

```
run("Close All");  
i=i+3;  
  
}
```

```
selectWindow("Results");  
saveAs("Text...", dir2+ "Excel" + ".xls");
```

**Figure B.2. Custom script used to analyze the intensity of a fluorophore within an ROI.**

It first creates an ROI using the dapi channel of a organoid. It then applies that ROI to the fluorescent channel and evaluates intensity and other parameters. It only does it for one fluorescent ROI; however, it is easy to add additional channels. It will label the thresholding values on the montage.

```

dir1 = getDirectory("Choose directory where images are located");
dir2 = getDirectory("Choose directory where to save montages");
list = getFileList(dir1);
num=list.length;
i = 0;
while (i < num)
{
//first open the image and rename it to get rid of the ".tif" at the end
open(dir1 + list[i]);
title1=getTitle();
title2=replace(title1, ".tif", "");
rename(title2);
//duplicate the phase image and convert the duplicate to binary
selectWindow(title2);
run("Duplicate...", " ");
//setMinAndMax(0, 100);
//run("Apply LUT");
setAutoThreshold("Default");
//setThreshold(0, 90);
setOption("BlackBackground", false);
run("Convert to Mask");
run("Fill Holes");
run("Set Measurements...", "area perimeter shape feret's skewness display redirect=None
decimal=3");
//create the ROI from the Phase channel and measure the Area
setTool("wand");
selectWindow(title2 + "-1");
waitForUser("select ROI with wand, then hit ok");
run("Measure");
//create a montage of images to be able to visually double check thresholding later
run("Images to Stack", "use");
run("Make Montage...", "columns=2 rows=1 scale=0.25");
saveAs("Jpeg", dir2 + title2 + " montage");
close();
selectWindow("Stack");
close();
run("Close All");
i=i+1;
}
selectWindow("Results");
saveAs("Text...", dir2+ "Excel" + ".xls");

```

**Figure B.3. Custom script used to measure organoid area by creating an ROI using the phase channel of a organoid.**

## APPENDIX C – Protocols

### Protocol C.1. Flow Cytometry Sample Prep for Mammary Fat Pads

#### Materials:

#### On a per fat pad basis:

- RPMI with 10% FBS
    - 5 mL per fat pad
  - PBS with 3% FBS
    - 35 mL per fat pad
  - PBS with 1% FBS
    - 10 mL per fat pad
  - 6 well plate or 6 cm dishes per fat pad w/ 1 mL RPMI/10%FBS for transporting
  - 6 well plate or 6 cm dishes per fat pad
  - 6 cm dishes per fat pad w/ 1 mL 1% FBS/PBS
  - 50 mL tube labeled dig per fat pad
  - 50 mL tube labeled filt per fat pad
- 
- All solutions kept on ice or at 4°C, unless otherwise noted
  - 1% FBS in PBS (500 mL) – Alternative: RPMI or DMEM with 10% FBS
    - PBS (without Ca/Mg) (495 mL)
    - 1% FBS (5 mL of 100% FBS)
  - FACS Buffer (500 mL)
    - PBS (without Ca/Mg) (493 mL)
    - 1% FBS (5 mL of 100% FBS)
    - 2 mM EDTA (2 mL of 0.5 M stock)
  - Collagenase solution
    - 4mg/mL Type II collagenase in 1% FBS in PBS (need 3 mL per sample)
    - Product #: C6885 from SIGMA
    - Optional: 0.25 mg/mL DNaseI

#### Method:

1. Sacrificed mouse
  1. Placed 2-3 droppers full of isofluorane to anesthesia chamber. Waited  $\geq 1$  minute, added mouse to chamber. Waited 2-5 minutes, cervically dislocated mouse.
  2. Perfused animal via left ventricle of heart with 10-20 mL PBS, immediately after clipping aorta/right atrium
2. Collected AT
  1. Isolated AT
  2. Placed AT (if  $\geq 1.2$  g, then split depot) in weigh boat on ice and submerged with 1 mL 1% FBS in PBS
  3. Minced tissue thoroughly with scissors (to a slurry,  $\sim 1$  min of mincing) and transferred to 50 mL conical tube
  4. Rinse remaining tissue from weigh boat into 50 mL conical tube (on ice) with 2 mL 1% FBS in PBS.

3. Repeated @1.) & 2.) for remaining mice
4. Collagenase (Sigma) digestion
  1. Added equal volume (3 mL) of 4 mg/mL collagenase solution to minced tissue suspension; [final] = 6 mL solution @2 mg/mL
  2. Incubated 30 min on heated shaker @200 rpm @37°C
    1. If heated shaker is not available, then incubate @37°C and shake by hand every 5 min
  3. Added 10 mL 1% FBS in PBS and placed on ice. Vortex well for 3-5 seconds
  4. Passed cell suspension through 100 micron filter into new 50 mL conical tube
5. Count Cells using MACSQuant 10 Cytometer (or other cell counter)
  1. Centrifuge samples 8 min at 500 RCF at 4°C, discard supernatant.
  2. Resuspend in 5 mL PBS 3% FBS.
  3. Count cells using automated cell counter. Add PBS/3% FBS as necessary to end up with a final density of around 1-5 million cells per tube
  4. Pipet cells into microcentrifuge tubes.
  5. Spin down at 500 RCF for 8 minutes. Resuspend in antibody cocktail to stain for surface markers.
6. Wash by adding 100 uL PBS, pipette up and down
7. Spin down the plate (1400 rpm, 3 min, 4°C); flick off liquid
8. Resuspend in 200 uL facs buffer (PBS/3%FBS) -or- 100 uL fixative (1:10 dilution of formalin in PBS) (depends on if you're running the samples now or later)
9. Leave cells at 4°C until flow cytometry analysis
  1. If fixing, can leave up to 1 week at 4°C in fixative
  2. Ready to run the sample: add 100 uL of PBS with a mutli-channel pipette and mix up and down to wash; spin down the plate; remove supernatant, and resuspend in 200 uL PBS before running the samples.
10. When analyzing, prepare compensation controls (beads), and move the unlabeled and live/dead only stained cells from the plate into microcentrifuge tubes for compensation.

### Intracellular Staining

Perm buffer: 1 part concentrated buffer (ThermoFisher), 9 parts DI water

Need 550 uL per well

If you have not done it already, fix cells in diluted formalin (1:10 in 1x PBS). Put in fridge for at least 20 minutes (can be stored for a few days).

1. Wash fixative with 100 uL of PBS.
2. Spin down at 1400 RPM, 3 minutes. Flick off.
3. Add 200 uL perm buffer for five minutes at RT.
4. Spin down, flick off.
5. Add 50 uL of ab cocktail per well, with antibodies diluted in the perm buffer.
6. Incubate for 30 minutes at RT in the dark/in foil.
7. Add 100 uL of perm buffer and wash.

8. Spin down, flick off.
9. Resuspend in 200 uL of perm buffer.
10. Spin down, flick off.
11. Resuspend in 50 uL of PBS. Run on the Cell Stream.

## Protocol C.2. Stromal Vascular Fraction Organoids

### Materials

1. Maintenance media: DMEM/20% BCS/1% PS
  - a. DMEM: 11995-065
  - b. BCS: Bovine Calf Serum
  - c. PS: Penstrep, 15140-122
  - d. To make maintenance media, get a new bottle of DMEM. Add 5 mL of PS. Mix well. Remove 100 mL of media. Add 100 mL of Bovine Calf Serum.
2. Trypsin: 25200-056

### Timeline

| Days Post Isolation | 0 Days         | 5-7 days                      | 10-12 days                    | 14-15 days           |
|---------------------|----------------|-------------------------------|-------------------------------|----------------------|
| Action              | Cell Isolation | Passage, expand               | Passage, expand               | Plate into organoids |
|                     | Cells are "p0" | After passage, cells are "p1" | After passage, cells are "p2" |                      |

## Cell isolation

*Approximate time: 2 hours*

1. Sacrifice a mouse. Resect its #4 mammary fat pads (both left and right side) and place in a 50 mL conical tube with 10 mL complete DMEM (DMEM/10% FBS/1% PS). Transport on ice back to Rafat lab.
2. Spray down with 70% EtOH, and bring into TC hood. Transfer fat pad to 50 mL conical tube with 10 mL PBS to rinse. Then, place in large weigh boat.
3. Chop up fat pad with a razor or scissors.
4. Transfer chopped up chunks into a new 50 mL conical tube with 10 mL PBS. Add 100 uL PS and liberase so that final liberase concentration is 0.2125 mg/mL. All of these are per mouse – so if you are combining fat pads from multiple mice into one tube, then multiply by the number of mice
5. Example calculations:

| Initial aliquot concentration (mg/mL) | Volume of liberase aliquot to add per 10 mL PBS (uL) |
|---------------------------------------|--|
| 2.5                                   | 85   |
| 5                                     | 42.5   |

6. Gently vortex, then place in water bath to digest. Vortex gently every ten minutes. Digest for a total of 45 minutes.
7. After digestion is complete, add 10 mL maintenance media to digestion cocktail to inhibit enzymes. Pour digestion cocktail through a 100 um filter (yellow filter) into a new 50 mL conical tube. Use the back of a 1mL/5mL syringe plunger to crush tissue on the filter, then rinse with 10 more mL of maintenance media.
8. Spin down at 1100 RPM for 5 min.
9. Aspirate media. Resuspend in 6 mL of maintenance media. Split into two 6 cm dishes.
10. 24 hours post plating, change media. Continue to change media every other day.

Scaling up – for large experiments, combine fat pads from multiple mice

|                                |      |     |       |
|--------------------------------|------|-----|-------|
| Number of mice                 | 1    | 2   | 3     |
| mL liberase digestion solution | 10   | 20  | 30    |
| uL P/S                         | 100  | 200 | 300   |
| uL Liberase                    | 42.5 | 85  | 127.5 |
| Number of 6 cm dishes          | 2    | 4   | 6     |
| mL maintenance media           | 6    | 12  | 18    |

## Expanding cells

*Approximate time: 1 hour*

| Plate size | mL PBS rinse per plate | mL Trypsin per plate | mL complete media per plate to stop trypsinization |
|------------|------------------------|----------------------|--|
| 6 cm       | 5                      | 1                    | 3  |
| 10 cm      | 10                     | 2                    | 5  |

1. 5-7 days post plating, cells will be ready to passage for expansion. Aspirate media and rinse with PBS. Gently swirl plate with PBS and aspirate. Add Trypsin and incubate at 37C for 7 minutes. After 7 minutes, check cells on microscope to confirm that they have lifted off from the plate. Bring back into hood and add 5 mL maintenance media. Use cell scraper to get residual cells. Combine cell suspension from both plates. Spin down at 1100 RPM for 5 min. Resuspend in 20 mL maintenance media. Plate into 2 10 cm dishes.
2. 3-5 days post passaging, split cells again into 8 plates. Aspirate media and rinse with PBS. Gently swirl plate with PBS and aspirate. Add Trypsin and incubate at 37C for 7 minutes. After 7 minutes, check cells on microscope to confirm that they have lifted off from the plate. Bring back into hood and add 5 mL maintenance media. Use cell scraper to get residual cells. Combine cell suspension from both plates into a 15 mL tube (should be a total of 14 mL). Spin down at 1100 RPM for 5 mins. Resuspend in 10 mL maintenance media. Pipette up and down 7 times to resuspend the cells well. Get two 50 mL centrifuge tubes. Transfer 5 mL of the cell suspension into each tube. Add 35 mL of maintenance media into each tube. Tubes should contain 5 mL of cell suspension + 35 mL maintenance media. Pipette up and down 7 times in each tube to resuspend the cells well. Pipette 10 mL of this new cell suspension per 10 cm dish (8 dishes total). Cells should be ready 3-5 days post-split.

## Plating into organoids

*Approximate time: 1.5 hours*

1. If a TC hood is open, spray down multichannel pipet and place under UV for at least 30 minutes. If not, spray down with EtOH before bringing into hood.
2. Passage cells as described above. After trypsinizing and spinning down, resuspend cells in 2 mL of maintenance media. Resuspend well. Add 20 uL of cell suspension to a microcentrifuge tube. Combine with 20 uL of Trypan blue and mix well. Add 10 uL into an automatic cell counting chamber, and quantify cell density using the automated cell counter. Record live cell density and viability for two replicates.
3. Add media to adjust live cell density to 1e5 live cells/mL.

4. Pour cell suspension into new sterile reservoir. Use multichannel pipet to transfer 100 uL of cell suspension/well into wells of a 96 well U bottom sphera (low adhesion) plate. Allow at least 16 hours for cells to form organoid.

Irradiating

*Approximate time: 3 hours*

1. Place relevant media in the water bath to warm it up. Transport cells to the irradiator in a Styrofoam container.

Notes:

- a. 3D irradiation can be performed no sooner than 16 hours post plating into organoids. The maximum dose that can be used is 20 Gy. Immediately after 3D irradiation, media must be changed.
  - b. 2D irradiation can be performed 3-5 days post 2<sup>nd</sup> split of cells. The maximum dose that can be used is 10 Gy. Immediately after 2D irradiation, cells must be passaged into organoids with BMDMs.
2. Irradiate to the desired dose.
  3. Transport cells back to the tissue culture hood. Spray down plate with ethanol.
  4. Under sterile conditions, gently add media to each well.
    - a. Use a multichannel pipet (spray down with EtOH before bringing into TC hood) and a sterile reservoir.
    - b. Pour some of the fresh media (DMEM/2% BCS/1% PS) into the sterile reservoir.
    - c. Have another reservoir for waste media.
    - d. Tilt plate so that left side is slightly below the right side.
    - e. Do this one biological replicate at a time. I.e, Add media to all wells for one biological replicate. Then, remove the media as in step two below. Dispose of media that has touched the organoids in the waste reservoir. After removing media from all the wells for the one biological replicate, replace the pipet tips with clean ones.

Add/remove media in the following order:

| Step | Instruction         | Total media in well (uL) | % original media |
|------|---------------------|--------------------------|------------------|
| 1    | Add 200 uL media    | 300                      | 33               |
| 2    | Remove 200 uL media | 100                      | 33               |
| 3    | Add 200 uL media    | 300                      | 5.5              |
| 4    | Remove 200 uL media | 100                      | 5.5              |

|    |                  |     |     |
|----|------------------|-----|-----|
| 5* | Add 100 uL media | 200 | <2% |
|----|------------------|-----|-----|

\*Note: for step 5, to do co-culture with both SVF and macrophages, add macrophages at appropriate density so that they make up ~15% of all of overall cells.

5. Incubate at 37C/5% CO2 for desired time point.

### **Protocol C.3. Bone Marrow Derived Macrophage Isolation**

Materials:

SF media: just IMDM (12440053)

Complete media: IMDM, 1% PS, 10% FBS

1. Add 5 mL of Penstrep to 500 mL IMDM. Mix well.
2. Remove 50 mL of media and aliquot into a 50 mL conical tube.
3. Add 50 mL Heat Inactivated FBS.
4. Mix well, then sterile filter into a sterile glass bottle.

Note: Do not add MCSF to the complete media until you are plating the cells. Only add MCSF to the cell suspension; if you add it to the main bottle it will eventually go bad.

BMDM diff media: IMDM, 10 ng/mL MCSF, 1% PS, 10% FBS

10 mL complete IMDM

10 uL MCSF (aliquots stored at 10 ug/mL)

When isolating the bones:

1 50 mL tube w/ ~30 mL of 70% EtOH

1 50 mL tube w/ ~30 mL complete IMDM media per mouse

Further processing:

Plenty of SF IMDM media

2 mL ACK lysis buffer per mouse

25 mL complete media per mouse

10 mL BMDM diff media per mouse, plus extra for doing dilutions

Ice bucket

## Day 0 – Isolation and Plating

*Approximate time: 2 hours for one mouse, plus 30 minutes for each additional mouse*

- 1) Isolate femurs from one mouse (unless otherwise specified); remove as much muscle and skin as possible; **place isolated femurs in 70% EtOH for a minute**. Then, transfer to tube with IMDM media
- 2) cut each end of the femur, and flush the bone marrow into a tube containing IMDM media. Flush until the bones are a lot lighter. If you notice large chunks of bone/tissue, filter the bone marrow suspension through a 45  $\mu$ M filter. Make sure to rinse the filter really well to increase yield.
  - a. Alternatively, crush bones in mortar with 5-10 ml of IMDM media; collect media and filter through a 45  $\mu$ M filter
- 3) Spin tubes for 5 minutes at 1300 rpm
- 4) Aspirate supernatant, add 2 ml (per mouse) of ACK lysis buffer, leave for  $\sim$ 2 min at RT
- 5) Add 20 mL complete media to stop reaction
- 6) Spin tubes for 5 minutes at 1300 rpm
- 7) Aspirate supernatant, resuspend pellet in 5 ml of IMDM media
- 8) Count cells
- 9) Adjust cell density to  $5e4$ - $5e5$  cells/mL (typically use **1e5 cells/mL**). Aliquot 10 mL of cell suspension
- 10) n/desired plate into a centrifuge tube.
- 11) Add 10  $\mu$ L of MCSF aliquot (aliquot is 10  $\mu$ g/mL, final conc will be 10 ng/mL) per desired plate to the complete media.
- 12) Seed plates
  - a. Plates should be non-tc treated
- 13) Incubate at 37 C for 7 days
  - a. Do not change media or add anymore M-CSF

Day 7

*Passaging cells – approximate time: 45 mins*

At this point, cells have adopted an “M0” phenotype, with over 95% positive expression of CD11b and F4/80. To harvest M0 macrophages, do the following:

- 1) Aspirate media, rinse with PBS
- 2) Aspirate PBS, add 3 ml of TrypLE, incubate for 5 min at 37 C
- 3) Wash cells with TrypLE 20 times (pipet up and down).
- 4) Add 7 ml of complete IMDM to inactivate TrypLE
- 5) Use a cell scraper to dissociate cells and collect media (can wash plates with media to collect any remaining cells)
- 6) Spin at 1100 rpm for 5 min
- 7) Aspirate supernatant
- 8) Resuspend in 13 ml of media (cells are ready to be used for experiment at this point)

*Polarizing cells – approximate time: 45 mins*

Macrophages can be polarized to an M1 and M2 phenotype. To do BMDM polarization:

- 1) Aspirate media, rinse w/ PBS.
- 2) Polarize cells. M1 and M2 polarization protocols require different time points. If you want both M1 and M2 macrophages ready for experiments at the same time, you will have to stagger the time that you add the cytokines.
- 3) When prepping media, make sure that cytokines are well resuspended in the polarizing media.

For M1 macrophages, add M1 media to cells. M1 media consists of:

- a. 10 mL complete media
- b. 100 ng/mL LPS
  - i. Aliquot conc: 100 ug/mL
  - ii. Volume aliquot/10 mL complete media: 10 uL
- c. 50 ng/mL IFN-gamma
  - i. Aliquot conc: 100 ug/mL
  - ii. Volume aliquot/10 mL complete media: 5 uL
- d. 10 ng/mL MCSF
  - i. Aliquot conc: 10 ug/mL
  - ii. Volume aliquot/10 mL complete media: 10 uL

Incubate for 48 hours. Cells should express high levels of iNOS on Day 9.

For M2 macrophages, add M2 media to cells. M2 media consists of:

- e. 10 mL complete media
- f. 10 ng/mL IL-4
  - i. Aliquot conc: 100 ug/mL

- ii. Volume aliquot/10 mL complete media: 1 uL
- g. 10 ng/mL MCSF
  - i. Aliquot conc: 10 ug/mL
  - ii. Volume aliquot/10 mL complete media: 10 uL

Polarize for 48 hours. Cells should express high levels of CD206 and Arg-1 on Day 9.

Passaging should be the same for polarized macs as it is for M0 BMDMs.

Cells can also just be maintained as M0 macrophages, and they will maintain strong CD11b and F4/80 expression for a couple weeks. Just change the media once a week. Continue to use complete IMDM media with MCSF.

#### Protocol C.4. CD8+ T cell isolation, activation, and expansion

Adapted from Miltenyi

Procedure:

\*Remember to minimize spin steps, because you lose about 10% of your cells with every spin\*

##### Creating a single-cell solution from a mouse spleen

**Note: to increase yield, isolate cells from lymph nodes as well.**

1. Bring tube of MACS buffer out of fridge so that it is at room temperature for the isolation.
2. Harvest spleen from immunocompetent mouse. Transport over in RPMI/10% FBS on a 6 or 10 cm plate.
3. Rinse with cold PBS. Place spleen on a strainer (40  $\mu$ m) attached to a 50 mL tube.
4. Press the excised spleen through using a syringe plunger
5. Wash the cells through the strainer with excess PBS, and remember to wash the plunger. Try to get at the bottom of the strainer, too (I usually wash up to 5ml)
6. Centrifuge at 1,600 rpm for 5 min (red pellet); aspirate supernatant
7. Add 1mL of ACK lysis buffer for 1 minute. Inactivate with 19 mL RPMI/10% FBS. Spin down at 1600 rpm for 5 min and resuspend in RPMI/10% FBS.
  - a. Use the automated counter to count. Do not use trypan blue. Adjust counter to suit spleen cells- between 4um and 16um- you will count each mouse spleen separately
  - b. The tech support at Miltenyi claims to get around 80-100 million cells pre-isolation.

Separating CD8+ T cells from the other cells

##### Prepare the reagents

- MACS Buffer – it is okay to use old buffer, there is no need to check the pH unless you are troubleshooting
  - PBS pH 7.2,
  - 0.5% bovine serum albumin (BSA)
  - 2 mM EDTA
  - Degas buffer before use, as air bubbles could block the column.
    - This is not totally necessary- you can use an Erlenmeyer with a vacuum port or one of the vacuum filtration systems for making media and leave it on vacuum for 30 minutes
  - Check pH- EDTA requires the pH to be about 8 to be soluble, but the buffer needs to be at about 7.4 to be effective

##### Manual Magnetic Labelling

**Note: Perform all incubations in the fridge and NOT on ice!**

**The binding kinetics are lower on ice, and you get a lot more cell death.**

1. Keep cells cold and use pre-cooled solutions
2. Volumes given are for up to  $10^7$  total cells. If you have more, scale accordingly (see table)
3. Spin cells down and resuspend pellet (get rid of clump) in 40uL of buffer (per  $10^7$  total cells). Keep the cells in the 50 mL tube.
4. Add 10 uL of Biotin-Antibody Cocktail (per  $10^7$  cells)

5. Mix well and incubate at 4degC for 5 min
6. Add 30uL of buffer (per 10<sup>7</sup> total cells)
7. Add 20uL of Anti-biotin microbeads (per 10<sup>7</sup> total cells)

Mix well and incubate for 10 min at 4 degC

### Manual Magnetic Separation

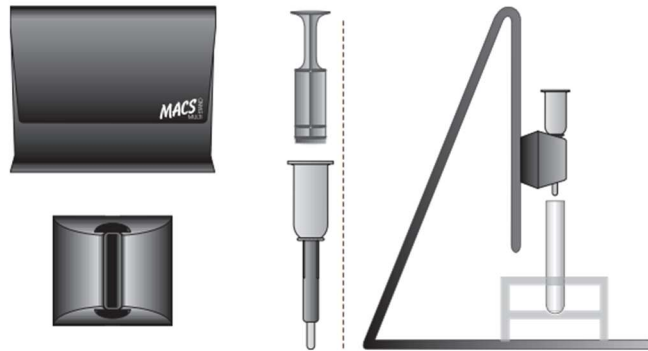
| Column | Max. number of labeled cells | Max. number of total cells | Separator            |
|--------|------------------------------|----------------------------|----------------------|
| LS     | 10 <sup>8</sup>              | 2×10 <sup>9</sup>          | MidiMACS, QuadroMACS |

- Cells should be at 10<sup>8</sup> total cells in

500uL

- Place **LS** column in the magnetic field of the MACS separator, as depicted, wings out

A) Use with MidiMACS™ or QuadroMACS™ Separator



### **DO NOT USE THE PLUNGER TO GET YOUR ISOLATED FLOW THROUGH**

- Prep column by rinsing with 3ml of buffer (1ml at a time to prevent it from taking the same path through the filter!) Once the column is prepped, use a different tube to collect the isolate.
- Apply cell suspension onto column- the flow through contains unlabeled cells which are the enriched cd8a- T-cells
- Apply 3ml off buffer and collect as isolated flow through. Apply 1 mL at a time. It is done when it has stopped dripping.
- IF YOU WANT YOUR UNLABELLED CELLS For confirmation purposes, you may remove the column, place it over a new tube, apply 5ml of buffer, then use the plunger to push the buffer through. These are your magnetically labelled cells.
- Pool the flowthrough of isolated cd8+ T cells, spin down at 1100 RPM and resuspend in 1 mL of T cell media
- Count cells on the automated cell counter
- Spin down, then resuspend in 1 mL activation media per 6e5 cells.

## **Culturing T cells**

### T cell activation

#### T cell media

T cell activation media: T cell media with 1 $\mu$ g/ml a-CD3 and 0.5 $\mu$ g/ml a-CD28 (no IL-2)

T cell expansion media: T cell media with 12 uL/mL of IL-2

Spin down and resuspend in CD8 T cell media. Count cells.

Adjust cells to be at a density of 6e5 cells/mL. Add a-CD3 and a-CD28 (1:1000 dilution for both)

Plate in activation media at a volume of 1 mL per well of a 48 well plate

Culture in activation media for 72 hours

### T cell expansion

After 3 days, recover cells by vigorously pipetting. Spin down, and resuspend in T cell media. Count cells, and adjust to a density of 6e5 cells/mL.

Add IL-2 at a dilution of 1:83 (12 uL per mL of media, aliquot is at 5e3 U/mL, so diluted amount is at 60 U/mL).

Plate at a density of 6e5 cells per mL

48 well – 1 mL/well

6 well – 3 mL/well

10 cm – 10 mL/well

### Notes

48 well – 1 mL/well (0.95 cm<sup>2</sup> per well)

6 well – 3 mL/well (9.5 cm<sup>2</sup> per well)

10 cm – 10 mL/well (~55 cm<sup>2</sup> per well)